Advanced Materials for the Delivery of Anti-Cancer Compounds and Imaging Contrast Agents

Wang, Wenbo

Publication date:
2019

Document Version
Publisher's PDF, also known as Version of record

Technical University of Denmark

Advanced Materials for the Delivery of Anti-Cancer Compounds and Imaging Contrast Agents

Ph.D. Thesis

Wenbo Wang

Supervisors

Jonas R. Henriksen (DTU Health Tech)
Thomas L. Andresen (DTU Health Tech)
Andreas T. I. Jensen (DTU Nutech)

Department of Health Technology
Technical University of Denmark
2800 Kgs. Lyngby
Denmark

February, 2019

Preface

The work presented in this PhD thesis is the result of 3 years of research carried out at DTU Chemistry from February 2016 to June 2017, DTU Nanotech from June 2017 to December 2018 and DTU Health Tech from January 2019 to February 2019. The work was conducted under the supervision of Associate Professor Jonas R. Henriksen as main supervisor, Professor Thomas L. Andresen and Senior Researcher Andreas. T. I. Jensen as co-supervisor.

Three separate projects are presented in this PhD thesis in Chapter 2 – 4. In Chapter 2 (*Development of multimodal fiducial markers for surgical guidance*), the *in vitro* self-quenching of the marker with dye was done in collaboration with Hongmei Sun, who was Visiting Scholar from China at DTU Nanotech. The *in vivo* evaluation was conducted by Anders E. Hansen and Frederikke P. Fliedner at Department of Clinical Physiology, Nuclear Medicine & PET, Cluster for Molecular Imaging, Rigshospitalet and University of Copenhagen.

In Chapter 3 (*Preclinical evaluation of cationic DOTA-triarginine-lipid conjugates for controlled intratumoral distribution of radionuclides in brachytherapy*), two cationic DOTA-triarginine-lipid conjugates was synthesized by Rasmus Eliasen at DTU Nanotech. The *in vitro* cell toxicity study was conducted by Researcher Fredrik Melander at DTU Nanotech. The *in vivo* evaluation was conducted by Senior Researcher Anders E. Hansen and Frederikke P. Fliedner at Department of Clinical Physiology, Nuclear Medicine & PET, Cluster for Molecular Imaging, Rigshospitalet and University of Copenhagen.

In Chapter 4 (*Development of Injectable in situ Solidifying Depots for Controlled Release of Organometallic Anticancer Compounds*), two Ti-complex anticancer agents were synthesized by Senior Researcher Fedor Zhuravlev at Center for Nuclear Technologies, DTU. The *in vitro* cell toxicity study was conducted by Fredrik Melander at DTU Nanotech. The *in vivo* evaluation was conducted by Senior Researcher Anders E. Hansen and Trine Bjørnbo Engel at Department of Clinical Physiology, Nuclear Medicine & PET, Cluster for Molecular Imaging, Rigshospitalet and University of Copenhagen.

All the data analysis and other work were conducted by Wenbo Wang.

List of Publications

Journal Publications

1. Wenbo Wang, Hongmei Sun, Frederikke Petrine Fliedner, Anders Elias Hansen, Thomas Lars Andresen, Andreas I. Jensen, Jonas R. Henriksen. *"Multimodal Fiducial Markers for Surgical Guidance,"* to be submitted to Advanced Healthcare Materials.
2. Wenbo Wang, Rasmus Eliasen, Frederikke Petrine Fliedner, Fredrik Melander, Anders Elias Hansen, Thomas Lars Andresen, Andreas I. Jensen, Jonas Henriksen. *"Preclinical evaluation of cationic DOTA-triarginine-lipid conjugates for controlled intratumoral distribution of radionuclides in brachytherapy,"* to be submitted to Journal of Controlled Release.

Conference contribution

1. Wenbo Wang, Hongmei Sun, Frederikke Petrine Fliedner, Anders Elias Hansen, Thomas Lars Andresen, Andreas I. Jensen, Jonas R. Henriksen. *"Multimodal Fiducial Markers for Surgical Guidance,"* presented at 3rd EACR conference - Making it Personal: Cancer Precision Medicine

Acknowledgements

First of all, I would sincerely like to thank my supervisor Associate Professor Jonas R. Henriksen, for accepting me as a Ph.D. student and guiding me to be a real researcher. During the last three years, you were always patient, helpful, supportive and encouraging. It was a cheerful experience to be a Ph.D. student with you. I learnt not only specialized knowledge, but also how to work efficiently and balance work and personal life well. Special thanks also goes to my co-supervisor, Senior Researcher Andreas T. I. Jensen at DTU Nutech, for guiding me to work with radionuclides and the discussions on experiments. Moreover, your guidance on manuscript writing was extremely valuable for me. I would also like to thank my co-supervisor, Professor Thomas L. Andresen, for providing me a great working environment in the Colloids & Biological Interface (CBIO) Group at Nanotech and the access to the facilities in the group.

In addition, I would like to thank all my collaborators, Rasmus Eliasen at DTU Nanotech and Fedor Zhuravlev at DTU Nutech for synthesizing and providing the compounds for my projects; Anders E. Hansen at DTU Nanotech, Frederikke P. Fliedner at University of Copenhagen and Trine Bjørnbo Engel at DTU Nanotech for performing *in vivo* studies; Fredrik Melander at DTU Nanotech for performing *in vitro* cell studies. I would also like to thank Gokce Engudar and Linda M. Bruum for the valuable discussions about my projects.

I am grateful to all my colleagues in the CBIO group at DTU Nanotech for their help, encouragement and positive working atmosphere. I would like to thank all the colleagues in the Hevesy Laboratory at DTU Nutech for the patient help and discussion with my projects. Moreover, I want to thank all the great people in the Group of Polymers and Functional Interfaces Group led by Professor Esben Thormann at DTU Chemistry, for your joyful accompany during the first year of my Ph.D.

At last, I would like to thank Junhao Huang, Tao Jiang, Xiaoyan Liu and Xiaotong Feng, for being my great friends. I would also like to thank my family, especially my husband Jifeng, for your understanding, support and encouragement. Without you, this thesis would not be possible.

Abstract and Thesis Outline

Cancer is a public health problem and a major cause of death. The need for cancer treatment with high efficacy and safety is increasing. The work described in this thesis aims to design novel delivery systems to improve the current treatment modalities, including surgery, radiation therapy and chemotherapy. The thesis is divided into five separated chapters. Chapter 1 is an introduction describing the general information of novel drug delivery systems for intratumoral injection, imaging modalities and current cancer treatment methods. Chapter 2, 3 and 4 present three separate research projects, forming the backbone of this Ph.D. work. Chapter 5 is a general conclusion section of all the work described in the thesis. A full list of references is attached in the end.

In Chapter 1, novel drug delivery systems for intratumoral injection, such as liposomes, micelles and *in-situ* forming drug depot, were introduced. These systems have been considered as promising vehicles to deliver drugs to the tumor with a low system exposure. Imaging modalities are crucial in all the phases of cancer management, especially in cancer drug development. Therefore, some imaging modalities that are used in the thesis as well as their current clinical applications have been described. In the end, the commonly used clinical treatment methods including chemotherapy, radiation therapy and surgery are introduced especially focusing on the present clinical limitations and the-state-of-art in the research.

Chapter 2 described an injectable multimodal fiducial marker based on sucrose acetate isobutyrate (SAIB), which is generally-recognized-as-safe by the FDA. The marker contained an iodinated SAIB, xSAIB, as computed tomography (CT) contrast, 2,11,20,29-tetra-tert-butyl-2,3-naphthalocyanine (PC) as near-infrared (NIR) imaging fluorophore as well as complexation with $^{64}Cu^{2+}$ for positron emission tomography (PET) imaging and gamma detection. The novel marker has the potential to reduce the discomfort to the patients due to the use of injectable and safe material. Moreover, the novel marker combined the advantages of different technologies by providing preoperative information by CT and PET images, and the accurate intraoperative location of tumor by gamma detection and real-time NIR images. The optimal concentration of NIR dye in the marker that gave the highest fluorescent intensity was identified. The effect of ethanol efflux and copper on the fluorescence of the marker was investigated. Finally, the marker was subcutaneously injected into mice for *in vivo* evaluation by CT, PET and NIR imaging.

In Chapter 3, two novel non-toxic DOTA-triarginine-lipid conjugates, D3R-C16 and D3R-C18, to deliver radionuclides for brachytherapy were synthesized. Both compounds are based on the chelator

1,4,7,10-Tetraazacyclododecane-1,4,7,10-tetraacetic acid (DOTA), which is known for high stability chelation of a range of medically relevant radionuclides, such as ^{64}Cu, ^{177}Lu, ^{225}Ac, ^{68}Ga, etc. Moreover, the compounds were functionalized with hydrophobic acyl chains (16C or 18C) and strongly cationic triarginine groups (arginine sidechain pka: 12.5). The scientific objective was that two compounds are expected to partition into liposomal and cell membranes as surfactant. Moreover, the positive charge of triarginine groups are supposed to enhance the charge-based interaction with Din placeringcancer cell membranes, which are generally slightly negative charged. The critical micelle concentration (CMC) and the partitioning properties into liposomes with varying surface charge of the surfactants were investigated *in vitro*. The lead compound D3R-C18 was radiolabeled with copper-64 (^{64}Cu) and evaluated *in vivo* by intratumoral injection as both a free compound and a formulation in liposomes. The *in vivo* biodistribution of the formulations was achieved by PET/CT imaging.

Chapter 4 described a new generation of Ti-complex chemotherapeutic drug, SaTiDv2, which was synthesized by our collaborator Senior Researcher Fedor Zhuravlev from the Center for Nuclear Technologies at the Technical University of Denmark. The *in vitro* cytotoxicity study showed that SaTiDv2 was more toxic than the previous SaTiD towards CT26 cells. In order to achieve a high tumor concentration and low systemic exposure of the drug, the SaTiDv2 was formulated into *in situ* forming depot formulation based on sucrose acetate isobutyrate (SAIB) or lactose octaisobutyrate (LOIB) with glycerol trioctanoate (GTO) and different organic solvent (DMSO, propylene carbonate or benzyl alcohol). The purpose of adding hydrophobic GTO into the formulation is to reduce the viscosity of the depot and slowly exchange with water from the surrounding environment after the efflux of the organic solvent. Therefore, the drug could slowly release from the formulation over a prolonged period. The optimal formulation that gave the highest cumulative release was investigated *in vivo* by intratumorally injecting the formulation into tumor-bearing mice.

Danske Resume

Kræft er et folkesundhedsproblem og en væsentlig dødsårsag. Behovet for kræftbehandling med høj effektivitet og sikkerhed er stigende. Arbejdet beskrevet i denne afhandling har til formål at designe nye formuleringer til forbedring af de nuværende behandlingsmetoder, herunder kirurgi, strålebehandling og kemoterapi. Afhandlingen er opdelt i fem adskilte kapitler. Kapitel 1 er en introduktion, der beskriver den generelle information om nye lægemiddelafgivelsessystemer til intratumoral injektion, billeddannelsesmodaliteter og nuværende cancerbehandlingsmetoder. Kapitel 2, 3 og 4 præsenterer tre separate forskningsprojekter, der udgør kernen i dette Ph.D. arbejde. Kapitel 5 er et generelt konklusionsafsnit af alt det arbejde, der beskrives i afhandlingen. En komplet liste over referencer er vedlagt i slutningen.

I kapitel 1 introducere nye lægemiddelafgivelsessystemer til intratumoral injektion, såsom liposomer, miceller og in situ-dannende lægemiddeldepot. Disse systemer betragtes som lovende drug delivery systemer til at levere lægemidler til tumoren med lav systemeksponering. Billeddannelses modaliteter er afgørende i alle faser af kræftbehandling, især i udvikling af kræftmedicin. Derfor er nogle af de medicinsk billeddannelses former, der anvendes i afhandlingen, såvel som deres nuværende kliniske anvendelser blevet beskrevet. I sidste del introduceres de almindeligt anvendte kliniske behandlingsmetoder, herunder kemoterapi, strålebehandling og kirurgi, specielt med fokus på de nuværende kliniske begrænsninger og state-of-the-art inden for diagnostik.

I kapitel 2 beskrives en injicerbar multimodal fiducial markør baseret på sucrose-acetate-isobutyrate (SAIB), som generelt er anerkendt som sikker af FDA. Markøren indeholder en ioderet SAIB, xSAIB, som CT-kontrast, 2,11,20,29-tetra-tert-butyl-2,3-naphthalocyanin (PC) som nær-infrarød (NIR) billeddannende fluorofor og som kompleksdannelse med $^{64}Cu^{2+}$ til positron emission tomografi (PET) billedbehandling og gamma detektion. Denne markør type har potentiale til at reducere ubehag for patienterne på grund af materiales nemme injicerbarhed. Desuden kombinerer den nye markør fordelene ved forskellige teknologier ved at tilvejebringe præoperativ information ved hjælp af CT- og PET-billeder og den nøjagtige intraoperative placering af tumor ved gamma-detektion og realtids NIR-billeder. Den optimale koncentration af NIR-farvestof i markøren, som gav den højeste fluorescerende intensitet, blev identificeret. Effekten af ethanol udsiving fra markøren samt kobber på fluorescensen af markøren blev undersøgt. Endelig blev markøren injiceret subkutant i mus til in vivo-evaluering ved CT-, PET- og NIR-billeddannelse.

I kapitel 3 beskrives to nye ikke-toksiske DOTA-triarginin-lipidkonjugater, D3R-C16 og D3R-C18, til levering af radionuklider i brachyterapi. Begge forbindelser er baseret på chelatoren 1,4,7,10-tetraazacyclododecan-1,4,7,10-tetraeddikesyre (DOTA), som er kendt for høj stabilitetskelering af en række medicinske relevante radionuklider, såsom ^{64}Cu, ^{177}Lu, ^{225}Ac, ^{68}Ga osv. Desuden blev forbindelserne funktionaliseret med hydrofobe acylkæder (16C eller 18C) og stærkt kationiske triargininggrupper (arginin sidekæde pka: 12,5). Det videnskabelige mål var, at de to forbindelser forventes at fordele sig i liposomale og cellemembraner som overfladeaktive stoffer. Desuden vil den positive ladning af triargininggrupper forøge den ladningsbaserede interaktion med cancercelle membraner, som generelt er lidt negative ladede. Den kritiske micellekoncentration (CMC) og fordelingsegenskaberne i liposomer med varierende overfladeladning af de overfladeaktive stoffer undersøgtes in vitro. Det ene konjugat, D3R-C18, blev radioaktivt mærket med kobber-64 (^{64}Cu) og blev efterfølgende evalueret *in vivo* ved intratumoral injektion både som fri forbindelse og som liposomal formulering. In vivo biodistribution af formuleringerne blev evalueret via PET/CT-billeddannelse.

Kapitel 4 beskriver en ny generation af det kemoterapeutisk lægemiddel, SaTiDv2, som blev syntetiseret af vores samarbejdspartner Seniorforsker Fedor Zhuravlev fra Center for Nuclear Technologies ved Danmarks Tekniske Universitet. En *in vitro* cytotoksicitetsundersøgelsen viste, at SaTiDv2 var mere toksisk end det tidligere SaTiDv1 mod CT26-celler. For at opnå en høj tumorkoncentration og lav systemisk eksponering af lægemidlet blev SaTiDv2 formuleret til *in situ* dannelse af depotformulering baseret på sucrose-acetate-isobutyrate (SAIB) eller lactose octa-butobutyrat (LOIB) med glyceroltrioctanoat (GTO) og forskellige organiske solventer (DMSO, propylencarbonat eller benzylalkohol). Formålet med at tilføje det hydrofobe GTO til formuleringen er at reducere depotets viskositet som langsomt udbytte med vand fra det omgivende miljø efter udsigning af det organiske opløsningsmiddel. Derfor frigives lægemidlet langsomt fra formuleringen over en længere periode. Den optimale formulering, der gav den højeste kumulative frigivelse blev undersøgt *in vivo* ved intratumoralt injektion af formuleringen i tumorbærende mus.

Table of Contents

Chapter 1. Introduction

1.1 Background

Cancer is one of the leading causes of death worldwide. It is estimated by the World Health Organization (WHO) that 14 million people died from cancer in 2012 with an expected increase of 50% in 2030 [1]. Before treatment, the patients are usually classified by a TNM (referring to tumor, node and metastasis) staging system, which describes the extent of the cancer. The TNM system can be broadly divided into early stage (small tumor without spreading), intermediate stage (lager tumor or evidence of lymph node involvement), and late stage (metastasis to other organs) [2, 3].

The type of treatment for cancer is dictated by the stage, cancer type, and the tolerance of patients to the therapy [3]. At present, the commonly used clinical treatment modalities include chemotherapy, radiation therapy and surgery. Chemotherapy uses chemicals to kill cancer cells and it is curative in many types of advanced cancers, such as lymphoblastic, myelogenous leukemia, germ cell cancer, small cell lung cancer and ovarian cancer [4]. In radiotherapy, cancer cells are killed by ionized radiations, which are applied either internally or externally. Radiotherapy is usually applied for solid tumors, especially prostate cancer. Surgery is the process to remove tumors, once detected. Surgery is considered as the primary treatment for solid tumors. Chemotherapy or radiotherapy may be used before or after the surgery.

Due to the improvements in early detection and the progress in the above-mentioned therapies, the incidence of cancer mortality has decreased over the last several decades [3]. However, the major shortcomings in treatment-associated morbidity and recurrence rate after therapy still exist. The challenges in the current cancer therapies are low therapeutic index of chemotherapy because of systemic administration, and the unpleasant procedures of radiotherapy and surgery to the patients, (i.e. the pain caused by the hard implant during the procedure). The discovery of the new drug delivery systems for locoregional administration, such as nanoparticles and biocompatible materials, have been consider as promising approach to improve the existing treatments. In addition, with the development of advanced molecular imaging technologies including positron emission tomography (PET), single-photon emission computed tomography (SPECT) and near-infrared (NIR) fluorescence imaging, the *in vivo* performance of these systems can be well described in a non-invasive manner.

In the following sections of this chapter, novel drug delivery systems for intratumoral injection and some imaging modalities used in cancer management will be introduced. Furthermore, the commonly used clinical treatments to cancer, including their current challenges and relevant researches, will be summarized.

1.2 Novel drug delivery system for intratumoral administration

Currently, most of the chemotherapeutic drugs are delivered by systemic administration (Figure 1 left). However, when the drugs are delivered intravenously, the high concentration in the plasma can result in insufficient dose reaching the tumor with severe unwanted side effect [5, 6]. Additionally, the insufficient dose could also be a result of rapid plasma clearance of the drugs, which is very common to many anticancer compounds [5]. Therefore, an effective treatment can never be achieved. Even though some novel drug delivery systems such as gold particles and liposomes, have the ability to passively accumulate in tumor by the enhanced permeability and retention (EPR) effect, the uptake of these particles in healthy tissues especially liver and spleen is still significant by the systemic administration [7, 8, 9]. Intratumoral injection (Figure 1.1 right) is an alternative effective administration method, which has the potential to deliver anticancer drugs locally to the tumor with minimum exposure to heathy tissues [6]. Moreover, some delivery systems are able to control and prolong the drug release, and consequently reduce multiple drug administration cycles. It has been demonstrated that the extended exposure of tumor cells to chemotherapy over multiple cell cycles has been shown to be more cytotoxic than multiple drug administration cycles [3].

In internal radiation therapy, the radiation sources are put inside patient's body by either systemic administration or the local implantation of radioactive seeds. Even though some clinical systemic administrations target to the specific receptors on tumors, such as ^{111}In-DTPA-Octreotide and ^{177}Lu-DOTATATE [10], the residence time of radiation in other tissues cannot be ignored [11]. Therefore, acute side effects (i.e. nausea, pain, or vomiting) usually occurs within 24 hours after administration [12]. Brachytherapy is a localized form of radiation therapy, where radiation sources are implanted into the tumor to provide high local dose and less harm to healthy tissues [13]. At present, the materials used to deliver radiation in brachytherapy like metal, needles and plastic catheters are generally invasive and cause a lot of discomfort to the patients. Image-guided surgery has the similar problem, as the markers for intraoperative localization of the tumor are hard and non-biocompatible materials as well.

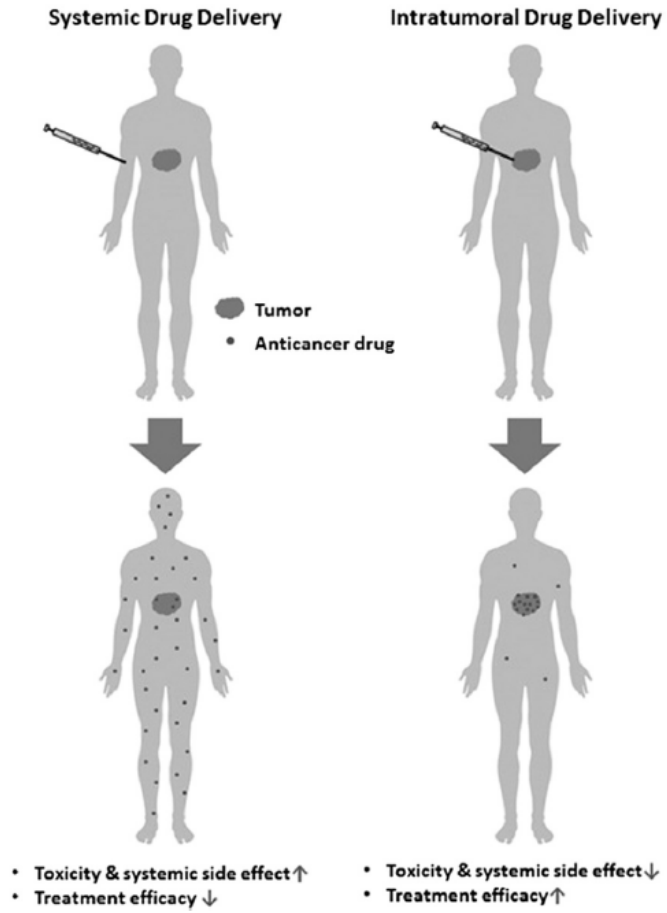

Figure 1.1. Systemic and intratumoral drug delivery. Systemic drug delivery is the most common administration, however, the limitations are insufficient local-dose and high side effect in healthy tissues. Intratumoral injection is an alternative approach, which can increase local drug dose and decrease the systemic toxicities (figure adapted from reference [6]).

Therefore, biocompatible and biodegradable drug delivery systems for intratumoral injection are highly needed for all of these common treatments. Some promising materials, such as nanoparticles, hydrogels and polymers, have been well studied by many researchers. In the following sections, liposomes, micelles and carbohydrate ester based system will be described in details.

1.2.1 Liposomes

Liposomes, known as spherical-shape artificial vesicles dispersed in the aqueous medium, were firstly described in the mid-60s. Figure 1.2A presents the structure of a liposome. Liposomes can be formed

by the spontaneous aggregation of phospholipids, which are the major components of biological membranes. Phospholipid is amphiphilic, containing a hydrophilic charged head and two hydrophobic chains (Figure 1.2B). The chemical structure and properties of phospholipids determine the characteristics of the liposomes in which they are located. For instance, the unsaturated phospholipids form a more permeable and less stable bilayer structure. On contrary, the saturated phospholipids form impermeable bilayers [14, 15]. The hydrophilic head of phospholipid has different charges, which determine the surface charge of liposomes and further affect the treatment efficacy. The commonly used neutrally charged lipids are phosphatidylcholine (PC) and phosphatidylethanolamine (PE). Phosphatidylglycerol (PG) and phosphatidylinositol (PI) are negatively charged lipids [16]. Positively charged phospholipid have been successfully synthesized for the delivery of nucleic acid [16, 17]. In Chapter 3, we have prepared liposomes containing PG, PC or the mixture of DSPE-PEG (2000), HSPC and cholesterol. All the structures of these lipids are presented in Figure 1.2B.

Another major structural element of liposomes is cholesterol, a lipid consisting of a steroid ring structure as its hydrophobic part, and a simple hydroxyl group as its polar head (Figure 1.2B). Cholesterol is a stabilizer and it has the ability to increase the packing of phospholipid molecules, therefore, to reduce the permeability of the bilayer to other compounds [18, 19].

Polyethylene glycol (PEG) lipid is usually included to prepare the liposomes for systemic administration in order to increase the circulation time of liposomes in body. Liposomes are cleared quickly from bloodstream by the reticuloendothelial system (RES) organs, such as liver and spleen. PEG creates a hydrated protective layer around the liposomes to prevent the binding of liposomes with the proteins in serum, and further prevent the recognition by RES system [20]. For intratumoral administration, PEG coating might increase the retention time of liposomes in lymph node [21]. This characteristic can be used to treat both primary tumor and lymph node metastases. In addition, PEG coated liposomes are promising to deliver imaging contrast to lymph node for imaging guided lymph node mapping.

Liposomes can be prepared by different methods. The most common method is dissolving lipids in organic solvents in order to well mix the lipids and ensure the formed liposomes are homogeneous. The organic solvents are then removed by freeze-drying or rotary evaporation (film-method). The resulted dry lipids are hydrated by using aqueous media, and the liposomes are created by vortexing or stirring the solution above the membrane phase transition temperature [15]. The liposomes

produced by this method are usually multilamellar vesicles (MLVs) consisting more than one bilayers with the size over 1000 nm [22]. In order to convert multilamellar vesicles to unilamellar vesicels, which consist only one bilayer, the liposomes can be extruded through the polycarbonate filters with pore sized in the desired range. This method is known as extrusion or French press [23]. Other methods exist for preparing liposomes, such as freeze-thawed liposomes, reverse-phase evaporation, more information can be found in [15, 22].

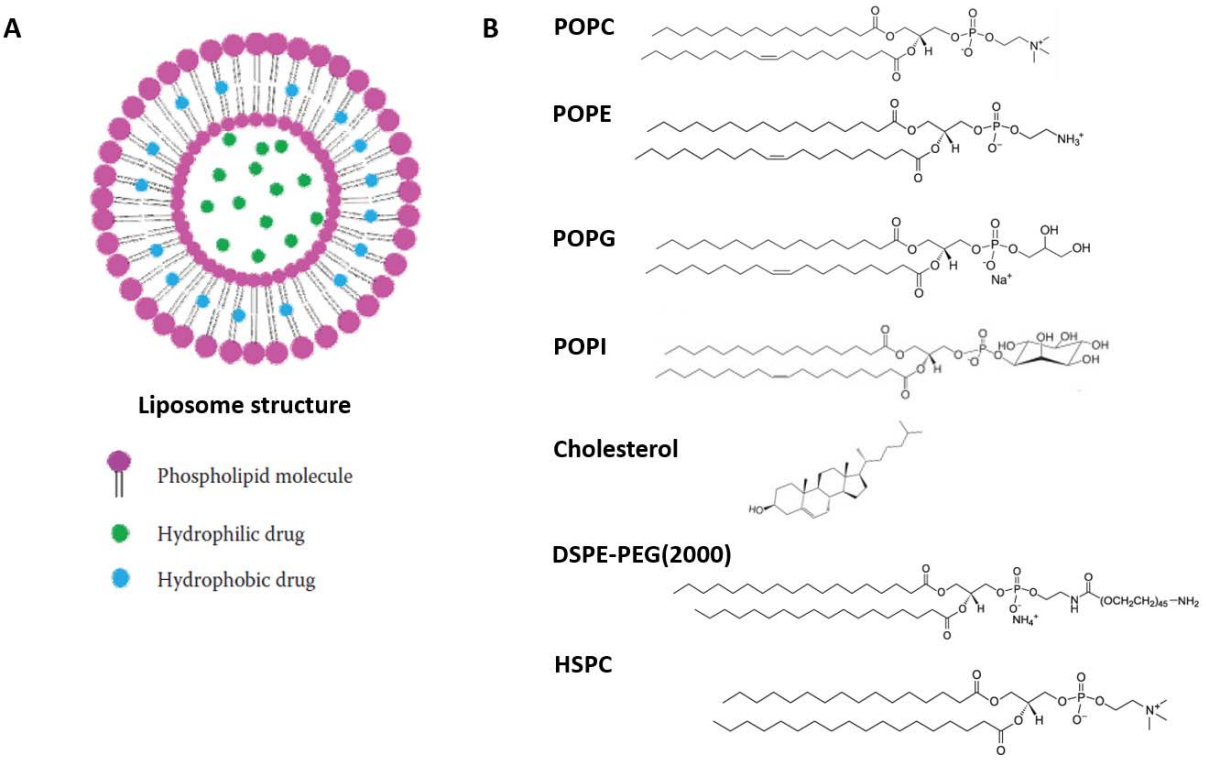

Figure 1.2. Liposome structure as a drug delivery carrier (A) (Figure adapt from [22]), structure of some commonly used phospholipid and cholesterol (B).

The unique structure of liposomes enable the ability to entrap both hydrophilic (in the core) and hydrophobic (in the lipid membrane) compounds (Figure 1.2A). Liposomes are extensively used as the carriers for cancer treatment. For example, Doxil® is the first liposomal drug approved by FDA in 1995 [24]. Most of the studies on liposomes focus on systemic administration due to the prolonged drug circulation time in blood stream. Recently, using liposomes in locoregional delivery has been proposed as a strategy to avoid RES and tumor vasculature barriers [25]. Due to the larger size of liposomes than small molecules, liposomes exhibit a longer tumor retention because of a much slower clearance from the interstitial space. Moreover, liposomes have lower interaction with tumor

extracellular matrix. Thus, they are able to infuse throughout the tumor interstitial space, resulting in a better intratumoral distribution than some small molecules [25, 26]. Addition to the excellent biocompatibility and biodegradability, liposomes are promising drug delivery system for intratumoral administration.

1.2.2 Micelles

Micelles (Figure 1.3) are formed by amphiphilic molecules (also termed as surfactant), which have the tendency to accumulate at the boundary of such as water-oil like interphases. In an aqueous solution, amphiphilic molecules orientate themselves at the surface of the solution and remove the hydrophobic moieties from the aqueous environment in order to achieve a state with minimum free energy. When the concentration of amphiphile increases, the unfavorable interaction between water molecules and the hydrophobic region of the amphiphile causes a decrease in entropy, increasing the free energy of the system. In a specific and narrow concentration range of amphiphile in solution, termed the critical micelle concentration (CMC), amphiphilic molecules are saturated at the surface of the solution and start to self-assemble into colloidal-sized particles, which are termed as micelles. The free energy of the system decreases by minimizing the unfavorable interactions between the surrounding water molecules and the hydrophobic part of the amphiphile. Upon diluting the micelles solution below CMC, micelles disassemble. The rate of disassembly depends on the structure of micelles and the interaction with the hydrophilic chains [27].

Polymeric micelles (PM) are attractive for intravenous drug delivery, since they can be designed with narrow size distributions in the range of 5 - 100 nm [28], which is crucial for the tumors with very small fenestration [29]. PM is assembled by amphiphilic long copolymers in aqueous solutions. Like phospholipid, one end of the copolymer is hydrophobic and the other end is hydrophilic, which is usually PEG. Hydrophobic drugs are usually loaded in the hydrophobic core by non-polar associations. PMs usually exhibit a CMC much lower than the micelles formed from conventional surfactants such as sodium lauryl sulphate. In general, a higher molecular weight and a more hydrophobic property leads to a lower CMC [28, 30]. Moreover, PMs are insensitive to dilution and resist disassembly upon dilution due to the physical interactions between the chains in the micelle core. Therefore, PMs have an enhanced circulation time in plasma compared to the micelles formed from conventional surfactants [28, 31]. So far, five micellar formulations for intravenous administration to treat various cancer types have been tested in clinical trials [28].

The use of micelles alone as carriers to deliver anticancer agents for intratumoral injection has been seldom discussed. Some intratumoral administrated drug delivery systems combining micelles and thermosensitive hydrogel have been reported. The idea is that the body heat triggers the phase transition of the hydrogel into an insoluble, viscous and stable depot for long-term brachytherapy [32] or chemotherapy [33]. The purpose of combining micelles is to increase the drug loading capacity [33].

In this thesis, a cationic micelles drug delivery system for brachytherapy based on the properties of the surfactant is designed. Once the micelles are injected into tumor, a state of sink condition occur immediately, meaning that micelles dissemble into individual unimers. With the presence of membranes, the surfactants might partition into the membrane at a low concentration, meaning that the radiation loaded on the surfactants can be attached onto the surface of the tumor cells with a long retention time. The behavior of the surfactant *in vivo* is determined by the CMC and its ability to partition into the membrane (Figure 1.3B). More details of this system will be described in Chapter 3.

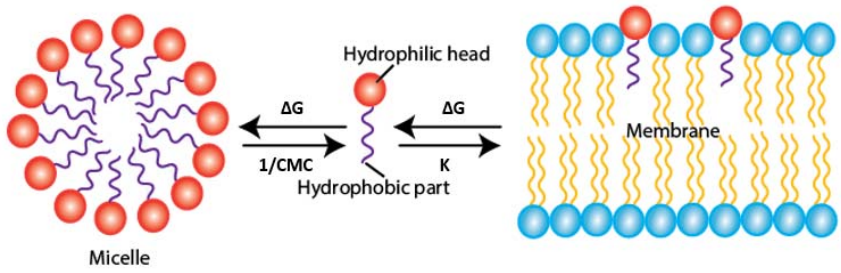

Figure 1.3. The structure of micelle and illustration of the surfactant equilibria in the presence of a lipid membrane. The partitioning of surfactant into membrane is determined by the partition coefficient, K, and the free energy of partitioning ΔG. The formation of micelle is determined by CMC and the free energy of transferring a surfactant unimer from bulk to micelle.

1.2.3 *In-situ* forming systems

In recent decades, injectable *in-situ* forming systems such as polymer-based systems have gained considerable attentions. Various natural polymers, including alginate [34], dextran [35], chitosan [36] and polypeptides [37] have been investigated for drug delivery systems [3]. These materials are biodegradable and are tolerable *in vivo*. Synthetic polymers have emerged in order to achieve the specific design of properties, such as drug release kinetics and degradation rate [38]. All of these polymers can be injected in liquid solutions, and form a hydrogel drug depot spontaneously via self-

assembly or by crosslinking upon injection. The intratumoral injection of these soft materials is advantageous to being less invasive and less pain to patients [6]. However, many polymers are hydrophilic and they are not compatible with water-insoluble anticancer agents or contrast agents. Moreover, the use of synthetic polymers might cause inflammation and immune responses at the implant site due to the accumulation of acidic degradation products [3].

Another interesting injectable *in-situ* forming drug depot is carbohydrate ester system. Sucrose acetate isobytyrate (SAIB, structure is presented in Figure 1.4A) is a non-polymeric, highly hydrophobic and fully esterified derivate of sucrose. Due to its biodegradable and biocompatible properties, SAIB has been approved for oral consumption and is generally regarded as safe (GRAS) by FDA [39, 40]. SAIB exists as a very viscous liquid (100 Pa·s) [41]. When diluting SAIB with organic solvents, such as ethanol, N-methyl-2-pyrrolidone (NMP), dimethyl sulfoxide (DMSO), benzyl alcohol, and others, the viscosity of the mixture is dramatically reduced to 0.05 – 0.2 Pa·s [41, 42, 43], which is injectable through thin needles. Upon injection, the solvent diffuses from the depot into body fluid, resulting in a highly viscous SAIB depot, from where the drug can be released slowly for long period of time [39, 41, 43]. The SAIB depot system is very flexible, and the designated release of drug can be achieved by adding different additives in the system. The diffusion rate varies of different solvents from SAIB depot, the higher diffusion rate of the solvent usually results in a higher burst release [39]. Moreover, the higher solubility of the drug in organic solvent can also give a higher burst release [39]. Biodegradable polymers such as Poly(lactic acid) (PLA) and poly(lactic-co-glycolic acid) (PLGA) have been involved in SAIB depot system. A solid thick shell is formed by these polymers to decrease the diffusion of solvent, therefore, the burst release of drug is reduced [39, 43]. Hydrophobic solutions such as glycerol trioctanoate (GTO) and glycerol trihexanoate (GTH) diffuse from SAIB system very slow due to their hydrophobic property, therefore, they are retained in the depot to prevent the solidification and lower the viscosity of the depot. As a result, the drug will continuously release from the depot. Other carbohydrate esters, such as the ester of lactose, trehalose, maltose (Figure 1.4B) have been synthesized and tested in our group recently. The idea is various formulations can be generated or optimized for different purposes in cancer treatments.

SAIB depot system has been widely applied to deliver drugs, such as small molecules [39], pepetides [43] and protein [44]. SAIB depot system is more attractive in cancer treatment due to its large loading capacity for hydrophobic molecules. A novel injectable marker for image-guided radiotherapy based on SAIB depot system, BioXmark, has been recently developed by a Danish company, Nanovi. Upon injection, the marker formed a highly viscous gel-like material consisting CT-contrast (see section

1.4.2) with high stability over a period of months [45]. Clausen et al. have combined BioXmark with a ^{125}I-radiolabeled SAIB derivative for radiation surgical guidance [46] (imaging guided surgery: see section 1.4.3). The multifunctional fiducial marker was stable in the site of injection for over 7 days. The radioactivity was well retained in the marker as well. Therefore, the marker can be implanted up to 7 days prior to surgery, which give surgeons enough time to plan the procedure. In brachytherapy (see section 1.4.2), the SAIB depot system is a promising alternative to current material in clinical use, such as metal seeds. The injectable formulations consisting radionuclides based on SAIB or LOIB (lactose octaisobutyrate) were developed in our group. Various formulations were designed based on the properties of the radionuclides.

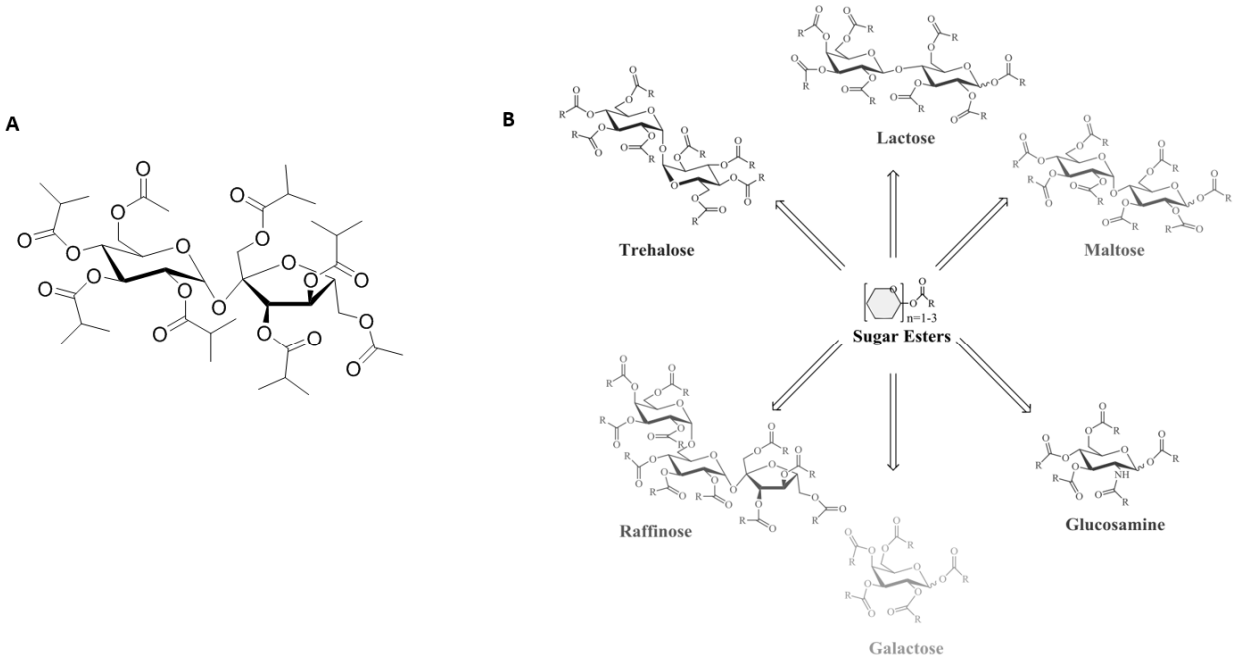

Figure 1.4. Structure of SAIB (A) and other possible carbohydrate esters (B).

1.3 Imaging techniques and their use in cancer management

Imaging is non-invasive and real-time visualization of biochemical events [47], which include morphological, structural, metabolic and functional information. Biomedical imaging techniques are crucial in all the phases of cancer management including diagnosis, staging, theranostic and treatment [48]. Imaging modalities can be classified to two areas [49]. One is *anatomical imaging*, such as CT and MRI, which can provide the structure of body including tumor with certain mass. The other one

is *molecular imaging* including nuclear imaging (PET and SPECT) and NIR fluorescent imaging where measuring ADME by detecting tracers.

Multimodal imaging, co-registration of several image modalities such as the combination of SPECT or PET with CT, has the advantage to compensate the limitations of each modality and is widely used in the current clinical applications. In the following sections, some modalities (Figure 1.5) that are relevant to the current thesis are introduced.

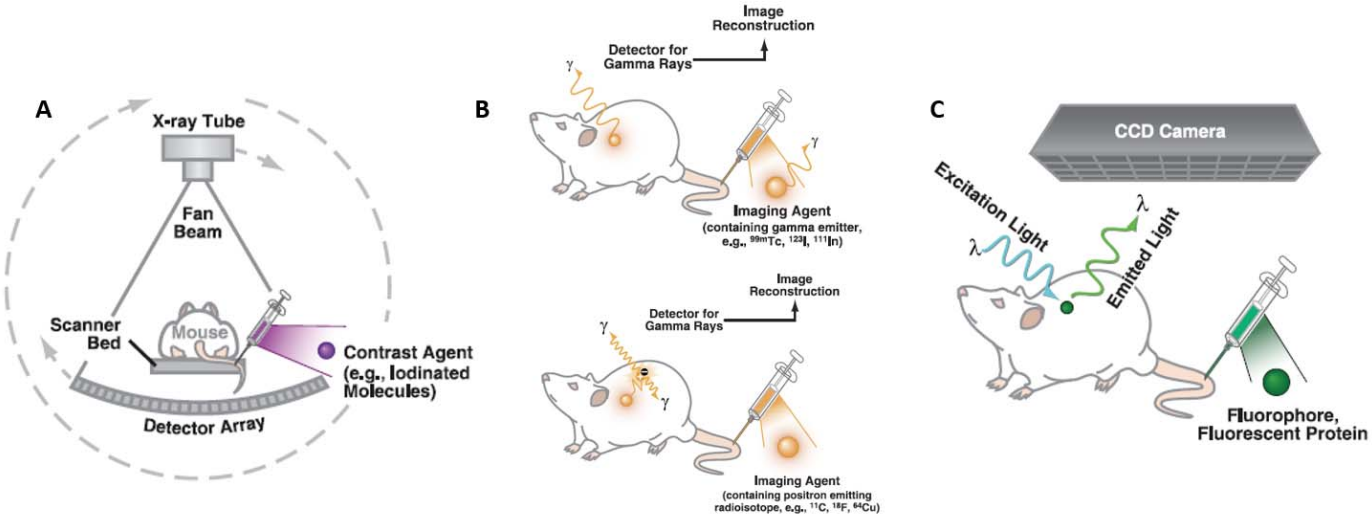

Figure 1.5. Schematic presentation of small animal imaging modalities: CT scan (A), nuclear imaging SPECT (up) and PET (down) (B), and fluorescent imaging (C). Figures were adapted from [47].

1.3.1 CT

The principle of CT is based on the differential levels of X-ray attenuation by the tissues in body so that images reflecting anatomy are produced. Figure 1.5A shows the basic geometry of a CT scanner. X-rays are generated from the X-ray tube by accelerating electrons using high voltage and it passes through the living subject on the scanner bed. Tissues will attenuate part of the X-rays and the rest of X-rays will be detected. In order to obtain 3D CT images, X-ray tube and detector array rotate simultaneously during scan to get a series of attenuation profiles of the target from different angels. Tissues that only slightly attenuate X-rays such as the lung appear black, in contrast, whereas tissues that attenuate X-ray to higher extend such as bone appear white. Therefore, high-contrast images exhibiting details of morphology and structure are created [47, 50, 51]. Hounsfield unit (HU) is the

attenuation values to describe the ability of matter to attenuate X-rays. Water is assigned as 0 HU and air is -1000 HU. The attenuation values for most soft tissues are in the range of 30 – 100 HU and mineralized tissues such as bone has attenuation values of approximately 1000 HU. CT has the advantages of high special resolution (pre-clinical = 0.05 – 0.2 mm, clinical = 0.5 – 1.0 mm), fast scan, cost effectiveness and relative sample operation. However, the limitations are its poor sensitivity, ionizing radiation to patients and the limited soft tissue resolution [47, 52].

Even though tissues exhibit contrast due to their different attenuation values, the imaging and identification of soft tissue or adjacent tissues such as liver and tumor is still challenging. Therefore, a CT contrast agent, which contains elements with higher atomic number (Z) like I, Ba, Au, Bi, etc., is often used to improve the spatial resolution and soft tissue contrast during CT scan. CT contrast agents based on Iodine ($Z = 53$) are mostly used in the current clinics. Some small molecules iodinated contrast agents such as iohexol, iopromide, iodixanol etc. for intravenous injection have been approved for clinical use [53]. Most of them are based on a 1,3,5-triiodobenzene ring and further optimized by functional groups such as carboxylic acids or imines. Even though these approved contrast agents significantly improve the quality of CT images, they do suffer from some shortcomings such as the non-specific biodistribution, rapid renal clearance and the renal toxicity caused by high osmolality of these compounds [51]. Iodinated contrast agents in nanometer range, such as liposomes, nanosuspensions and micelles, were developed to address these limitations. In general, in comparison with small molecules, nanoparticles are supposed as the possible solution to increase blood circulation time, and reduce the rate of renal clearance. A CT marker based on SAIB (BioXmark) for intratumoral injection was also developed for image-guided radiotherapy (see section 1.4.2).

CT is used in cancer in many different ways, including diagnose abnormal growths, provide information about the stage of cancer, guide and plan therapies. One typical example is CT lung cancer screening, which can distinguish benign and malignant nodules based on the size, shape and doubling times of lung nodules [54]. It is a valuable guidance for the later radiotherapy or surgery. However, due to the low sensitivity of CT imaging, hybrid imaging system combining CT and other sensitive molecular imaging techniques, such as PET and SPECT, are commonly used in the clinic.

1.3.2 SPECT and PET

SPECT and PET are quantitative nuclear emission tomography that enable the evaluation of biochemical changes by the imaging of specific molecular radioactive tracer. It is more effective to detect biochemical changes than the anatomic changes, which usually show after biochemical changes. Therefore, SPECT and PET have the advantages to diagnose early stages of disease compared to CT [55]. Other strengths of using nuclear emission tomography are deep tissue penetration depth and high sensitivity. While, the common limitation is the lack of anatomical structure. Therefore, hybrid SPECT/CT and PET/CT systems have been introduced with the advantages of providing images with both functional and anatomical structure [47, 56, 57]. Other disadvantages, such as low spatial resolution and ionizing radiation to patients, should also be taken into consideration when applying these techniques.

When a nucleus of the radionuclide exists in an exited state, the excess energy can be emitted in the form of gamma photons. SPECT can detect the radionuclides emitting gamma photons (SPECT radionuclides), such as ^{99m}Tc ($T_{1/2}$ = 6 h), ^{123}I ($T_{1/2}$ = 13.3 h), and ^{111}In ($T_{1/2}$ = 2.8 days). Figure 1.5B presents the process of SPECT imaging. A SPECT imaging agent is administered into the living subject, and the gamma rays from the agent are detected by a gamma camera detector. Images of tomographic reconstruction are obtained by rotating the gamma camera around the subject to collect data from numerous positions. The gamma camera is equipped with collimators to define the angle of the gamma rays, therefore, diagonally incident photons can be excluded. Comparing to PET, different radionuclides can be distinguished in the same SPECT scan because gamma photons have different energies. While PET only detects annihilation radiation, which is always 511 keV. Thus, SPECT is very important to study the new drug delivery systems like double-labeled nanoparticles [58]. However, the use of collimators in the camera results in a lower sensitivity of SPECT in comparison with PET, since a lot of radiation is filtered off by the collimators. Though PET/CT is currently more commonly used than SPECT/CT, the earliest attempts to achieve both anatomical and functional information were started with SPECT [49, 59]. In the current clinical application, SPECT/CT is still widely used for lymphoscintigraphy, which is the standard method for cancer staging [60, 61].

PET can detect the radionuclides emitting positrons (PET radionuclides), such as ^{18}F ($T_{1/2}$ = 110 min) and ^{64}Cu (12.7 h). The nuclei of PET radionuclides are unstable with excess protons, and this instability causes transforming a proton into a neutron, a positron and a neutrino. The positrons will

annihilate by combining electrons in the tissue. As a result of annihilation, the positrons and electrons convert into two anti-parallel photons, each with the energy of 511 keV (Figure 1.5B) [62]. A PET detector contains a ring of scintillation detectors. During PET scan, the subject is placed in the ring and the detectors from various planes simultaneously record the coincidence signals, which are the anti-parallel photons at the same time in order to achieve a dimensional image. The resolution of PET images can be improved by only detecting coincidence signals instead of using collimators in the SPECT detectors. As a result, PET is at least 10 fold more sensitive than SPECT, in the range of 10^{-11} – 10^{-12} moles/liter [47, 56]. This advantage allows a shorter scan time with improved quality of the images. Moreover, due to the high energy of annihilation photon, the penetration depth of PET is deeper than SPECT in most cases. At present, PET [^{18}F]-2-fluoro-2-deoxy-glucose ([^{18}F]FDG) scan is widely used to diagnose, stage, and monitor cancer, as well as predict treatment response by imaging glucose metabolism in body [63, 64]. Due to the enhanced glucose uptake by cancerous cells, FDG is a specific and effective marker of cancer by accumulating more in malignant cells than normal cells [65, 66]. In addition to its clinical utility, PET is a useful tool in basic research, including the development of new therapies and novel pharmaceuticals in animal models [47]. New PET radionuclides with longer half-lives, such as ^{52}Mn ($T_{1/2}$ = 5.6 days) [9], ^{124}I ($T_{1/2}$ = 4.2 days) [67] and ^{89}Zr ($T_{1/2}$ = 3.3 days) [68], are developed for allowing longer-term PET studies.

1.3.3 NIR fluorescence imaging

Fluorescence refers to the ability of certain molecules that are able to absorb light at one particular wavelength and emit light at a longer wavelength [69, 70]. Fluorescence imaging uses a sensitive camera to detect the emission of fluorescent molecules, which are excited by an external light source and translate these results to evaluate the change of *in vivo* metabolism (Figure 1.5C). Unlike the above-mentioned imaging modalities (CT, SPECT and PET), fluorescence imaging has the benefits of providing functional images with high spatial resolution and avoiding the use of hazardous ionizing radiation [71]. Moreover, both endogenous and exogenous fluorescent probes are available for different purpose. The application of fluorescence imaging has a long history since 1924, when the autofluorescence of endogenous porphyrins were observed in tumors by the excitation of ultraviolet light [70]. Later in 1942, red fluorescence was observed in tumors after intravenous administration of porphyrins [70] and the use of fluorescein was reported in 1948 to improve the detection of brain tumors [72]. After these applications, many improvements in both camera and exogenous

fluorophores have emerged. However, the main limitation of fluorescence imaging is the poor tissue penetration of both excitation and emission light. The intensity of the light decreases dramatically in tissues due to the light-tissue interactions including interface reflection, in-tissue scattering, in-tissue absorption and tissue autofluorescence (Figure 1.6A) [71]. In order to decrease the effect of these light-tissue interactions, the near-infrared (NIR: 600 – 1700 nm) part of the spectrum was increasingly proposed to use for fluorescence imaging because of less absorption by hemoglobin and water (Figure 1.6B), less scattering, and less autofluorescence from surrounding tissues [71, 73]. So far, there are two FDA-approved dyes, indocyanine green (ICG) and methylene blue (MB), and two dyes in clinical Phase I test, IRDye800CW and zwitterionic cyanine dye ZW800-1. All these four dyes are excited and emitted in the NIR range of 600 – 900 nm, which is defined as NIR-I window. Dyes with longer excitation and emission wavelength of 900 – 1700 nm in NIR- II window were developed recently [71] and these dyes improved the penetration depth by further decreasing scattering and autofluorescence [71]. However, the current challenges to promote the fluorescence imaging in NIR-II window are the low quantum yield of the dyes, and the development of special detectors that are sensitive at longer wavelength [74].

The current clinical application of fluorescence imaging in cancer is mainly for superficial imaging or for surgical guidance due to its limited tissue penetration (<1 cm) [69]. Currently, both methylene blue (MB) and indocyanine green (ICG) are widely used in clinical NIR fluorescence guided process such as sentinel lymph node mapping and image guided surgery. Novel intraoperative real-time imaging systems, such as FLARE^{TM} [75] and SurgOptix [76], have been developed and are available for detecting MB (excitation/emission wavelength: 665/686 nm) and ICG (excitation/emission wavelength: 807/822 nm) respectively.

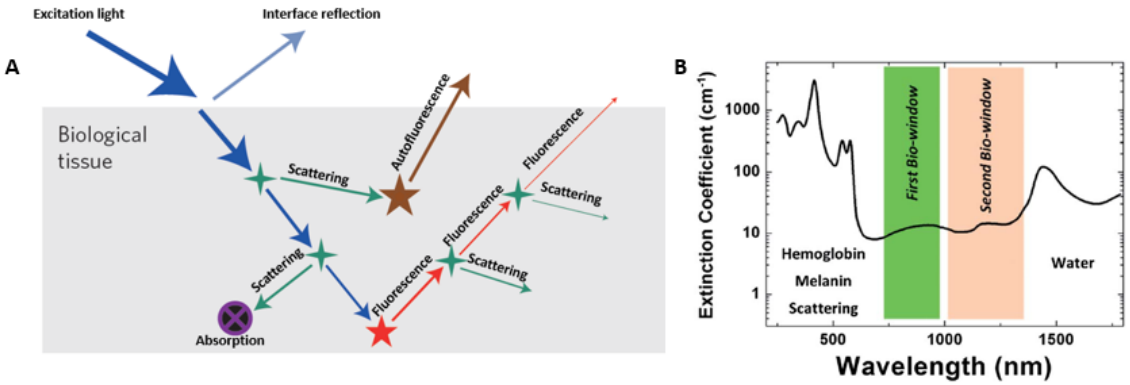

Figure 1.6. Light-tissue interactions resulting from impinging excitation light (A). Figure is adapted from [71]. Excitation coefficient of water and hemoglobin as a function of wavelength (B). Figure is adapted from [73].

1.4 Common treatments to cancer

The purpose of treatment to cancer is to remove or destroy the cancerous cells without damaging normal cells [77]. Chemotherapy, radiotherapy and surgery, which can be applied either alone or in combination with each other, are the most common types of cancer treatments available currently [4], [77]. These three types treatments are described in the following sections.

1.4.1 Chemotherapy

Chemotherapy is the treatment that uses one or more cytotoxic drugs to kill cancer cells by preventing cancer cells from dividing and growing. The era of chemotherapy started in 1940s with the first use of nitrogen mustards to treat lymphomas [4], [78], [79]. So far, several different classes of anticancer drugs have been developed and are available for cancer treatment. According to the mechanisms of action, anticancer drugs can be divided into: a) alkylating agents that damage DNA and are most active in the resting phase of the cell cycle; b) anti-metabolites that are similar to normal substance within the cell such as folic acid and pyrimidine, and interfere with the cellular metabolism; c) antibiotics that affect DNA replication by interfering with the essential enzymes; d) topoisomerase inhibitors that interfere with the action of topoisomerase I or II, which are involved in unwinding DNA during replication and transcription; e) mitotic inhibitors, which inhibit mitosis and cell division [77]. Table 1.1 lists some current anticancer drugs and their mechanisms. Note that platinum (Pt) coordination complexes (i.e. cisplatin) are classified as alkylating agents even though the compounds have no alkyl group due to their similar mechanism to DNA. More details will be described in Chapter 4.

Cancer is considered as a combination of interconnected disease pathway, hence, a single anticancer drug may not effective to eradicate cancer and causes the emergence of drug resistance and tumor recurrence [80]. The combinations of drugs provide effective solutions for the quandary by different mechanisms of synergistic, addictive or potentiation combination effects [81]–[84]. So far, chemotherapy has been verified to be curative and significantly improved overall survival in many types of advanced cancer, such as acute lymphoblastic and acute myelogenous leukemia, Hodgkin's and non-Hodgkin's lymphoma, germ cell cancer, small cell lung cancer and ovarian cancer.

Table 1.1. Some examples of current anticancer drug for chemotherapy

Classification	**Drug examples**
Alkylating agents	Cisplatin, Cyclophosphamide, Busulfan
Anti-metabolites	Methotrexate, 5-Fluorouracil, 6-Thioguanine
Antitumor antibiotics	Doxorubicin, Dactinomycin, Idarubicin
Topoisomerase inhibitors	Ironotecan, Etoposide, Amsacrine
Mitotic inhibitors	Paclitaxel, Docetaxel

Chemotherapy is normally administered as systemic treatment. Therefore, the patients with unresectable and metastatic cancer can benefit from chemotherapy alone or its combination with radiotherapy and surgery [77], [78]. The combination of chemotherapy with radiotherapy or surgery is achieved by either *adjuvant chemotherapy*, in which chemotherapy is applied after radiotherapy or surgery in curing patients with advanced cancer, or *neoadjuvant chemotherapy*, where chemotherapy is applied prior to surgery or radiotherapy in order to reduce the primary tumor size, prevent micrometastases and increase sensitivity of cancer cell to radiation [4].

However, the systemic circulation of anticancer drug can cause insufficient local concentration to kill cancer cells and damage to the normal cells that divide rapidly. Therefore, many researchers started to put effort on looking for specific targets to attach the cancer cells without damaging the normal cells, which is known as targeted therapy. So far, many specific targets, including growth factors, signaling molecules, cell-cycle proteins, modulators of apoptosis and molecules that promoted angiogenesis [78], [80] have been successfully developed for chemotherapy. One of the most famous compounds is Imatinib mesylate (Glivec), which is the first FDA approved anticancer compound for targeted therapy. Imatinib is a tyrosine kinase inhibitor against BCR-ABL, which is involved in the pathogenesis of chronic myeloid leukemia [85]. The using of antibodies is another effective treatment for targeted therapy. Antibodies, such as alemtuzumab [86], can be curative alone by binding to cancer cells and acting as a marker for the body's immune system to destroy them. Anticancer drugs can be modified and conjugated with antibodies, which take the anticancer component directly to the cancer cells. This kind of chemolabeled antibodies include Brentuximab vedotin targeting tumor cells expressing CD30 antigen, Ado-trastuzumab emtansine targeting human epidermal growth factor receptor 2 protein (HER 2) on the surface of cancer cells.

1.4.2 Radiotherapy

Radiotherapy is an important component of cancer treatment, which uses high-energy particles or waves including x-rays, gamma rays, electron beams, or protons to destroy cancer cells [87]. Radiotherapy has a long history since late 19th century when Becquerel and Rontgen discorded X-rays and radiation [4]. Until now, 50% of all cancer patients have received radiotherapy during their treatment and radiation therapy contributes towards 40% of curative treatment for cancer [88].

The principle of radiotherapy is using ionizing radiation to destroy cancer cells. The high energy radiation makes small breaks in the DNA of the cells, thus blocking their growing as well as dividing, and cause the death of the cells via various types (Figure 1.7) [89]. Although both normal cells and cancer cells can be damaged by radiation, normal cells can repair themselves to their normal function status at a faster rate than the cancer cells [90]. Radiotherapy is given by three ways, external beam radiotherapy (EBRT), internal therapy including brachytherapy and systemic radiotherapy. EBRT and brachytherapy are applied locally in the tumor site in order to increase the local radiation dose and decrease the unnecessary damage to normal cells. Systemic radiation, where radioactive tracers travel through the body, also exists to treat some certain types of cancer, but not relevant to this PhD work.

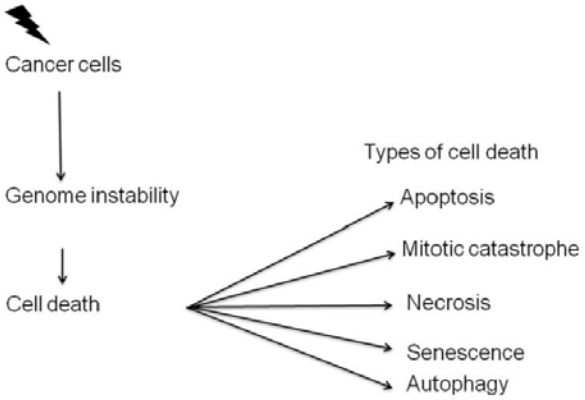

Figure 1.7. Types of cell death induced by radiation. Most cells are killed in apoptosis and mitotic catastrophe Figure is adapted from [88].

1.2.1.1 External Beam Radiotherapy

EBRT is the most commonly used radiotherapy for cancer treatment. During the treatment, high-energy rays is applied from the outside the body into the tumor. A linear accelerator (linac) is usually

used to aim the radiation, so that a high dose of radiation will only apply to the tumor with less damage to normal tissues. The radiation sources for EBRT were x-rays and radium initially, which are frequently used to treat skin cancers due to their low energy and short radiation range [91]. Later on, higher energy X-rays, and new radiactive isotopes, type of rays were discovered to treat deeper cancers [92] such as cobalt teletherapy, which produces high energy γ-rays [93]. However, with the increase in radiation energy and range of the radioactive sources, the risk to cause an excessive radiation in the tissue surrounding cancer also increased. A crucial progress in EBRT was achieved by the end of 1990s when 3D conformal EBRT emerged [91, 94]. In 3D conformal EBRT, imaging scans (such as a CT scan) of the patient are usually done before treatment, which allows the radiation oncologist to adjust the position of patients or the direction of radiations in order to deliver the radiation to the target precisely. Another new technology based on 3D conformal EBRT is intensity modulated radiotherapy (IMRT), which modulates and controls the intensity of the radiation beam in multiple small volumes and allows higher radiation doses to the tumor with minimizing dose to the surrounding normal tissues [95, 96].

As the margins of treatment become more conformal and tighter, the potential to miss the position of tumor due to breathing motion, changes in organ filling, and tumor size is the new challenge in EBRT [88, 97]. In order to improve the precision and accuracy of radiation, image-guided radiotherapy (IGRT) is currently being used, where frequent 2D (e.g. radiographic imaging) or 3D (e.g. CT, PET, MRI) are recorded before or even during each treatment [40, 98]. The introduction of IGRT, was recently demonstrated to simultaneously reduce the toxicity and improve the therapeutic efficacy for several tumor types including head-neck [99] and prostate cancer [100]. CT imaging is commonly used in IMGR, however, the localization of some soft-tissue tumor is challenging since the tumor is hard to identify from the surrounding soft tissues (low tumor/organ ratio). In this case, contrast agents, also termed as fiducial marker, are usually administered for a better tumor visualization. Currently, the intratumoral implantation of solid fiducial gold markers is commonly used in clinic to provide a better CT contrast of tumor for IGRT. However, the implantation of the large metal marker is invasive, and usually cause bleeding, organ damage or even pneumothorax to the patients due to the use of the large and specialized needles for insertion [101]. Moreover, the migration of the metal marker causing inaccuracy of tumor localization has also been observed. An injectable marker for intratumoral injection based on SAIB containing gold nanoparticles as well as a highly iodinated SAIB-derivative (BioXmark) has been developed by the Danish company Nanovi A/S [45, 46]. The marker was visible

and stable in position and size for up to 7 weeks, which is suitable for IGRT, especially for locally advanced lung cancer patients .

A novel concept of EBRT, emission guided radiotherapy (EGRT), has been developed by an American company Reflexion [102]. The instrument for EGRT combines PET imaging setup and beamlet for radiotherapy. A marker solution of FDG is intravenously injected into the patients prior to the treatment. As in conventional PET imaging, coincident photon pairs produced by positron annihilation are continually detected. Instead of forming PET images, the EGRT system delivers beamlets of therapeutic radiation along the paths of the coincidence photon pairs. Therefore, the accurate tracking and radiation delivery can be achieved at the same time by EGRT [103, 104, 105].

1.2.1.2 Brachytherapy

Brachytherapy is the treatment to place the radiation in or near the tumors to be treated permanently or temporally. Due to the high radiation doses applied to tumor with a low burden of radiation in the whole body, brachytherapy is gaining importance and attention in clinical oncology for the local treatment of solid tumors [106]. Based on the delivery dose rate, brachytherapy can be divided into three types. The international Commission on Radiation Units and Measurements defined the treatment with dose rate of 40 – 200 Gy/h as low dose rate brachytherapy (LDR-BT), 200 – 1200 Gy/h as moderate dose rate brachytherapy (MDR-BT), and >1200 Gy/h as high dose rate brachytherapy (HDR-BT) [107]. Two main types of brachytherapy implants exist, intracavitary, where radiation sources are placed in the body cavities close to the tumor, and interstitial, in which radiation sources are placed in the tumor directly [92, 106]. Other implants are also available such as surface, intraluminal, intraoperative and intravascular for some specific purpose [108].

HDR-BT is also known as temporary brachytherapy where the radioactive sources are delivered from a chamber through a series of thin catheters (Figure 1.8A). The catheters containing radioactive sources such as ^{192}Ir (380 KeV) or ^{60}Co (1.25 MeV) are temporarily placed in the tumor using real-time ultrasound image guidance [106]. HDR brachytherapy gives a powerful radiation to the tumor for only a few minutes every time, and the source is removed after each treatment. This procedure might repeat several times during the whole treatment, and the procedure is done under anesthesia. The length of time that radiation and the position of radiation can be freely programmed and controlled by computer during the procedure. HDR-BT was initially introduced as a high-dose-rate

supplement for EBRT, and it was proven as an effective and safe treatment [13, 109, 110]. Comparing to LDR-BT, HDR-BT is more popular to treat early staged prostate cancer. The advantage of applying HDR-BT is the dose of radiation can be well controlled over post-implant [106]. Nevertheless, the procedure of HDR-BR is fairly invasive, and it usually requires several sessions associated with a brief hospital stay [13]. Moreover, due to the inverse square law, the dose reduces exponentially with increasing distance from the radioactive source [111]. The radiation dose distribution of HDR-BT is heterogeneous, and highly depends on the position of the catheters. HDR-BT can only be used alone to treat relatively small tumors [112].

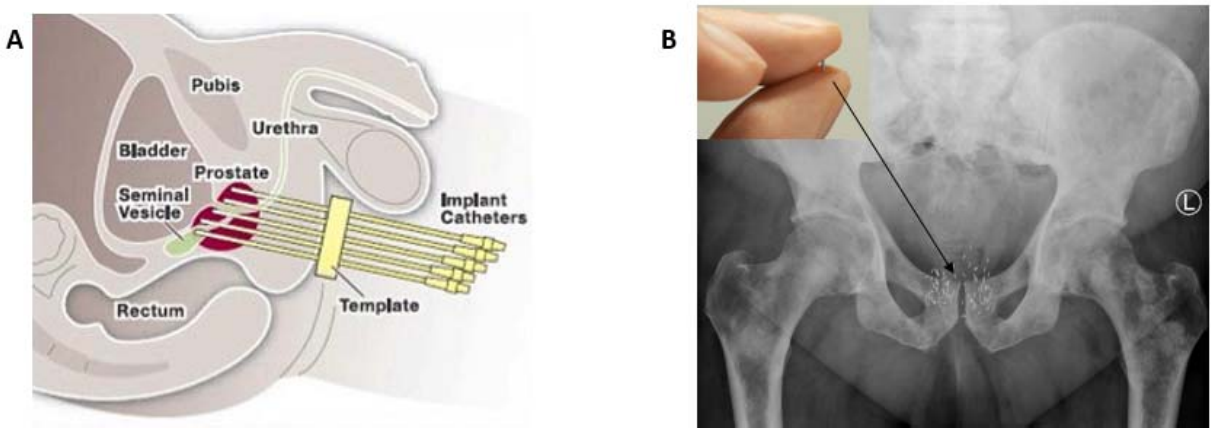

Figure 1.8. HDR-brachytherapy to prostate cancer (A) figure was adapted from https://www.tackleprostate.org. The seeds for LDR-brachytherapy and their CT images (B), figure was adapted from http://www.tccoh.com and https://radiopaedia.org.

In LDR-BT, a high dose of radiation but at a low dose rate is delivered by the permanent implantation of radioactive metal seeds in the tumor. Commonly used radionuclides in LDR-BT are iodine 125 [^{125}I], cesium 131 [^{131}Cs] and palladium 103 [^{103}Pd], all of which emit photons with energies in the 20-35 KeV range. Before implantation, the location, shape and volume of the tumor are determined by computer imaging in order to plan the radiation dose required and optimize the distribution of the metal seeds [106]. During the actual implantation, the titanium seeds with the lengths of about 4.5 mm are injected into tumor such as prostate gland by long needles under CT or ultrasound image guidance, and this procedure is done under general anesthetic. It typically requires 70-150 radioactive seeds to be inserted into the tumor (Figure 1.8B). Patients usually undergo one-day practical procedure and receive a long-term treatment for several months with lower complication rate such as bleeding and urinary incontinence during and after the procedure [13]. LDR-BT presents the most conformal radiotherapy and it has been a gold standard to treat prostate cancer for many years. Despite its high clinical efficacy, there are still certain limitations of LDR-BT. The implantation of so many

metal seeds requires a high level of surgical skill in order to place these seeds accurately and uniformly [113], [114]. The non-degradable and non-biocompatible metal seeds may cause serous inflammation and discomfort to the patients [115, 116]. Moreover, the dose distribution of LDR-BT is heterogeneous in line with HDR-BT.

In summary, the main limitations of brachytherapy is the invasive procedure to the patients and the heterogeneous dose distribution in the tumor region. Using biodegradable, biocompatible and injectable materials to deliver radiation to the tumor is a rational and promising approach to improve brachytherapy. Liu and co-workers have reported a radioactive hydrogel depot consisting ^{131}I, which was formed by polypeptide micelles [32]. ^{131}I was well retained in the depot for over 60 days in both prostate and pancreatic tumors with very low radiation dose to healthy tissues. However, the point-sources employed in this system result in a heterogeneous distribution of radiation in line with conventional metal seeds [117]. Liposomes are potential carriers to provide a long intratumoral retention and a relatively homogenous distribution of radiation due to their large size and the ability to infuse throughout the tumor interstitial space [26]. Recent studies have suggested using liposomes carrying beta-emitting therapeutic radionuclides such as ^{186}Re and ^{188}Re to treat glioblastoma [118], head cancer or neck cancer [119, 120]. Gold nanoparticles have been found to provide a more homogeneous distribution of ^{103}Pd in comparison to conventional metal seeds [121]. Thermosensitive hydrogel based on Pluronic® F-127 and sodium hyaluronate consisting of micron or small sized radiation sources was recently developed by Lim et al. [122]. The hydrogel was a water-like fluid at low temperature and polymerized into a gel like semi-solid at body temperature. Upon injection, the small size radiation sources ^{111}In are continuously released from the depot to tumor region for 50 hours resulting in a homogenous distribution of radiation. However, the kidney accumulation of ^{111}In was considerable. Our group have developed a series of formulations based on carbohydrate esters such as SAIB and LOIB for brachytherapy. A releasing formulation was designed for medium/low-energy beta-emitter with short tissue penetration, such as ^{177}Lu, in order to achieve a homogenous distribution of the radiation. On the other hand, for delivery high-energy beta-emitter with long radiation range such as ^{90}Y, a non-releasing formulation was designed to prevent the radiation to healthy tissues.

1.4.3 Surgery

Surgery is the approach to completely remove cancerous tissue, while preserving as much of the health tissue as possible. Surgery is the most effective treatment for localized solid tumor without metastasis, and can be applied alone or combined with post-operative chemotherapy and radiotherapy [6]. In this process, it is crucial to delineate the location and boundary of tumors as well as their interaction with healthy surrounding tissues in order to avoid positive margin resection and the damage to other tissues [123]. The surgeons should try to avoid cutting into or across the tumor during the procedure in order to lower the chance that cancer cells spread or scatter to other healthy tissues. These requirements are quite difficult to achieve if surgeons identify the tumor by eyes or palpation during the procedure. *Ex vivo* histologic validation of excised tissue is the gold standard to determine if the resected tissue contains tumor on the margin [123, 124]. The validation ensure the complete resection of the tumor during the surgery. Unfortunately, many cases are required to repeat the surgery due to the uncomplete resection, which is costly and cause more discomfort to the patients. Small-sized solitary nodules are increasingly identified at early stages due to screening programs, and these non-palpable nodules are not possible for surgeons to identify during the surgical procedure. Consequently, the procedure is postponed until the nodule has grown to a palpable size. Such delays are unsatisfactory and increase the risk of progression to metastatic cancer, which significantly worsens prognosis and increases treatment associated costs. Currently, pre-operative structural or functional images localizing and delineating the tumor can be provided by some advanced imaging modalities such as CT, PET and MIR. However, these systems are not available to use during the procedure in the operating room due to their large hardware footprint, the use of ionized radiation, slow image reconstruction, high cost and specialized operator requirement [123, 125].

In order to localize the tumor during surgery, some preoperative markers, which are able to localize the position of tumor have been clinically used. Surgery with wire-guided localization (WGL) is the oldest and current gold treatment for non-palpable breast tumors [126], where a wire with a small hook at the end is inserted into breast pointing to the tumor by CT or ultrasound guidance. The surgeon will remove the piece of tissue around the hook during surgery. Some disadvantages of this method have been reported, such as inaccurate localization due to wire migration, high positive margins rate and invasive procedure [46, 127, 128]. Therefore, some other localization methods have been reported to minimize the problems of WGL. Radio-guided occult lesion localization (ROLL) is the method to inject technetium-99m [^{99m}Tc]-labeled particles to the tumor region under guidance by

stereotactic mammography. The radioactivity in the tumor region allow surgical excision guided by a handheld gamma ray detection probe [129]. It has the advantage of detecting sentinel lymph node during the same injection. Unfortunately, the radioactive particles are not visible by CT and ultrasound scanning [128]. Moreover, the window for surgery is short due to the 6 h half-life of ^{99m}Tc [130]. Radioactive seed localization (RSL) is similar to ROLL, where Iodine 125 [^{125}I] radiolabeled metal seeds are implanted into tumor by the guidance of CT or ultrasound and the radioactivity in the tumor can be detected by a gamma probe during surgery. Due to the long half-life of ^{125}I (59.4 days), the seeds can be implanted up to 5 days prior to the surgery [131]. The metal seeds are less likely to migrate than wire, so that RSL can provide a more accurate tumor localization. However, the metal seeds are injected into tumor with a wide-gauge (17G) [132], which is considered as an invasive and unpleasant procedure to the patients. The development of markers based on injectable biomaterials that enable surgical guidance with accurate localization, reduced patient discomfort and decent contrast is highly desired. A ^{125}I radiolabeled marker containing CT contrast (BioXmark) based on SAIB has been reported recently [46]. The marker can be delivered through thin hypodermic needles (>25G) to the tumor by CT image guidance, and it is detected by a potable gamma probe during surgery in line with ROLL and RSL. The marker was proved to be stable in the position for seven days, and the radioactivity was well remained in the marker, which limits the exposure to healthy tissues.

Real-time image-guided surgery (RT-IGS) is another novel technology that allow for highly accurate surgery by providing intraoperative spatial position of the marker with relation to the preoperative images [133]. Unlike only tracking a marker that creates discontinuous workflow, RT-IGS updates the location of the marker continuously by real-time images [134]. Video-assisted thoracoscopic surgery (VATS) is a minimally invasive procedure to remove the tumor in lungs, where a small camera probe is placed inside of patients and the tumor and surrounding tissues are recorded in real time. Intraoperative MRI has been recently reported to provide a more effective and safer procedure than conventional surgery in glioblastoma [135]. NIR fluorescence imaging is increasingly gaining attention in RT-IGS due to the high detection sensitivity and high spatial resolution (Figure 1.9) [136], [137]. Currently, there are several mounted, handheld or wearable such as goggle NIR fluorescence imaging systems are available and most of them are designed for ICG guided surgery [123]. ICG has been intravenously injected into patients to visualize e.g. colorectal hepatic metastases and hepatocellular carcinoma (HCC) [138]. In a similar manner, ICG was used to identify tumor in breast cancer patients by the delayed clearance because of angiogenesis in the area of the tumor [139]. For

increasing the circulation time of ICG and an effective EPR-mediated tumor accumulation, Jaffray et al. have reported a multimodal liposomal maker for intravenous injection consisting of ICG and a CT contrast agent for RT-IGS [140]. The application of the marker successfully combined preoperative CT with >200 Hounsfield units enhancement as well as intraoperative NIR fluorescence images with >5-fold tumor-to-background ratio.

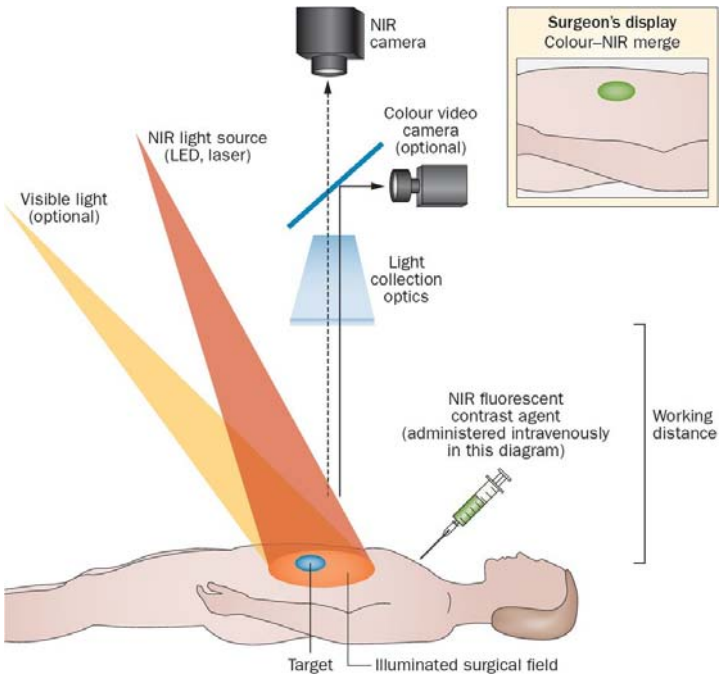

Figure 1.9. A Schematic presentation of NIR fluorescence image guided surgery. NIR fluorescence contrast agents are injected intravenously, topically or intrapenchymally. During surgery, the agents are visualized by NIR fluorescence imaging system including excitation light, collection NIR camera that sensitive to emission light with the wavelength in a specific range. The surgeon's display can be standard computer monitor or goggles. Figure is adapted from [125].

So far, only two FDA-approved dyes, ICG and MB, are available for clinical use. Even though MB is able to accumulate in some tumors, the interference from autofluorescence and other visible dyes in the similar emission range limits its use in RT-IGS [123]. Therefore, the development of new NIR dyes or formulations with the properties of high quantum yield, target to tumor, long-term stability are highly relevant to improve the current state of fluorescence image guided surgery. Moreover, fluorescence imaging has the disadvantages of the limited penetration depth of emitted light in tissue. The combination of fluorescence and radioactivity detection can be one of the strategies to solve the problem. A marker of ^{111}In radiolabeled fluorescent antibody for intravenous injection that target to prostate specific membrane antigen was recently reported [141]. By using the marker, surgeon can firstly use a gamma probe to roughly localize the tumor. Once the surgical field is exposed to the

surface, fluorescence images are able to precisely evaluate resection margins as well as detects micrometastases. As the development of portable gamma cameras that are using in clinical sentinel lymph node mapping, the combination of intraoperative NIR and SPECT images might also be possible and promising to guide surgery in future.

1.5 Concluding remarks

As has been demonstrated, the commonly used clinical treatments have their own shortcomings, which could be improved by using novel drug delivery systems. The *in vivo* behavior of these drug delivery systems could be better understood by using imaging modalities. Therefore, the works presented in this thesis aim to design delivery system to improve the current treatments. In the following chapters, different novel drug delivery systems will be presented for the application in imaging guided surgery (Chapter 2), brachytherapy (Chapter 3) and chemotherapy (Chapter 4).

Chapter 2. Development of Multimodal Fiducial Markers for Surgical Guidance

2.1 Background

Lung cancer is the most common cause of death (1.69 million in 2015) with a high coincidence rate [142]. Poor prognosis of lung cancer usually occur due to the late diagnosis, often at advanced stages. Surgical resection is the main treatment for non-small lung cancer (NSCLC), which accounts for 80% of all lung cancers [143]. With the development of screening programs and diagnosis technologies, small-sized solitary pulmonary nodules (SPNs) are increasingly identified at early stages. Ideally, such SPNs should be removed by video assisted thoracic surgery (VATS) at the time of diagnosis to prevent the progression of the disease. VATS has been considered as an effective treatment for lung cancer since its rapid and safe resection results in a lower chance of infection and patient discomfort [144].

However, many SPNs are not possible for surgeons to identify and remove during surgery, because they are non-palpable due to their small size or long distance from the pleura. Consequently, the VATS procedure is postponed until the nodule has grown to a palpable size. Such delays are unsatisfactory and increase the risk of progression to metastatic cancer, which significantly worsens prognosis and increases treatment associate costs. In order to assist surgeons in identifying the position of the tumor during surgery, markers are usually utilized to accurately locate the tumor tissue, which is to be removed by VATS procedures. Then the surgeon would be able to remove even the smallest detectable SPN by identifying the position of the marker.

The development in resolution and sensitivity of diagnostic imaging technologies including computed tomography (CT), magnetic resonance imaging (MRI), positron emission tomography (PET) and single-photon emission computed tomography (SPECT) have revolutionized identification and diagnosis of cancer at early stages. Based on these technologies, markers can be positioned and identified during surgery. Such markers are intensively explored for preoperative and intraoperative target localization and navigation. The present markers for surgical guidance include hook wire, which is visible by ultrasound and CT, and technetium (^{99m}Tc)-labeled nanoparticles, which could be detected by gamma probe. Hook wire is an unpleasant and painful procedure to patients and the wire has the potential to migrate prior or during the surgery [145]; ^{99m}Tc-labeled nanoparticles can only

be used during surgery with no preoperative information, since they are not visualized by anatomical imaging techniques [130]. More details on hook wire and ^{99m}Tc-labeled nanoparticles localization can be found in Chapter 1 (section 1.4.3). Consequently, it is highly desired to develop an implantable marker that is non-invasive to patients, visible on diagnosis, easy to locate during surgery at any tissue depth and stable after placement without migration. NIR fluorescence imaging is increasingly gaining interest in surgery, due to its high quality images with high spatial and temporal resolution. Currently, two FDA-approved dyes, methylene blue (MB) and indocyanine green (ICG), are widely used in clinical NIR fluorescence guided process such as sentinel lymph node mapping and image guided surgery. However, the systemic distribution of the solution containing ICG or MB for intravenous injection could result in a poor guidance. Moreover, the penetration depth of fluorescence in tissues is limited [123]. Therefore, the combination of NIR imaging with other imaging modalities, or the development of novel formulation and NIR dye are relevant for surgical guidance.

Design of tumor-targeted compounds and novel drug delivery systems have been utilized to deliver imaging contrast to the tumor in order to increase the contrast in tumor during surgery. Gelovani et al. have reported a dual probe targeted to αvβ3 integrin, which correlated with tumor progression, angiogenesis and metastasis [146]. The probe consisted of a RGD peptide that had a high affinity and specificity for αvβ3 integrin, an ^{111}In chelator diethylenetriaminepentaacetic acid (DTPA), and the NIR fluorescent dye IRDye800 (excitation/emission, 765/792 nm). The probe had a higher uptake in the mice with αvβ3-positive M21 melanoma than in those with αvβ3-negative M21-L melanoma at 4 – 48 hours after intravenous injection. A liposome contrast agent for intravenous injection loaded with ICG and iohexol for NIR and CT imaging was reported by Jaffray et al. [140]. Due to the long lasting accumulation of liposomes at the tumor site, the preoperative and intraoperative imaging could be conducted between 24 hours and 4 days post-injection. Intratumoral injectable liquid formulations based on sucrose acetate isobutyrate (SAIB) were recently reported as highly stable contrasts for different purposes. BioXmark, a SAIB-based marker composed XSAIB for CT image-guided radiotherapy, was visible and stable in size and position throughout treatment in 7 weeks [45]. Later on, a ^{125}I-radiolabeled SAIB derivative was synthesized and combined with BioXmark for both preoperative CT imaging and intraoperative gamma detection [46]. The dual functional marker could be implanted into tumor at least 7 days prior to surgery because of the long half-life of ^{125}I (59 days).

2.2 Objective

In this study, we aimed to develop an injectable multimodal fiducial marker based on SAIB (Scheme 2.1A) with ethanol. SAIB is a promising modern biomaterial, which has been approved by FDA as generally-recognized-as-safe (GRAS). The viscosity of the marker is dramatically reduced when diluting SAIB with ethanol (20% v/v) and this enables injection by a thin needle [41, 46]. The fluid marker is also compatible with state-of-the-art electromagnetic navigation bronchoscopes [147] (Figure 2.1B), which enables the placement of the marker with high precision. Therefore, the marker has high potential for increasing the use of minimally invasive VATS procedures. It will reduce the discomfort and post-operative pain for the patients, improving survival and lowering healthcare costs. Upon injection in soft tissue, ethanol diffuses into surrounding environment causing its hardening into a highly viscous gel-like material [40, 41], which minimizes the risk of migration. Moreover, the enhanced viscosity property of the material provide stronger ultrasound reflections, rendering the material highly visible in ultrasound imaging.

The marker consists of the CT contrast agent xSAIB, an iodine-rich sugar ester (Scheme 2.1B), and 2,11,20,29-tetra-tert-butyl-2,3-naphthalocyanine (PC, scheme 2.1C), a near-infrared (NIR) fluorophore that enable both fluorescence imaging as well as the complexation of $^{64}Cu^{2+}$ ($T_{½}$ = 12.7 h) for positron emission tomography (PET) and gamma detection of annihilation photons. Therefore, the intraoperative application of the marker benefits the advantages of both improved penetration depth from radiation detection and high resolution images from NIR fluorescence imaging to provide accurate intraoperative location of tumor. Moreover, unlike the abovementioned NIR imaging guidance using ICG or MB solution, highly hydrophobic PC would not diffuse from the marker after the injection into the tumor site. Therefore, the marker would provide a high contrast of fluorescence intensity over time.

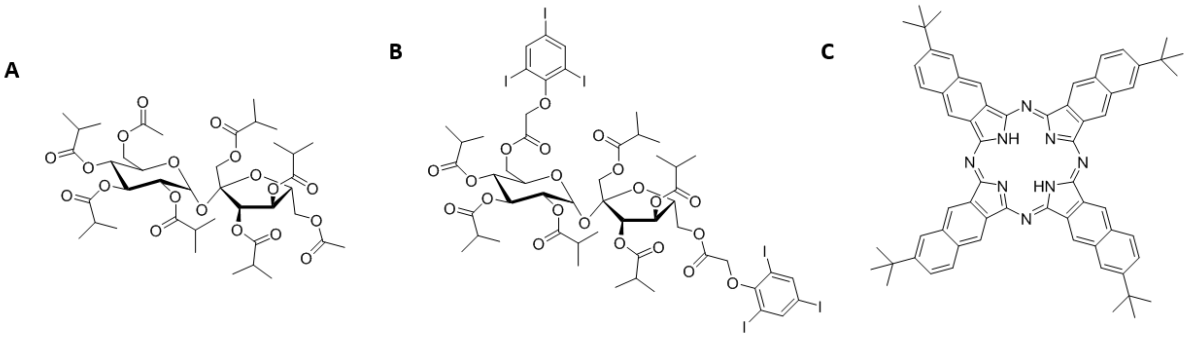

Scheme 2.1. Chemical structure of contrast agents: SAIB (A), XSAIB (B) and PC (C).

Figure 2.1 presents the application of the marker in surgery. SPNs are initially diagnosed via CT screening. The multimodal markers are able to be injected to the region in or close to the SPNs under the guidance by using ultrasound or CT. Preoperative information for the surgery plan can be provided by CT and PET images. During surgery, the position of the marker can be initially detected by a handheld gamma probe. Once the surgical field is close to the marker, the margins of the marker and the tumor are able to be accurately evaluated by real-time fluorescence images, which ensures the completely resection of lesion with a low rate of positive resection margins.

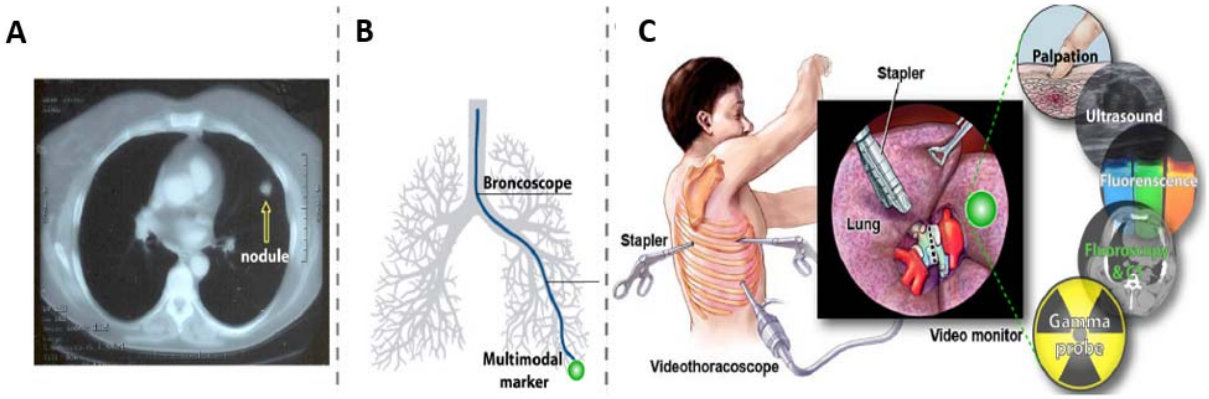

Figure 2.1. The application of the marker in surgery. Early stage detection of SPNs via CT based screening (A). Novel multimodal markers are injected using ENB bronchoscopy to the small non-palpable nodules (B). Video assisted thoracic surgery is guided by the new multimodal marker via palpation, ultrasound, fluorescence, fluoroscopy or gamma probe detection (C).

2.3 Results

2.3.1 *In vitro* optical characterization and release of PC in markers

2.3.1.1 Absorption and fluorescence spectra of PC

The absorption and full fluorescence spectra of PC in the marker (0.001% w/w) are presented in Figure 2.2. PC strongly absorbs light at around 700 nm and emits light in NIR-I region (700 – 1000 nm) with maximum fluorescence emission wavelength (λ_E) of 788 nm. The NIR dyes with longer-wavelength photons >700 nm have the advantages to facilitate deep-tissue imaging with high signal to background ratio (SBR) by decreasing the interaction of photon with tissue (i.e. photon scattering, absorption and auto fluorescence) [71].

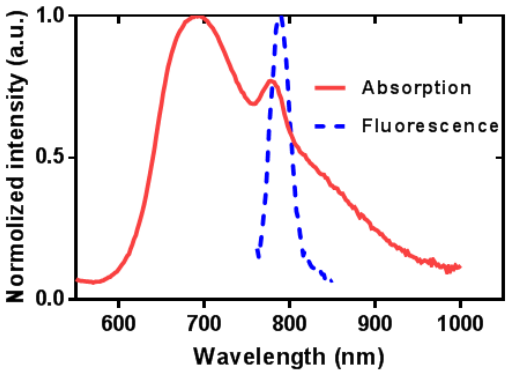

Figure 2.2. Normalized absorption and fluorescence spectra at the excitation wavelength of 700 nm of the marker (SAIB:xSAIB:EtOH 70:10:20) with 0.001% w/w PC. The full fluorescence spectrum was measured by cuvette fluorescence spectrometry assay.

2.3.1.2 Self-quenching of PC

In order to obtain the brightest marker, the optimal concentration of PC in the marker was investigated. The fluorescence intensity of the dye usually depends on the dye concentration in a solution. We have prepared a series of markers with different PC concentration to investigate the impact of PC concentration on fluorescence intensity and identify the marker formulation with the highest fluorescence intensity. Two different assays, cuvette based fluorescence spectrometry and surface fluorescence imaging, were utilized to measure the fluorescence intensity of PC in the marker. In the cuvette based fluorescence spectrometry assay, the excitation light goes through the cuvette and the marker solution, and only emission from the fluorophore in the center of the cuvette is detected at 90^{o} (Figure 2.3A). The fluorescence spectra (Figure 2.3B) of PC in the markers (SAIB:xSAIB:EtOH 70:10:20) were obtained from cuvette fluorescence spectrometry. PC in the markers (SAIB:xSAIB:EtOH 70:10:20) displayed fluorescence emission intensity dependence on the fluorophore concentration. Figure 2.3C summarizes the change of fluorescence as a function of PC concentration. The fluorescence intensity increased with the increase of PC concentration in the range of 0.00001% - 0.001% w/w. However, the fluorescence intensity of PC dropped rapidly when the PC concentration increased further >0.001% w/w because of quenching. The optimal concentration of PC in the marker that displayed the highest fluorescence intensity was found as 0.001% w/w.

In the surface fluorescence imaging assay, the fluorescence emission might be mainly obtained by the fluorophores on the surface of the marker (Figure 2.3D). We hypothesized that the excitation light

did not pass though the marker. In this case, the attenuation and absorption of light was less in

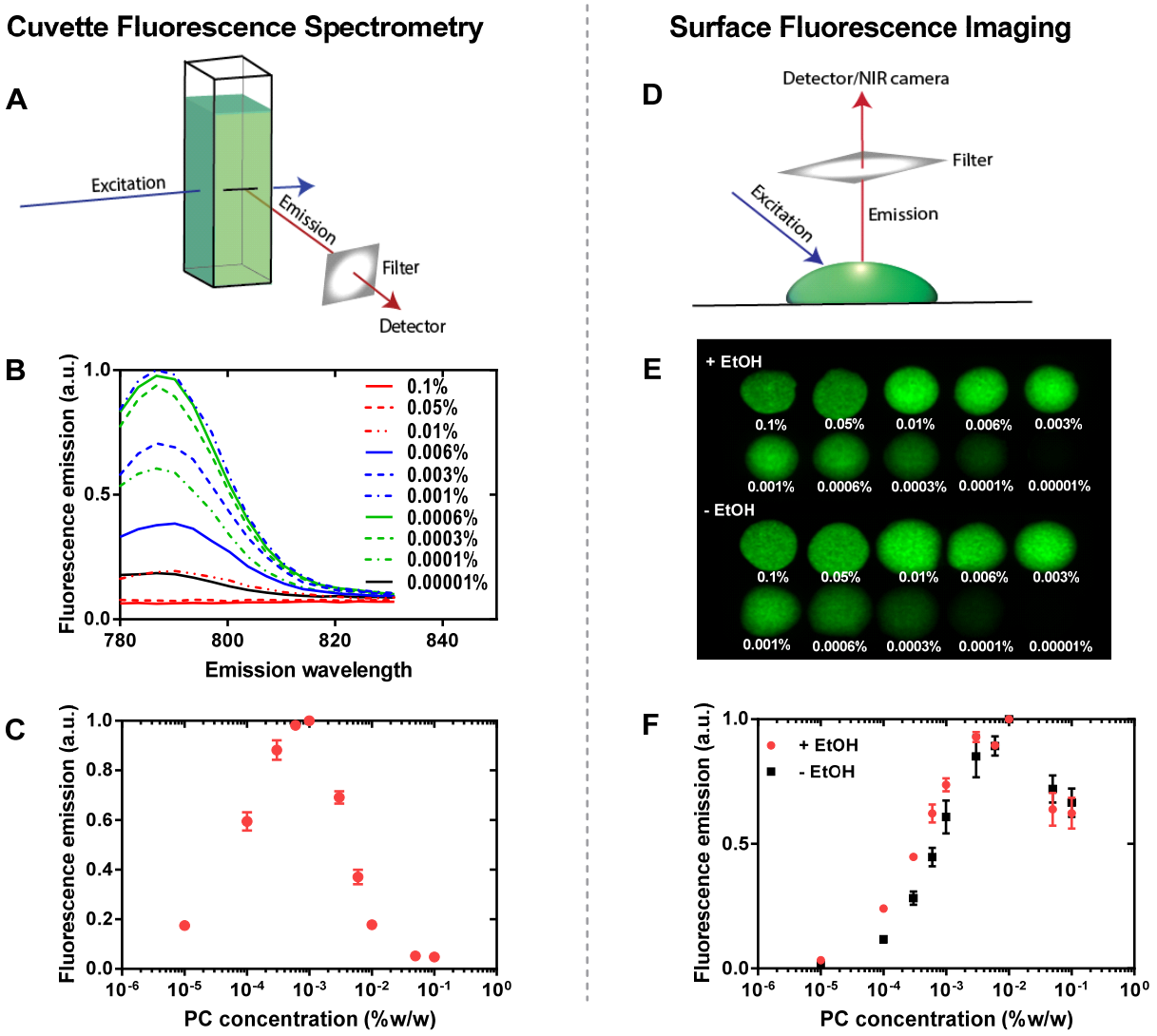

Figure 2.3. Fluorescence measurement of the marker (SAIB:xSAIB:EtOH 70:10:20). (A-C) Fluorescence measured by cuvette fluorescence spectrometry. Principle of cuvette fluorescence spectrometry (A); normalized Fluorescent spectra (B) at maximum excitation wavelength of 768 nm of PC markers with varying concentrations of PC; normalized fluorescent intensity as a function of PC concentration at excitation wavelength of 768 nm and emission wavelength of 788 nm (C), and the results are presented as mean ± SEM (n = 3). (C-E) Fluorescence measured by surface fluorescent imaging assay. Principle of surface fluorescent imaging assay (D); surface fluorescence images of markers, and the markers after evaporation ethanol with different PC concentrations at excitation wavelength of 785 nm emission wavelength of around 800 nm (E); Normalized fluorescence (F) of markers, and markers after evaporating EtOH as a function of PC concentrations, the results are presented as mean ± SEM (n = 3).

comparison to the cuvette fluorescence spectrometry. Surface fluorescence images at excitation wavelength of 785 nm and emission wavelength of around 800 nm were collected (Figure 2.3E), and

the brightest marker was found with a PC concentration of 0.01% w/w, which was 10-fold higher than the optimal concentration (0.001% w/w) measured by cuvette fluorescence spectrometry. In the clinical procedure (see Figure 1.9 in Section 1.4.3, Chapter 1), the fluorescence signals are collected mainly by the fluorophores on the marker surface, and the principle is very similar to surface fluorescence imaging assay. Therefore, the optimal concentration (0.01% w/w) of PC obtained from surface fluorescence imaging assay was further evaluated *in vivo*.

2.3.1.3 Effect of ethanol on the fluorescence emission of PC

As mentioned in previous studies [40, 46], ethanol diffuses out of the marker into surrounding aqueous environment once the marker is injected in soft tissues. Therefore, the influence of ethanol on the fluorescence of PC in the marker was investigated. Ethanol was removed from the marker by storing the marker in the vacuum oven at 55 ℃ overnight. Surface fluorescence images of the markers with different concentration of PC were collected before and after removing ethanol (Figure 2.3 E). No significant effect of ethanol was observed on the brightness of markers with the same PC concentration, and the optimal PC concentration was still 0.01% after the removal of ethanol.

2.3.1.4 Effect of Cu^{2+} on the fluorescence emission of PC

Cu^{2+} was found to quench the fluorescence of organic dyes and fluorescent proteins by donor atoms or chelating groups of the fluorophore [148, 149]. Because the final marker solution is radiolabeled with $^{64}Cu^{2+}$, the effect of Cu^{2+} on the fluorescence intensity of PC in the marker (SAIB:xSAIB:EtOH 70:10:20) was tested by adding different amount of $CuCl_2$ to the marker. Both absorption (Figure 2.4A) and fluorescence intensity (Figure 2.4B) of the marker with PC decreased with an increased concentration of Cu^{2+} in the marker. Therefore, the results indicated that Cu^{2+} could decrease the fluorescence intensity of the marker with PC. The reason of this phenomenon might be the formation of the PC-Cu complex, and the complex could still absorb light but dissipated energy in a non-fluorescence manner.

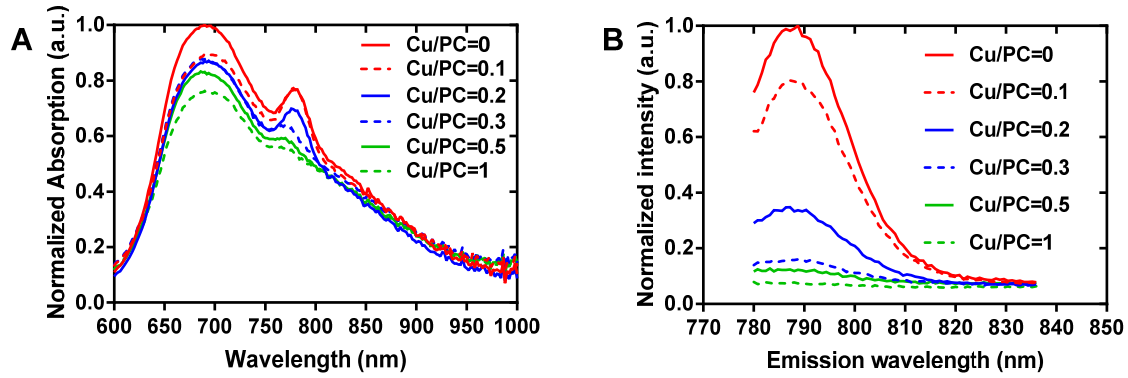

Figure 2.4. Quenching of PC by coordination to Cu^{2+}. Normalized absorption (A) and fluorescence spectra (excitation wavelength: 768 nm) (B) of markers (0.001% w/w PC) with different amounts of Cu^{2+}. The ratios in the figures present the molar ratio of Cu^{2+} and PC (Cu/PC) in the markers.

However, the final marker for *in vivo* study contained only 180 nM non-radioactive Cu^{2+} (specific activity > 1 TBq/µmol Cu) at preparation. The PC concentration in the marker was 0.01% w/w corresponding to about 107 µM in the marker. The concentration of PC was about 600-fold excess to Cu^{2+}, therefore, the influence of $^{64}Cu^{2+}$ on the fluorescence emission of the marker is neglected.

2.3.1.5 In vitro release of PC

An optical marker should have the property of long-term brightness in order to provide surgeons with enough time for the procedure. The release of PC from the marker to surrounding tissues might cause insufficient contrast and high background signal. Therefore, *in vitro* release of PC was studied by injecting the marker with the highest PC concentration (0.1% w/w) into PBS buffer. Due to the low solubility of PC in buffer, the standard curve of PC in buffer could not be achieved. Thus, a standard solution corresponding to 10% PC in acetonitrile was prepared and compared with the release samples. Figure 2.5 presents the absorption spectra of the PBS release buffer on day 6 post injection and the standard solution. Less than 10% of PC was released from the marker within a time frame of 6 days.

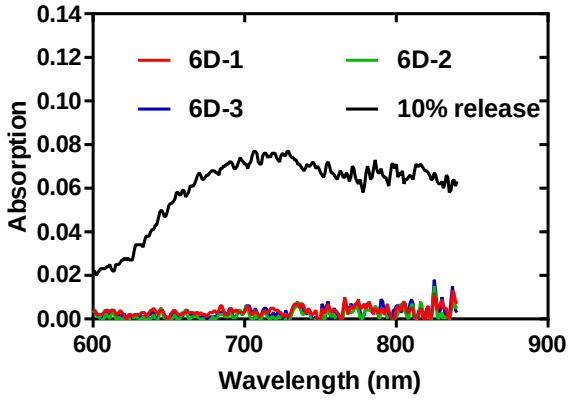

Figure 2.5. In vitro release of PC dye from the marker. UVvis spectra of PC in the PBS release media on day 6 after injection into buffer (conducted in triplicate). A standard corresponding to 10% release was included for reference.

2.3.2 Radiolabeling of the marker

2.3.2.1 Formation of a ^{64}Cu-PC complex

The ^{64}Cu-PC complex can be formed by substituting two central active hydrogen atoms with Cu^{2+} in the tetrapyrrolic macrocycle of PC [150]. In order to confirm the formation of ^{64}Cu-PC complex, a non-radioactive reference compound Cu-PC in the marker was prepared by an analogous method to the radiolabeling process. The resulting product was analyzed by MALDI-TOF MS and the mass spectrum has confirmed the formation of Cu-PC complex (Figure 2.6)

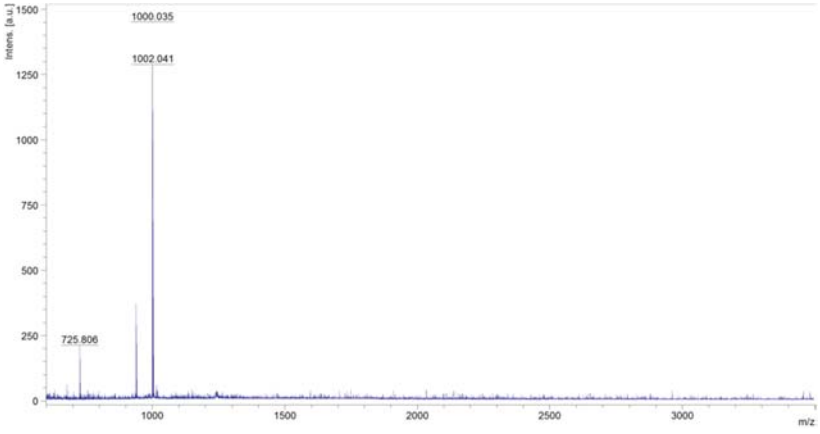

Figure 2.6 Mass spectra of Cu-PC complex. The peak of 1000 presents the mass of $[PC\text{-}Cu]^+$ complex. The peak of 1002 presents the mass of PC-Cu complex + H.

The resulting compound was analyzed by TLC and the R*f* of resulting Cu-PC complex was about 0.8. The radiolabeling of marker was simple and fast within 2 hours, with a high radiochemical purity

(RCP) of >95%. The analysis of radio-TLC gave an R*f* of about 0.8 to ^{64}Cu-PC complex, which was the same as the R*f* of non-radioactive complex. In contrary, free ^{64}Cu in the marker without PC stayed at the origin.

2.3.2.2 Transfer efficiency of radioactivity

Radionuclides of high specific radioactivity with short half-lives represent non-weighable trace amounts. Such small amounts of compound might behave very different comparing with macrocomponents, especially if the system contains interfaces of liquid/solid, gas/solid or liquid/liquid [151]. On the surface of glass vials, ion-exchange adsorption can take place due to the ability of silanol groups to bind metal ions [151]. Therefore, $^{64}Cu^{2+}$ may adhere to the glass wall instead of dissolving in the liquid, which can result in a non-quantitative transfer efficiency. The *transfer efficiency* is defined as the ratio of the measured radioactivity to the theoretical radioactivity of the marker that was transferred to another vial. The transfer efficiency of the marker with PC was higher than that of the marker matrix without PC (Figure 2.7). However, only significant difference ($p < 0.05$) in transfer efficiency was found between the marker with 0.01% PC and marker matrix. The chelating agent, PC, can form a stable complex with $^{64}Cu^{2+}$ in the marker. The complex is more stable than the weaker coordination of Cu^{2+} in the marker. Therefore, a higher transfer efficiency can be achieved. Comparing the transfer efficiency of two markers with PC, the higher concentration of PC resulted in a slightly but not significantly higher transfer efficiency ($p = 0.067$).

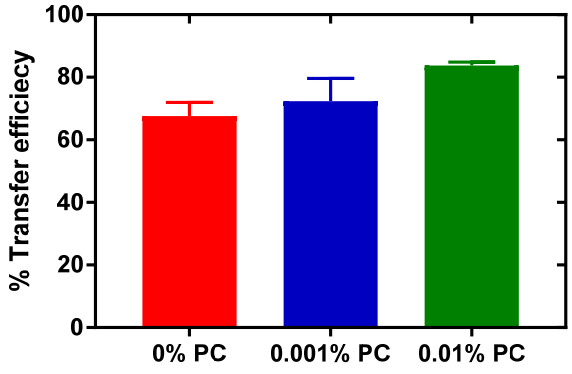

Figure 2.7 Transfer efficiency of ^{64}Cu radiolabeled markers (SAIB:xSAIB:EtOH 70:10:20) given as function of PC concentration. The concentration of radioactivity was 300 MBq/mL for all the formulations. Data are presented as mean ± SEM, n = 3.

2.3.2.3 In vitro release of ^{64}Cu-PC

Due to the abundant beta emissions and high linear energy transfer (LET) Auger electrons from the ^{64}Cu decay [152, 153], there is a risk to cause damage to health tissues if ^{64}Cu leaks from markers and diffuse to healthy tissues. Moreover, the leakage of ^{64}Cu will increase the signal of background during the procedure. Therefore, the *in vitro* and *in vivo* release of radioactivity from markers was studied. For the *in vitro* studies, marker matrix without PC was utilized as control and markers with two different PC concentrations (0.001% and 0.01%) were compared by injecting each marker into a release medium containing 10 mM TRIS, 1 mM EDTA, and stealth liposomes with 5 mM lipid concentration. EDTA and stealth liposomes were added into the release medium as a sink condition mimic. A rapid burst release of ^{64}Cu was observed from the marker matrix without PC (about 80% in 6 hours, Figure 2.8). The solubility of hydrophilic $^{64}Cu^{2+}$ is higher in ethanol that diffuse out and the water diffuse in the marker than hydrophobic SAIB, and the burst release might be attribute to the rapid solvent exchange of ethanol and water once the marker was injected into release medium. Markers containing 0.001% or 0.01% w/w PC exhibited limited release of less than 2% or less than 0.4%, respectively on day 6. The presence of PC results in the formation of a ^{64}Cu-PC complex, which is hydrophobic and more soluble in SAIB than ethanol. Lower release of radioactivity was observed from the marker with highest PC concentration (0.01%) in comparison with the release from the marker with low PC concentration (0.001%). The higher concentration of PC promotes the formation of ^{64}Cu-PC complexes, and hence most ^{64}Cu was chelated and retained in the 0.01% PC marker. However, the difference of free ^{64}Cu amount in two markers was not detectable by radio-TLC.

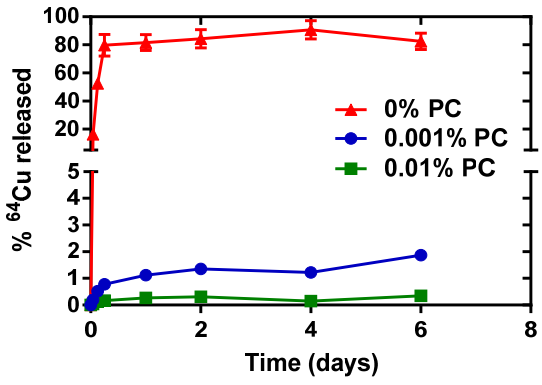

Figure 2.8. *In vitro* release of ^{64}Cu into TRIS buffered EDTA liposome containing media given as function of time for the markers (SAIB:xSAIB:EtOH 70:10:20) containing varying PC concentrations. The initial concentration of radioactivity in the marker was 300 MBq/mL. The radioactivity in the release medium was measured by liquid scintillation. The results are reported as mean ± SEM, n = 3.

2.3.3 *In vivo* investigation of the marker

The *in vivo* performance of the marker was evaluated in a mouse model by subcutaneous injection the ^{64}Cu-radiolabeled marker (0.01% PC) in the right flank of NMRI mice (injection volume: 50 µL, n = 8). Figure 2.9 shows the representative images of the marker in one representative mouse, and the marker was clearly visible on PET, CT and fluorescence images. An excellent positional stability of the marker was observed over 4 weeks, and the marker could be clearly identified for over 48 hours by PET images and 4 weeks by fluorescence images.

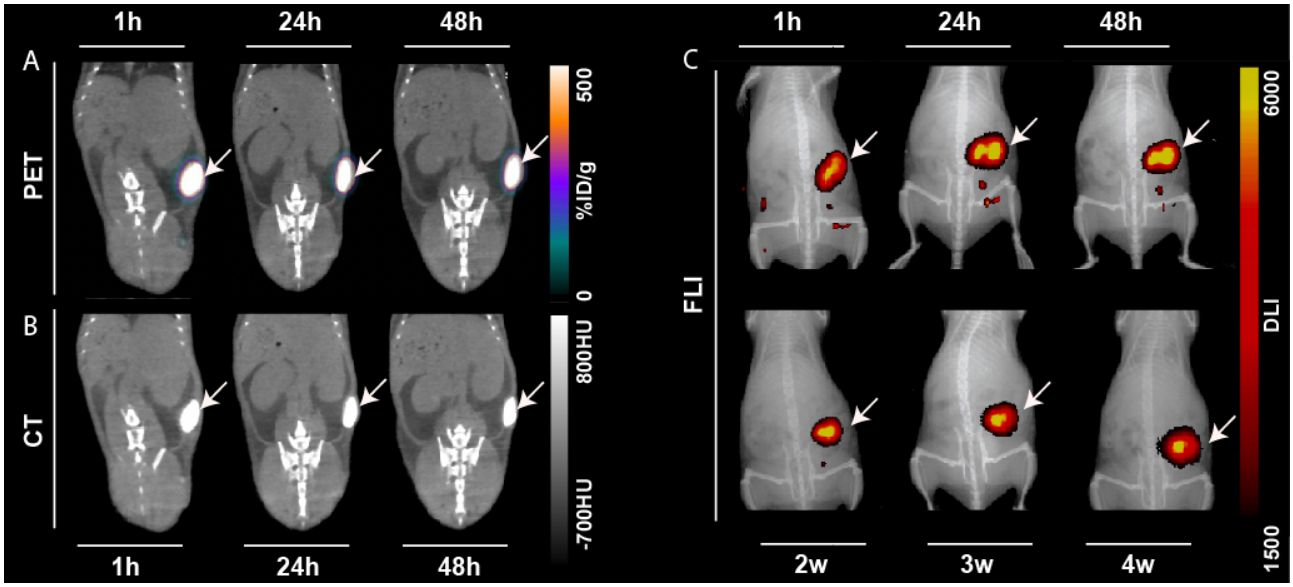

Figure 2.9. Representative images of one mouse with the fiducial marker as a function of time. Coronal PET images (A), CT images (B). From left to right: 1 hour, 24 hours and 48 hours post injection. Fluorescence images with excitation at 745 nm and fluorescence emission at 780 – 800 nm (C). Top row from left to right: 1 hour, 24 hours and 48 hours, low row from left to right: 2 weeks, 3 weeks and 4 weeks post injection. The white arrows indicate the injection position of the marker.

The *in vivo* stability of the marker, including volume and the change of CT contrast, was evaluated by ROI-analysis of the micro-CT, PET and fluorescence scan. The volume of marker was found to be stable (Figure 2.10A). A slight reduction of the volume (about 10%) was due to ethanol efflux, which was consistent with previous studies [40, 46]. Both PET (95 – 100% of the initial %ID) and fluorescence contrast (90 – 116% of the initial contrast) were stable during the experiment period without significant reduction.

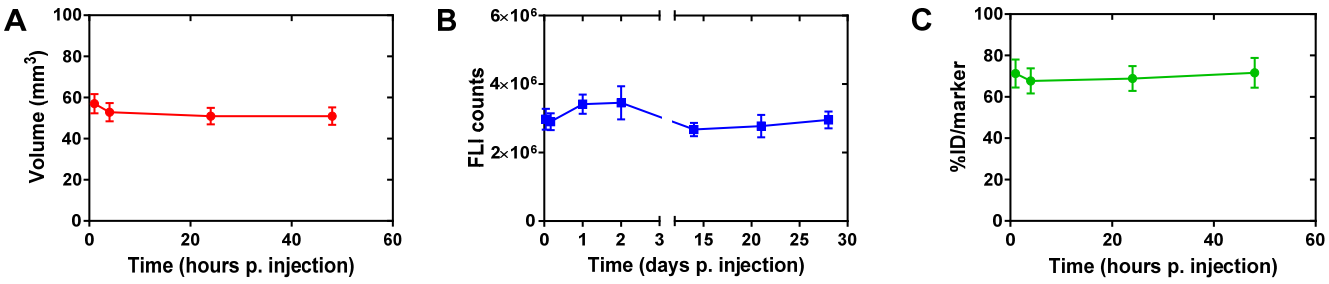

Figure 2.10. Marker volume based on CT contrast (A), fluorescence-lifetime imaging (FLI) counts (B) and activity dose per marker area (C) as a function of time. Results are presented as mean ± SEM, n = 8 in A and B, n = 3 in C.

The fluorescence contrast did not change in 4 weeks (Figure 2.10B), which indicate no leakage of PC from the marker and that PC has an excellent *in vivo* photostability. Currently, two FDA-approved fluorophores, methylene blue (MB) and indocyanine green (ICG) are widely used in NIR fluorescent guided processes such as surgery and lymph node mapping. Novel intraoperative real-time imaging systems, such as FLARETM [75] and SurgOptix [76], have been developed and are available for detecting MB (excitation/emission wavelength: 665/686 nm) and ICG (excitation/emission wavelength: 807/822 nm). ICG suffers from low photostability *in vivo* [154, 155, 156]. MB might not be suitable for surgical guidance due to the interference from the autofluorescence of the tissue in the similar emission range [123] and the toxicity of using MB is still a concern. PC could be a decent dye for our designed marker due to its high photostability and high emission wavelength. PC is well retained in the marker, and therefore the side-effect in other tissues is low. Moreover, the chelation of tetrapyrrolic macrocycle with a radionuclide such as $^{64}Cu^{2+}$ enables NIR imaging and gamma detection at the same time.

$^{64}Cu^{2+}$ was well retained in the marker by the chelation of PC, as the percentage of radioactivity in the marker area did not significantly change for 48 hours (Figure 2.10C). Note that the radioactivity level was around 70% of the injected activity, and the loss of 30% is likely to be due to the backflow of the marker solution through the injection path. In order to evaluate the leakage of the radioactivity from the marker and its potential risk to the healthy organs, the biodistribution of the ^{64}Cu was investigated. The whole-body distribution of ^{64}Cu in mice was monitored by PET/CT and quantified as percent injected dose per tissue gram (%ID/g) (Figure 2.11A). After 48 hours, 5 mice were euthanized and organs of interest were weighed and well-counted (Figure 2.11B). The result of biodistribution was consistent with that from the *in vitro* release study, and both studies clearly

showed a high ^{64}Cu retention in the marker with less than 1% radioactivity leakage. A slight increase in radioactivity concentration (682 ± 177 at 1h to 733 ± 154 %ID/g at 48h post injection) in the marker was observed over time, which is likely caused by the decrease in marker volume as a result of the ethanol efflux. The accumulation of radioactivity was low in all other tested organs. We observed the accumulation of activity in the liver (1 ± 0.3 %ID/g) and kidney (0.6 ± 0.1 %ID/g) to be significantly higher than spleen (0.2 ± 0.05 %ID/g) and blood (0.1 ± 0.01 %ID/g) ($p < 0.05$) from well counting results. It might be due to the release of free $^{64}Cu^{2+}$ that was not chelated by PC in the marker, since free $^{64}Cu^{2+}$ is known to accumulate in liver and kidney as reported previously [157]. The biodistribution results indicate that the marker lowers the risk of radiation to healthy organs as only little radioactivity is released from the marker to healthy tissues.

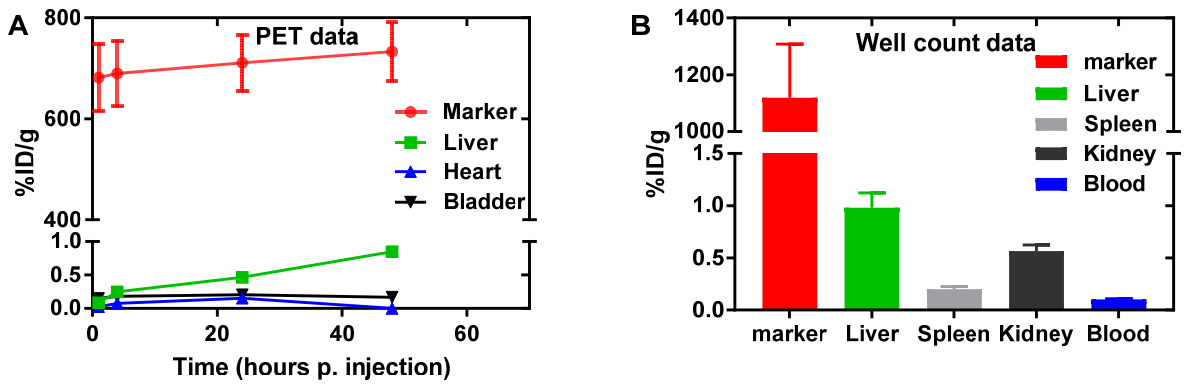

Figure 2.11. Biodistribution of ^{64}Cu in NMRI mice based on PET imaging and well counting. Biodisctribution of ^{64}Cu in marker, liver, heart and bladder based on PET as function of time post injection. (A). Biodistribution of ^{64}Cu 48h post injection based on organ well counting data (B). The results are presented as mean ± SEM, n = 5.

2.4 General discussion and future perspectives

PC is an excellent fluorophore for image guided surgery, due to its long-term photostability. However, the marker containing PC might not be fully compatible with current available intraoperative real-time imaging system for detection of ICG due to the slightly shorter emission wavelength of PC. The development of either new imaging systems that are suitable for the marker or other naphthalocyanine alternatives to PC with similar emission profiles as ICG or MB is highly relevant to the future clinical use of the marker.

Marker containing other potential dyes, 5,9,14,18,23,27,32,36-octabutoxy-2,3-naphthalocyanine (PC1, excitation/emission wavelength: 750/832 nm) and 2,9,16,23-tetra-tert-butyl-29*H*,31*H*-phthalocyanine (PC3, excitation/emission wavelength: 650/722 nm), were preliminarily evaluated in the marker as well. The chemical structure of these dyes is presents in Scheme 2.2. PC1 was found to fluoresce in the 700-800 nm range and absorb light from 600-700 nm in the marker formulation (Figure 2.12A). PC3 fluoresced in the range 850-1100 nm and absorbed light in the 700-900 nm range in marker formulation (Figure 2.12B). Note that PC3 is more hydrophobic than PC and PC1, in order to increase the compatibility of PC3 in the marker solution, the organic solvent in the marker was changed to benzyl alcohol. The fluorescence spectra indicated the markers contain these two dyes might be detected by the current available imaging systems for ICG and MB, respectively. Moreover, like PC, both two dyes have the ability to form complex with $^{64}Cu^{2+}$ because of the tetrapyrrolic macrocycle.

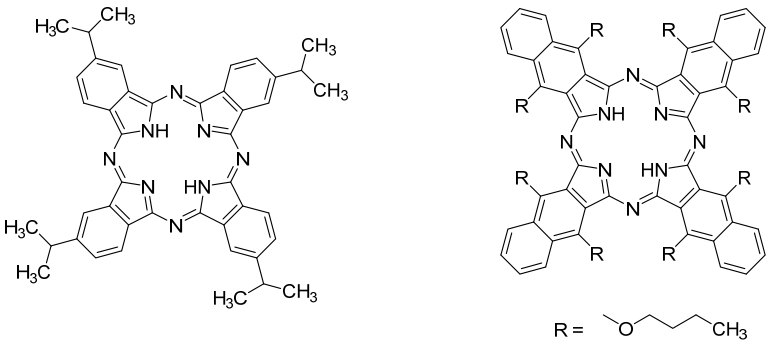

Scheme 2.2. Chemical structures of 5,9,14,18,23,27,32,36-octabutoxy-2,3-naphthalocyanine (PC1, left) and 2,9,16,23-tetra-tert-butyl-29*H*,31*H*-phthalocyanine (PC3, right).

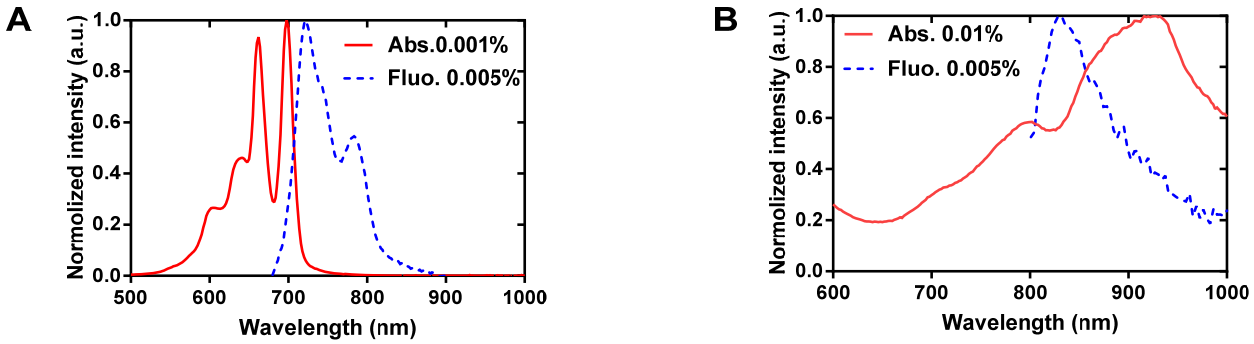

Figure 2.12. Absorbance and fluorescence spectra of PC1 and PC3 dissolved in marker formulations. PC1 dissolved in in SAIB:xSAIB:EtOH 70:10:20 marker formulation at excitation wavelength of 650 nm (A). PC3 dissolved in SAIB:BA 80:20 marker formulation at an excitation wavelength of 750 nm (B).

^{64}Cu is a PET radionuclide with a relatively low positron energy (E_{mean} = 278 keV, E_{max} = 653 keV), which can provide valuable preoperative information by PET/CT imaging. Moreover, intraoperative localization of the marker can be detected by a hand-held high-energy gamma probe, which was designed to detect the 511 keV photons resulting from the positron-electron annihilation [136, 158]. Currently, technetium-99m (^{99m}Tc), a gamma ray emitter with an average energy of 141 keV, is the most commonly used radionuclide for radioguided procedures. Nevertheless, the window of these procedures is very short due to the short half-life of ^{99m}Tc (6 hours). In this case, the procedures guided by ^{64}Cu can be prolonged up to 72 hours due to its considerable half-life of 12.7 hours. Other gamma emitters with low energy and long half-life, such as indium-111 (E_{mean} = 171 keV and 254 keV, $T_{1/2}$ = 2.8 days) and gallium-67 (E_{mean} = 93 keV, 184 keV, 300 keV and 393 keV, $T_{1/2}$ = 78 hours), are also possible to be chelated in the marker for intraoperative gamma detection, since the tetrapyrrolic macrocycle is able to chelate In^{3+} [154] and Ga^{3+} [159, 160]. These low-energy gamma emitters might also compatible with the current gamma cameras that are applying in clinical sentinel lymph node mapping, for real-time intraoperative SPECT image guided surgery.

Besides the application of the marker in image guided surgery, the marker would be promising for emission guided radiation therapy (EGRT), which integrates accurate tumor tracking and dose delivery [103, 104]. An EGRT system combining PET imaging setup and beamlet for radiotherapy has been recently designed by an American company, Reflexion [102]. During the procedure, coincident photon pairs produced by positron annihilation are continuously detected. Each photon pair is detected by a PET setup containing a ring of scintillation detectors from different planes simultaneously. Then, the EGRT system delivers beamlets of therapeutic radiation along the paths of the coincidence photon pairs. Therefore, the accurate tracking and radiation delivery can be substantially improved by EGRT [103]. The injectable marker developed in this study has the advantages to reduce patient discomfort comparing to conventional markers for radiation therapy and surgical guidance, such as 2-mm-diameter gold markers or ^{125}I radioactive metal seeds [161]. Currently, the marker for EGRT is intravenous injection of [^{18}F]2-fluoro-2deoxy-glocose (FDG) [103, 104]. The intratumoral implantation of the marker can provide a high tumor-to-background signal in comparison to FDG. Therefore, the use of marker for EGRT might be more effective.

Imaging plays a crucial role in oncologic surgery procedures. Many novel hybrid imaging probes combining different modalities have been described and intended to provide accurate localization of the tumor with high sensitivity and specificity in real-time surgery. In the background (section 2.1), two novel dual marker systems for imaging guided surgery were introduced. One is RGD peptide-

IRDye800-DTPA probe targeting to tumor related integrin and providing both NIR imaging and gamma detection during surgery [146]. The other one is a liposome formulation consisting ICG and iohexol for NIR and CT imaging [140]. Both marker systems could provide long contrast time to several days. However, these systemically circulative imaging probes might have the common disadvantage that the high signal in blood or other organs may interfere with target lesion visualization during surgery. Our intratumoral implanting marker has the great advantage of providing high contrast in the tumor with low background signal. Moreover, the long-term stability in both localization and contrast of the marker provide the flexibility of planning and scheduling to the surgeons.

2.5 Conclusion

In this study, we have successfully developed an injectable multimodal fiducial marker based on SAIB. The marker consisted of xSAIB as CT contrast and PC as both NIR fluorescence imaging and complexation of $^{64}Cu^{2+}$ (>99% RCP in 2 hours) for PET imaging and gamma detection. The marker combined the advantages of five different technologies by providing preoperative information by CT, ultrasound and PET images as well as accurate intraoperative location of the tumor by NIR images and gamma detection. The *in vivo* evaluation of the marker by subcutaneous injection into NMRI mice showed long-term stability of localization. The marker was clearly visible by PET and CT images for at least 48 hours with 1.75 MBq ^{64}Cu at the injection time, and NIR images for at least 4 weeks. Moreover, no observed change in the fluorescence intensity indicating that PC was well retained in the marker with excellent photostability. The biodistribution results based on PET images and well-counting showed limited accumulation of ^{64}Cu in healthy tissues because of the formation of ^{64}Cu-PC complex. According to the results presented in this study, the marker is promising for clinical use and can be expected to benefit both surgeons and patients.

2.6 Experimental section

2.6.1 Material

6,6'-di-triidobenzene-isobuturic-sucrose or IodoSAIB (X-SAIB) was kindly provided by the Danish company, Nanovi. The freeze dried, premixed stealth liposome mixture of hydrogenated soy

phosphatidylcholine (HSPC), cholesterol (CHOL) and 1,2-distearoyl-sn-glycero-3-phosphoethanolamine-N-[methoxy(polyethylene glycol)-2000] (DSPE- PEG2000) (565:382:53, molar ratio) was purchased from Lipoid. Sucrose acetate isobutyrate (SAIB), cupric chloride dehydrate ($CuCl_2 \cdot 2H_2O$), 2,11,20,29-Tetra-tert-butyl-2,3-naphthalocyanine (PC) and all other chemicals were purchased from Sigma Aldrich. All the chemicals and reagents were of analytical grade and used without further purification.

The UV-vis spectra of markers were recorded by a multimode microplate reader (Tecan). The fluorescence emission of markers with PC was measured by a fluorescence spectrometer (OLIS SLM8000 or OLIS DM 45) in quartz cuvettes (Helma). Surface fluorescence imaging was recorded by using an Odyssey FC imaging system (Licor).

All radioactivities were measured by a Veenstra Instruments dose calibrator VDC-505 (Comecer) or a liquid scintillation counting on a 300 SL spectrometer (HIDEX) with the energy range of 2 – 850 keV for ^{64}Cu. The scintillation vials and the scintillation cocktail were purchased from PerkinElmer. All radio-thin layer chromatography (radio-TLC) was performed on silica gel 60 F254 plates (Merck), using $CHCl_3$:MeOH:AcOH (98:1:1) as eluent. A MiniGita Star with a Beta Detector GMC probe (Perkin-Elmer) was used for analysis of radio-TLCs with radioactive peaks integrated using associated computer software.

Isotonic buffer, ISO-TRIS, containing 2-Amino-2-(hydroxymethyl)-1,3-propanediol (TRIS, 10 mM) and sodium chloride (150 mM), was prepared and adjusted to a final pH of 7.8, using hydrochloride acid (0.1 M). Phosphate-buffered saline was prepared by mixing sodium phosphate monobasic dihydrate and sodium phosphate dibasic dihydrate to obtain pH 7.4 (10 mM phosphate, 150 mM NaCl, pH 7.4).

Mini-extruder was purchased from Avanti Polar Lipids. The hydrodynamic size of liposomes were measured in ISO-TRIS by dynamic light scattering (DLS) on a Zetasizer (Malvern). Phosphor concentration of liposomes was measured by ICP-MS (Thermo Scientific, iCAP Q).

2.6.2 Preparation of marker formulations

All the percent and ratios represent weight percent or weight ratios unless otherwise noted. SAIB was heated to 70℃, and 7g of SAIB was poured into a glass vial. 1g xSAIB and 2g ethanol was mixed

with SAIB and sonicated for 30 minutes to obtain a transparent and homogeneous marker matrix (SAIB:xSAIB:ethanol 70:10:20).

1mg PC was weighted into a glass vial. 1g of marker matrix was added, and the resulting solution was sonicated at 55℃ for 6 hours and followed by magnetical stirring at 55℃ for 16 hours, to obtain a final dye concentration of 0.1%. Markers with different PC concentrations (0.05%, 0.01%, 0.006%, 0.003%, 0.001%, 0.0006%, 0.0003%, 0.0001% or 0.00001% w/w) were prepared by diluting 0.1% PC marker with marker matrix. The resulting markers were homogenized by 5 minutes magnetically stirring.

2.6.3 UV-vis spectra of markers

Markers with different PC concentrations (0.01%, 0.006%, 0.003%, 0.001%, 0.0006%, 0.0003%, 0.0001% or 0.00001%) were prepared as described above. Each marker (0.2 mL) was pipetted into a 96-well plate, and the UV-vis spectrum (400 – 1000 nm) was recorded by a multimode microplate reader with bandwidth of 3.5 nm.

2.6.4 Fluorescence emission

The fluorescence spectra of markers with different PC concentrations (0.1%, 0.05%, 0.01%, 0.006%, 0.003%, 0.001%, 0.0006%, 0.0003%, 0.0001% or 0.00001%) were measured using a fluorescence spectrometer (OLIS SLM8000). Briefly, each marker solution (1.2 mL) was transferred to a quartz cuvette and the fluorescence emission spectra was recorded in a wavelength range of 780 – 830 nm at an excitation wavelength of 768 nm, scan time of 45 seconds and a slit width of 8 mm. The full fluorescence spectra of the marker with PC (0.001% w/w) was measured using a fluorescence spectrometer (OLIS DM 45). Briefly, each marker solution (1.2 mL) was transferred to a quartz cuvette and the fluorescence emission spectra was recorded in a wavelength range of 780 – 830 nm at an excitation wavelength of 700 nm with an integration time of 0.2 seconds and a slit width of 26 mm. The full fluorescence spectra of the marker with PC1 and PC3 were also measured by a fluorescence spectrometer (OLIS DM 45). Details are described in section 2.8.12.

2.6.5 Surface fluorescence imaging and the influence of ethanol on fluorescence

Markers solutions containing different PC concentrations (70 µL, 0.01%, 0.006%, 0.003%, 0.001%, 0.0006%, 0.0003%, 0.0001% or 0.00001%) were spotted on a 10-well cover-glass. The surface fluorescence of markers was measured by an *in vitro* Licor NIR system (excitation wavelength at 785 nm, emission wavelength at 800 nm, and resolution of 125 µm). Then, the 10-well cover-glass with markers was stored in the vacuum oven at 55 ℃ overnight in order to remove ethanol from the markers. After the markers had cooled to room temperature, the surface fluorescence was measured again as described above.

2.6.6 Effect of copper on the fluorescence of markers

A solution of $CuCl_2 \cdot 2H_2O$ in ethanol (0.005 mg/mL) was prepared and transferred to glass vials (0, 43.6, 87.1, 130.7, 217.8 or 435.6 µL). The ethanol in each vial was evaporated by heating at 55℃ with nitrogen flow. Marker with PC (1.2 mL, 0.001%) was added into the vails containing different amount of $CuCl_2$ and the molar ratio of Cu^{2+} / PC in each vial was 0, 1:10, 1:5, 3:10, 1:2 and 1:1, respectively. The resulting mixtures were magnetically stirred at 55 ℃ for 2 hours. The absorbance was measured as described above in section 2.8.3. The fluorescence emission spectra of each mixture was obtained as described above in section 2.8.4.

2.6.7 Preparation of ^{64}Cu

^{64}Cu was produced on a PETtrace cyclotron (GE Healthcare) equipped with a beamline by proton irradiation of an electroplated ^{64}Ni target, then purified by anion exchange chromatography in aqueous hydrogen chloride (HCl) media. The ^{64}Cu was ultimately obtained in aqueous HCl (1.0 M), and isolated by evaporation of aqueous HCl by argon flow, as described before [9]. The dry $^{64}CuCl_2$ was used for radiolabeling markers.

2.6.8 Radiolabeling of markers

A marker solution containing PC (750 µL, 0.01% or 0.001%), or a marker without PC (750 µL) was added to $^{64}CuCl_2$ (150 MBq). The resulting mixtures were magnetically stirred at 55 ℃ for 2 hours.

A small amount of each radiolabeled marker solution was weighed into glass vial and dissolved in acetonitrile to a concentration of about 10 mg/mL. The resulting solution was analyzed by radio-TLC. The formation of ^{64}Cu-PC was confirmed by comparing the obtained TLC retention factor (R*f* = around 0.8) with that of a non-radioactive chemically identical reference compound. The R*f* of ^{64}Cu in marker without PC remained at the origin (R*f* = 0).

The reference non-radioactive complex was produced by adding a chloroform solution of PC (1mL, 1mg/mL) to 0.02 mg $CuCl_2 \cdot 2H_2O$ (molar ratio Cu^{2+}:PC 10:1). The resulting mixture was magnetically stirred at 55 ℃ for 2 hours. The resulting product and PC dye alone were analyzed by MALDI-TOF MS (Bruker Reflex, Bruker Daltonics, Billerica, MA, USA): Calc. M: 939.2 Da., Obs. M: 939.2 Da. (PC dye). Calc. M: 1000.7 Da., Obs. M: 1000.0 Da (Cu-PC complex). 1 µL of mixture was spotted on silica gel 60 F254 plates (Merck) and a solution of $CHCl_3$:MeOH:water:AcOH (70:25:4:1) was used as eluent. The R*f* of resulting Cu-PC complex was about 0.8.

2.6.9 *In vitro* release of ^{64}Cu from markers

A radiolabeled marker (initial radioactivity concentration 300 MBq/mL) containing PC (100 µL, 0.01% or 0.001% w/w) or marker matrix without PC (100 µL) was injected through a 25G needle into release medium (4.0 mL), which contained ISO-TRIS, EDTA (1.0 mM) and stealth liposomes (lipid concentration: 5.0 mM). Liposomes were produced by hydrating commercial stealth lipid mixture with ISO-TRIS (37.5 mg/mL) at 65 ℃ by sonication for 1 hour followed by sizing with a mini-extruder with a cut-off size of 200 nm. The size of liposomes was 142.4 ± 1.6 nm with a PDI of 0.19 ± 0.006. The phosphor concentration of liposomes was measured using ICP-MS with an internal standard (gallium, 10 ppb), and the liposomes were further diluted by ISO-TRIS to a final concentration of 5 mM. The radioactivity of each marker injected into the buffer was measured on a dose calibrator. The *transfer efficiency*, which is defined as the ratio of the measured radioactivity to the theoretical radioactivity of the marker that was injected in the buffer, was calculated for each formulation.

Aliquots (15 – 1000 µL) were removed as a function of time (1 hour, 3 hours, 6 hours, 1 day, 2 days, 4 days and 6 days), and replaced with an equal amount of release medium. After 6 days, all the release medium was removed and remaining marker was dissolved using ethanol (1.0 mL). An aliquot of the resulting solution (250 µL) was removed for quantification. All removed aliquots were analyzed by

liquid scintillation with the energy range of 2 – 850 keV. A calibration curve (20 – 800 Bq) was prepared for ^{64}Cu and was linear in the required concentration range ($r^2 > 0.999$).

2.6.10 *In vivo* experiments

^{64}Cu radiolabelled SAIB:xSAIB:EtOH:PC2 70:10:20 w/w marker with 0.01% w/w PC were prepared as described in section 2.8.8. At the time of injection, the markers had an activity of 35 MBq/ml.

Study setup: 8 mice (NMRI/Taconic) were subcutaneous injected with 50 µL (1.75 MBq) marker on right flank for IVIS-imaging of the fluorophore and PET-imaging of ^{64}Cu over time. All eight mice were PET/CT and IVIS scanned at 1h, 4h, 24h and 48h post injection, and three mice were IVIS scanned after 2 weeks, 3 weeks and 4 weeks. Five mice were euthanized after PET/CT scanning and organs were following collected and counted for 120 seconds on a Wizard Well counter.

PET-procedure: Mice were anaesthetized using sevoflurane, placed on heated bed for scan, and scanned with CT and subsequent PET data were acquired on a MicroPET Focus 120 (Siemens Medical Solutions, Malvern). The voxel size was 0.866 × 0.866 × 0.796 mm^3, and in the center field of view the resolution was 1.4 mm full width at half-maximum (fwhm). PET-protocol for ^{64}Cu with emission time of 5 min for time points 1h and 4h, and 10 min for 24h, and furthermore 20 min for 48h scan. Data were reconstructed with the maximum a posterior (MAP) reconstruction algorithm. For anatomical localization of activity, CT images were acquired with a dediactes small animal imaging system (NanoScan microSPECT/CT, Mediso). After data reconstruction, PET and CT images were fused using the Inveon Software (Siemens). The emission scans were corrected for random counts and dead time. The PET and CT images were used to identify regions of tracer uptake and to generate regions of interest (ROIs) that were applied to each scan separately. A region of interest was drawn around the gel and liver and kidney, and either %ID/gel or %ID/g was calculated.

IVIS-procedure: Mice were anaesthetized using isoflurane, placed on heated plate for scan, and fluorescence (FLI) scanned. A binning of 2, exposure time of maximum 120 seconds and excitation and emission wavelength of Ex: 745 nm and Em: 810-875nm were employed.

Well counting: After last PET scan time (48h), five mice were euthanized and organs collected for well count. The well counting protocol consisted of 120 seconds counting per organ sample, and the results were presented as average ± SEM.

Marker volume: The marker volume was obtained by automated segmentation procedure based on a CT contrast cut-off of 250 HU.

2.6.11 Statistics

The statistics were calculated by one-way ANOVA with Tukey's multiple comparison test. The probability values that are less than 0.005 (p<0.005) are considered as a statistical significant difference.

2.6.12 Supplementary information – primary test of the marker with other dyes

SAIB was heated to 70℃, and 7g of SAIB was poured into a glass vial. 1g xSAIB and 2g ethanol was mixed with SAIB and sonicated for 30 minutes to obtain a transparent and homogeneous SAIB:xSAIB:ethanol formulation (SAIB:xSAIB:ethanol 70:10:20). 8g of SAIB was poured into a glass vial. 2g of benzyl alcohol (BA) was mixed with SAIB and sonicated for 30 minutes to obtain a transparent and homogeneous SAIB:BA formulation (SAIB:BA 80:20).

A solution of PC1 dissolved in chloroform (50 µL, 1 mg/mL) was pipetted into a glass vial, and the chloroform was evaporated at room temperature under nitrogen flow. Subsequently, 1g of marker formulation (SAIB:xSAIB:ethanol 70:10:20) was added into the vial to achieve a PC1 concentration of 0.005% w/w for fluorescence emission measurement. The resulting mixture was sonicated at 70℃ for 15 minutes and followed by vortexing. The marker was further diluted using marker solution to a PC1 concentration of 0.001% for absorbance measurement.

A solution of PC3 dissolved in chloroform (100 µL, 1 mg/mL) was pipetted into a glass vial, and the chloroform was evaporated at room temperature under nitrogen flow. Subsequently, 1g marker formulation (SAIB:BA 80:20) was added into the vial to achieve a PC3 concentration of 0.01% for absorbance measurement. The resulting mixture was sonicated at 70℃ for 15 minutes and following by vortexing. The marker was further diluted using marker solution to a PC2 concentration of 0.005% for fluorescence emission measurement.

Each marker solution (0.2 mL) was pipetted into a 96-well plate, and the UV-vis spectrum (400 – 1000 nm) was recorded by a multimode microplate reader (Spark®, Tecan) with bandwidth of 3.5 nm.

Each marker formulation (1.0 mL) was transferred to a quartz cuvette (Helma, 10mm light path), and the fluorescence spectrum was collected by a fluorescence spectrometer (OLIS DM 45) with excitation/emission bandwidth of 26 nm and integration time of 0.2 seconds. An excitation wavelength of 650 nm was used for the marker formulation with PC1. An excitation wavelength of 750 nm was utilized for PC3 in the marker formulation.

Chapter 3. Preclinical Evaluation of Cationic DOTA-triarginine-lipid Conjugates for Controlled Intratumoral Distribution of Radionuclides in Brachytherapy

3.1 Background

Brachytherapy (BT) is a form of internal radiotherapy that has been adopted as an efficient way to treat certain cancers since the 1950 [114]. In BT, sealed radioactive sources are placed in or near the tumor in order to deliver a local radiation dose with minimal systemic exposure. The emitted ionizing radiation results in DNA damage and locoregional cell death. In clinical applications, BT is used to treat solid tumors, particularly gynecologic and prostate cancer [32, 162].

As mentioned in the introduction (Section 1.4.2), BT exists in two forms, high-dose rate brachytherapy (HDR-BT) and low-dose rate brachytherapy (LDR-BT). In HDR-BT, catheters containing radionuclides such as iridium-192 (380 KeV) and cobalt-60 (1.25 MeV), are temporarily placed in or close to the tumor with dose rates of >12 Gy/h [13, 107]. In contrast, radioactive sources are permanently implanted in LDR-BT. This also delivers a high total radiation dose but at a lower dose rate (0.4-2 Gy/h). Commonly used radionuclides in LDR-BT are palladum-103 and iodine-125, both of which emit photons with energies in the 20-35 keV range. Both forms of BT have the advantage of high radiation dose to the tumor with minimal exposure to healthy tissues. However, BT remains an invasive technique that requires insertion of radioactive sources under anesthesia, and the non-biocompatible sources may cause serious inflammation and discomfort to patients [115], [116]. Moreover, the use of point-sources in BT results in a heterogeneous distribution of the radiation dose in tumor.

To address these shortcomings of BT, the development of materials that are biodegradable, biocompatible and easy to administer is highly relevant in brachytherapy. Improving on the intratumoral distribution of the radiation dose with long-term tumor retention can be considered as major points of improvement when designing new materials for BT. Small molecules can diffuse through the tumor interstitium, resulting in a uniform intratumoral distribution. Intratumoral injection of radiolabeled small molecules such as ^{186}Re-perrhenate and ^{186}Re-N,N-bis[2-mercaptoethyl]-N=,N=-diethyl-ethylenediamine (BMEDA) were studied previously and the intratumoral retention of these compound was found to be very short (less than 2% intratumoral retention of injected

radioactivity after 2 hours for both compounds) [119]. Biomaterials have the potential to improve the intratumoral retention of such compounds. However, only a few new biomaterials intended to provide both better distribution and retention of the injected radioactive material have been described in recent years. The distribution of ^{103}Pd radiolabeled gold-coated nanoparticles was found to be more uniform than conventional metal seeds within the tumor [121]. Liposomes radiolabeled with ^{186}Re/^{188}Re were likewise demonstrated as a potential approach in brachytherapy [26]. These showed an ability to diffuse throughout the tumor and had higher intratumoral retention than small molecules. However, the distribution of both nanoparticle types was still relatively heterogeneous, making it problematic to correlate therapeutic efficacy with the injected dose.

3.2 Objective

We aimed to develop a new radiolabeled drug delivery system for intratumoral injection and controlled distribution of radioactive material throughout the tumor mass. To achieve this, we designed and synthesized two novel chelator-triarginine-lipid constructs (Scheme 3.1). Both compounds were based on the chelator 1,4,7,10-Tetraazacyclododecane-1,4,7,10-tetraacetic acid (DOTA), which is known for high stability chelation of a range of medically relevant radionuclides, such as ^{64}Cu, ^{177}Lu, ^{225}Ac, ^{68}Ga, etc. [163, 164, 165]. Moreover, the compounds were functionalized with hydrophobic acyl chains (16C or 18C) as well as strongly cationic triarginine groups (arginine sidechain pka: 12.5).

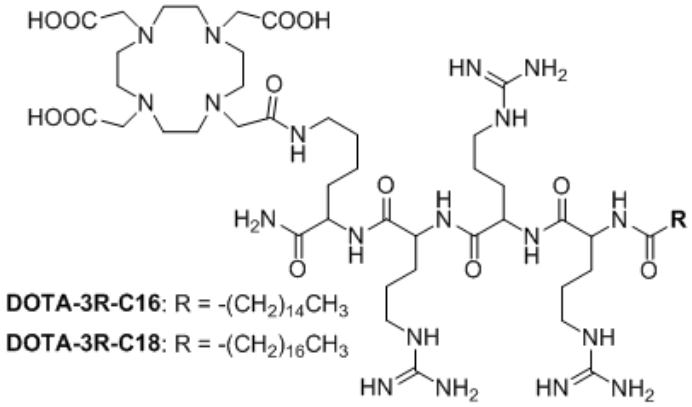

Scheme 3.1. Chemical structures of D3R-C16 and D3R-C18.

As surfactants, the two compounds were expected to partition into liposomal and cell membranes. The triarginine groups were chosen to enhance charge-based interaction with typically slightly negatively charged cancer cell membranes [166] (Figure 3.1). The critical micelle concentration (CMC) and partitioning of the D3R-C16/D3R-C18 into liposomes were characterized *in vitro*. Accurate and whole body biodistribution knowledge of radiolabeled designed formulations can be achieved by a positron emission tomography (PET) imaging. Copper-64 (^{64}Cu) is a useful PET radionuclide to image the biodistribution of drug delivery systems because of its low positron energy (Eav = 278 keV, Emax = 653 keV) and its considerable half-life of 12.7 hours, which allows imaging for up to 72 hours [8]. Therefore, the chelator-triarginine-lipid constructs were radiolabeled with ^{64}Cu and administered intratumorally in a murine model, both as the free compound and inseted into liposomes. The intratumoral distribution was evaluated by PET in combination with computed tomography (CT).

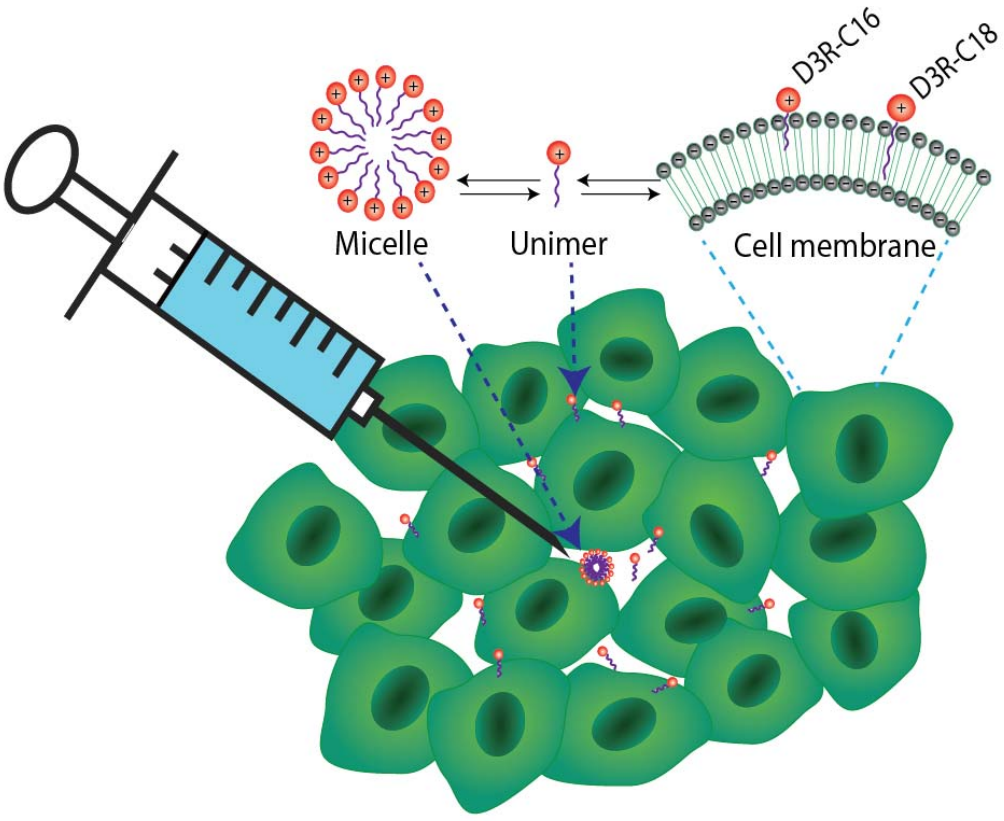

Figure 3.1. Schematic illustration of the interaction of cationic micelles with tumor cells and the surfactant equilibrium in the presence of a lipid membrane.

3.3 Results

3.3.1 Synthesis of non-radioactive Cu-D3R-C16 and Cu-D3R-C18 and cytotoxicity evaluation

In order to confirm the identity of ^{64}Cu-D3R-C16 and ^{64}Cu-D3R-C18, non-radioactive reference compounds, Cu-D3R-C16 and Cu-D3R-C18, were prepared by the method analogous to the radiolabeling itself. Analysis by TLC gave R*f* values 0.3-0.4 for Cu-D3R-C16 and 0.4-0.5 for Cu-D3R-C18. D3R-C16 and D3R-C18 have similar R*f* of 0.6-0.7.

The radiolabeling of both compounds gave 99% radiochemical purity (RCP) within 30 minutes. The radioactive products had the same R*f* values as the non-radioactive reference compounds, demonstrating the formation of ^{64}Cu-D3R-C16 and ^{64}Cu-D3R-C18. Free ^{64}Cu stayed at the origin in TLC. To evaluate the stability and specificity of the radiolabeling, free DOTA or EDTA was added as challenge to both products in a molar ratio of 10:1 with DOTA or EDTA in excess. There was no detectable formation of ^{64}Cu-DOTA (Rf = 0.3-0.4) or ^{64}Cu-EDTA (Rf = 0.7-0.8) in both samples after 24 hours at room temperature, demonstrating that ^{64}Cu was specifically chelated as the desired products.

As intratumorally administered D3R-C16 and D3R-C18 may migrate to surrounding healthy tissue, the toxicity of the compounds was investigated. The cytotoxicity of D3R-C16 and D3R-C18, as well as of non-radioactive Cu-D3R-C16 and Cu-D3R-C18, were measured towards CT26 cells (Figure 3.2). The half maximal inhibitory concentration (IC_{50}) of both D3R-C16 and D3R-C18 was found to be above 100 μM. Both compounds were slightly more toxic than their corresponding chelates with Cu^{2+}, having IC_{50} values about 80 μM. In the animal study, a concentration of 100 μM D3R-C18 was injected intratumorally, as a dispersion of the free compound or formulated with liposomes (injection volumes: 50 μL). The tumor volumes were 426.6 ± 168.0 mm^3 (n = 5) and 524.9 ± 81.6 mm^3 (n = 4) at the time of injection, respectively, based on CT. Accordingly, the average concentration of D3R-C18 in the tumor could be estimated to be about 10 μM, assuming homogenous intratumoral distribution of the compound. This indicated that D3R-C18 was likely to have negligible local cytotoxicity towards the cancer cells. Furthermore, the probability of D3R-C18 accumulating at levels higher than the IC_{50} in healthy tissues could also be considered unlikely.

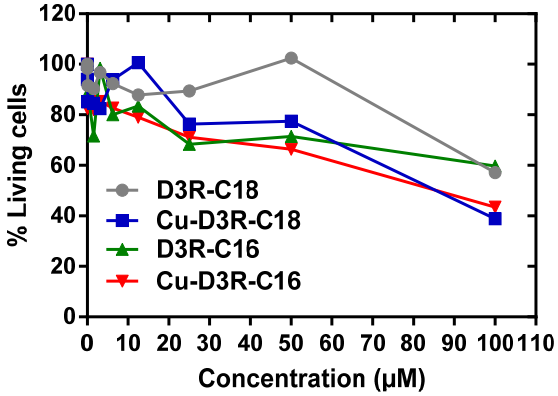

Figure 3.2. Cytotoxicity of D3R-C16/18 and their constructs with Cu^{2+} towards CT26 cells, n = 1. CT26 cells (4000 cells/well the day before the start of experiment) were incubated for 72 h with increasing concentration of D3R-C16/18 or their constructs with Cu^{2+}. Cell viability was evaluated using MTS assay.

3.3.2 Physical chemical characterization of surfactants

D3R-C16 and D3R-C18 were designed as surfactants, due to their spatially separated hydrophobic alkyl chains and charged polar head groups. Surfactants exist in different forms with the presence of lipid (Figure 3.1), which has been mentioned in section 1.2.2 Chapter 1. Surfactants are presented as mixture of micelles and free unimers in aqueous solution when the concentration of surfactants exceeds a certain threshold, which is defined as critical micelle concentration (CMC). The micelles will dissociate into single surfactant unimers when the solution is diluted below CMC. With the presence of membranes, the unimers have the ability to partition into double-layer lipid membranes [167, 168].

In order to predict the *in vivo* performance of D3R-C18 and D3R-C16, the CMC and the partitioning into liposomes were investigated. The change in surface tension of the medium as a function of the concentration of D3R-C16/D3R-C18 in ISO-HEPES-NaCl or ISO-HEPES-Sucrose was measured (Figure 3.3). The surface tensions decreased with the increasing accumulation of surfactant on the surface until they reached a plateau level. The CMC of both compounds was lower in ISO-HEPES-NaCl (D3R-C16: about 35 µM, D3R-C18: about 10 µM) than in ISO-HEPES-Sucrose, in which it was above 100 µM for both compounds. This can be attributed to electrolytes in the ISO-HEPES-NaCl screening the electrostatic charge repulsion between the ionized polar heads of the compound, causing micelles to form at lower surfactant concentrations. D3R-C18 exhibited a generally lower CMC than D3R-C16, likely due to the longer hydrophobic alkyl chain [169]. The zeta potential of micelles containing D3R-C18 in ISO-HEPES-Sucrose was 20.7 ± 0.5 mV.

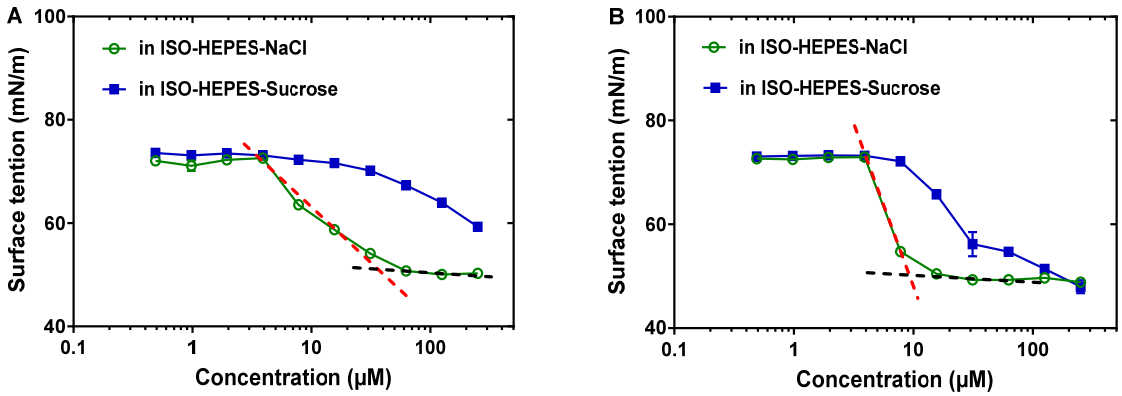

Figure 3.3. Surface tension plotted against the concentration of D3R-C16 (A) and D3R-C18 (B). The results are presented as mean ± SEM, n = 3. The surface tension is linearly dependent on the logarithm of the surfactant concentration in a range. Above CMC, the surface tension is independent of the surfactant concentration. The CMC is the intersection between the regression straight line (red dashed lines) of the linearly dependent region and the straight line passing through the plateau (black dashed lines).

D3R-C16 and D3R-C18 were radiolabeled with ^{64}Cu for membrane partitioning studies. Radiolabeled compounds were used because of their ease of quantification by a dose calibrator. Liposomes were utilized as a prominent and widely used model for cell membranes [170]. The kinetics of the partitioning were initially assessed in order to elucidate the incubation time needed for reaching partitioning equilibrium. ^{64}Cu-D3R-C16 was incubated at 37 ℃ with POPC liposomes at a relatively low lipid concentration of 0.36 mM. The partitioning equilibrium was reached within 10-30 minutes (Figure 3.4). Consequently, the total incubation time in subsequent studies was set to 60 minutes to ensure equilibrium.

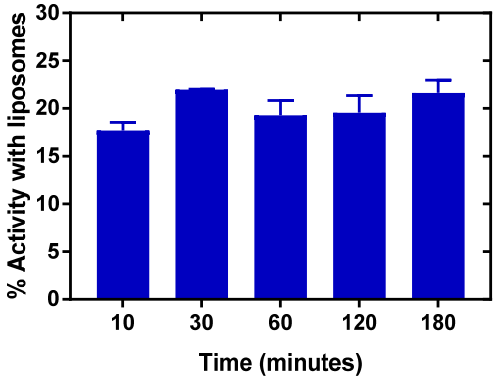

Figure 3.4. Partitioning kinetics of ^{64}Cu-D3R-C16 into POPC liposomes (lipid concentration: 0.36 mM) as a function of time. The results are given as mean ± SEM, n = 3.

The partitioning into the lipid membrane of both radiolabeled compounds increased with the liposome concentration regardless of liposome composition (Figure 3.5 A+B). At low lipid concentrations (0.36 mM), the lipid composition of the liposomes had no significant effect on the partitioning of ^{64}Cu-D3R-C16 (POPC: 24 ± 2%, POPC+POPG: 27.2 ± 0.7%, Stealth: 28 ± 5%). However, at lipid concentrations of 0.72 mM and 3.6 mM, the partitioning ratio of ^{64}Cu-D3R-C16 into stealth liposomes (0.72 mM: 53 ± 8% and 3.6 mM: 91 ± 3%) and POPC+POPG liposomes (0.72 mM: 55 ± 1%, 3.6 mM: 89.5 ± 0.9%) was significantly higher than into POPC liposomes (0.36 mM: 29.6 ± 0.2%, 0.72 mM: 57 ± 2%). At lipid concentrations of 0.36 and 0.72 mM, the partitioning of ^{64}Cu-D3R-C18 into POPC+POPG liposomes (0.36 mM: 74 ± 2%, 0.72 mM: 83 ± 2%) was higher than the partitioning into stealth liposomes (0.36 mM: 57 ± 2%, 0.72 mM: 78 ± 1%), and even higher than the partitioning into POPC liposomes (0.36 mM: 30.5 ± 0.5%, 0.72 mM: 57 ± 1%). However, no significant difference between ^{64}Cu-D3R-C18 partitioning into POPC+POPG liposomes (92.1 ± 0.7%) and stealth liposomes (93 ± 3%) was observed at a lipid concentration of 3.6 mM. Furthermore, partitioning of ^{64}Cu-D3R-C18 into POPC (81.2 ± 0.8%) was significantly lower than the other two liposome types at 3.6 mM lipid concentration.

The cause of the lower partitioning of both radiolabeled D3R-alkyl compounds into POPC liposomes may be attributed to the relatively neutral surface charge of these liposomes (-2.3 ± 0.6 mV). This could result in less affinity for the positively charged tri-arginine groups than in the case of the highly negatively charged surface of POPC+POPG liposomes (-49.1 ± 0.6 mV). In contrast, the partitioning of both ^{64}Cu-D3R-C16 and ^{64}Cu-D3R-C18 into stealth liposomes, also of limited zeta potential (-2.7 ± 0.3 mV), was high. This may be a consequence of negatively charged DSPE-PEG head groups on the surface of these liposomes. The reason for the low zeta potential of stealth liposomes is masking of the charges by the PEG corona [171], [172]. On this basis, the ^{64}Cu-D3R-C16 and ^{64}Cu-D3R-C18 appear to have a high affinity towards lipid membranes, with the tri-arginine group potentially enhancing the interaction with overall negatively charged lipid head groups on the surface. In comparison with ^{64}Cu-D3R-C16, ^{64}Cu-D3R-C18 showed higher partitioning into liposomes regardless of lipid composition and concentration, likely due to the larger C18-moiety.

The partitioning of D3R-C16 and D3R-C18 labeled with two different radionuclides, ^{177}Lu and ^{64}Cu, was compared (Figure 3.5 C+D). There was no significant difference ($p > 0.05$) observed in the partitioning of D3R-C16 due to changing the radionuclides. However, the partitioning of ^{177}Lu-D3R-C18 into lipid membranes was significantly higher than ^{64}Cu-DOTA-3R-C18 at low lipid

concentrations (0.36 and 0.72 mM). The reason for this difference may be attributed to the trivalent $^{177}Lu^{3+}$ forming a non-charged complex with DOTA, when one carboxylic acid on DOTA is used for conjugation. In contrast, divalent $^{64}Cu^{2+}$ forms a negative complex with DOTA. Therefore, the ^{177}Lu-DOTA moiety may have a higher affinity for negatively charged liposomal surfaces as compared to the ^{64}Cu-DOTA moiety. These results suggest that the valence of the radionuclide in use should be taken into consideration when predicting the intratumoral behavior of the DOTA-alkyl compounds.

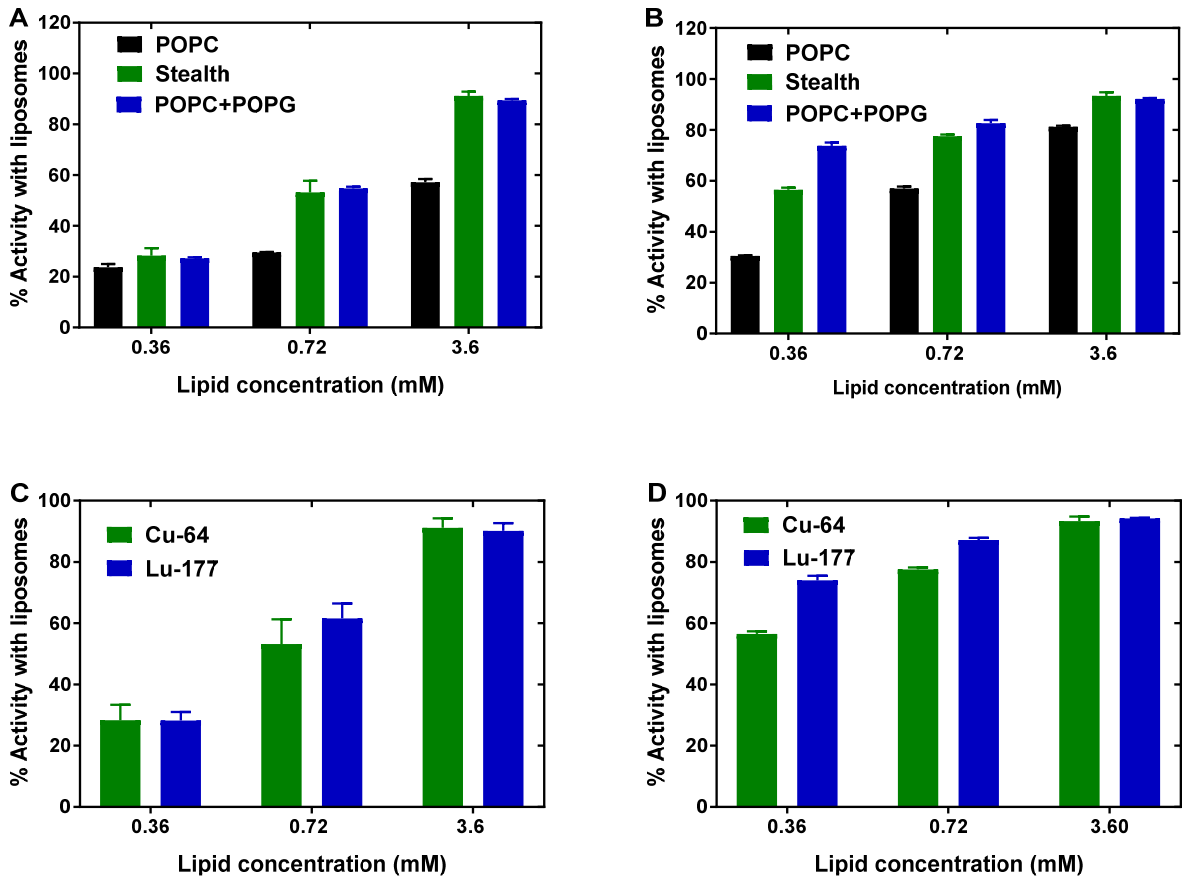

Figure 3.5. Partitioning into liposomes of ^{64}Cu-D3R-C16 (A) and ^{64}Cu- D3R-C18 (B). Comparison of liposome partitioning of D3R-C16 (C) and D3R-C18 (D) labeled with $^{64}Cu^{2+}$ or $^{177}Lu^{3+}$. The results are presented as mean ± SEM, n = 3.

3.3.3 Interaction between ^{64}Cu-D3R-C16/^{64}Cu-D3R-C18 and stealth liposomes

Liposomes have been recognized as promising vehicles for the intratumoral delivery of radionuclides, such as ^{186}Re, ^{188}Re and ^{99m}Tc [26, 118]. This is mainly due to their longer intratumoral retention and more uniform intratumoral distribution, as compared to small molecules where rapid washout from the injection site is typically seen. Since ^{64}Cu-D3R-C16/^{64}Cu-D3R-C18 were observed to efficiently

partition into stealth liposomes, we investigated these as potential vehicles for delivering the radioactive compounds. Surfactants mixed with liposomes will initially insert into the outer membrane leaflet, with the polar head-group facing the outer medium. From there, individual surfactants may potentially change location into the inter leaflet, with the head-group facing the liposomal compartment. This process is known as flip-flop [173]. Since this exchange may influence release kinetics of ^{64}Cu-D3R-C16/^{64}Cu-D3R-C18 from the liposomes, their tendency to flip-flop was investigated.

Two different methods for inserting the radioactive surfactants into liposomes were compared: 1) partitioning of ^{64}Cu-D3R-C16 or ^{64}Cu-D3R-C18 into preformed liposomes, analogous to the partitioning study described above, and 2) directly mixing ^{64}Cu-D3R-C16 or ^{64}Cu-D3R-C18 with lipid mixture, from which the liposomes were formed. The insertion efficiencies were 89% and 98% for ^{64}Cu-D3R-C16 and ^{64}Cu-D3R-C18, respectively by partitioning, and 87% and 92% for ^{64}Cu-D3R-C16 and ^{64}Cu-D3R-C18, respectively by direct mixing method. Partitioning would initially insert the surfactants exclusively in the outer leaflet, while direct mixing would give liposomes with surfactant present in both leaflets.

Liposomes prepared by both partitioning and direct mixing were diluted 1000x or 10000x in ISO-HEPES-NaCl and the radioactivity still associated with the liposomes after 2 h and 24 h incubation at 37 ^{o}C was measured (Table 3.1). After significant dilution, it was hypothesized the surfactant present in the outer leaflet would leave the liposomes to form separate micelles in the bulk medium. If the compounds could flip-flop, surfactant in the inner leaflet would also leave the liposomes, whereas it would be trapped in the liposomes if flip-flop was not possible. The amount of ^{64}Cu-D3R-C16 associated with the liposomes after 2 hours incubation was significantly lower for the partitioning type, than for direct mixing, both for 1000x and 10000x dilution. For ^{64}Cu-D3R-C18, there was no significant difference in radioactivity associated with the liposomes by both methods at 1000x dilution. However, the radioactivity associated with the liposomes prepared by partitioning was significantly lower than for direct mixing after 24 hours at 10000x dilution. Accordingly, these results indicate that a tendency to flip-flop is not pronounced for the two surfactants. This was underscored by the observation that less radioactivity was associated with the liposomes prepared by partioning after dilution for both surfactants. However, for ^{64}Cu-D3R-C16 loaded liposomes prepared by direct mixing, radioactivity levels with the liposomes were also relatively low (31% at 2 h and 25% at 24 h) at 10000x dilution, indicating that slow flip-flop and consequent de-loading of the radioactive surfactant may be occurring for this compound.

Table 3.1. The percent activity in the liposome fraction of each diluted sample. The radioactivity of liposome fraction was measured and divided by the totally activity of liposome and free compound fractions. Results are presented as mean ± SEM (n = 3).

Samples	% activity with liposomes				
	Before dilution n = 1	2h incubation 1000x dilution	24h incubation 1000x dilution	2h incubation 10000x dilution	24h incubation 10000x dilution
Partitioning ^{64}Cu-D3R-C16	89	23 ± 4	11 ± 1	8 ± 3	11 ± 4
Partitioning ^{64}Cu-D3R-C18	98	43 ± 4	47 ± 9	45 ± 10	16 ± 3
Direct mixing ^{64}Cu-D3R-C16	87	46 ± 4	56 ± 7	31 ± 7	25 ± 3
Direct mixing ^{64}Cu-D3R-C18	92	60 ± 8	50 ± 8	50 ± 7	47 ± 10

3.3.4 *In vivo* evaluation of radiolabeled samples

Because of the higher partitioning into liposomes, ^{64}Cu-D3R-C18 was selected for *in vivo* evaluation. The high partitioning into liposomes indicated a high affinity towards cancer cell membranes, which was expected to result in a desired longer intratumoral retention of the compound. ^{64}Cu-D3R-C18 was administered intratumorally both as the free compound and formulated with liposomes by partitioning method (LIP). Free $^{64}CuCl_2$ and free ^{64}Cu-DOTA were intratumorally administered as controls. According to the CMC of DOTA-3R-C18 of about 10 μM in ISO-HEPES-NaCl, the injected ^{64}Cu-D3R-C18 (100 μM) was primarily composed of cationic micelles. Stealth liposomes with ^{64}Cu-D3R-C18 (LIP) were also evaluated *in vivo*. The insertion of ^{64}Cu-D3R-C18 into the stealth liposomes occurred within 60 minutes with a quantitative loading efficiency of >98% at lipid concentration of 10 mM.

The whole-body biodistribution of the four radiolabeled preparations was monitored by PET/CT (Figure 3.6) and quantified as percent injected dose per gram tissue (%ID/g) (Figure 3.7). The *ex vivo* biodistributions were also determined by organ well counting (Figure 3.8). Figure 3.7A shows the tumor retention of the four preparations. Note that the initially increasing dose in the tumors is due to slow (30 seconds) initial intratumoral administration. ^{64}Cu-DOTA was cleared very rapidly after injection from both the tumor and the body as a whole through kidneys and bladder (Figure 3.7C and 3.7F), which is in line with previous reports [174, 175]. At 12 minutes post injection, 90 ± 15 %ID/g ^{64}Cu-DOTA was present in the tumor, which was the lowest among all the formulations. Only 4 ±

2 %ID/g and 2.3 ± 0.9 %ID/g was found in the tumor at 6 hours and 24 hours respectively, underscoring the rapid wash-out. Free $^{64}CuCl_2$ is known to accumulate in solid tumors since copper is an essential element in mammals [157, 176]. We observed the initial tumor retention of free ^{64}Cu to be high (140 ± 62% at 12 minutes). Then, ^{64}Cu was quickly cleared with tumor retention of 18 ± 3% and 10 ± 1% at 6 hours and 24 hours, respectively. As reported previously, most of the released free $^{64}CuCl_2$ accumulated in liver and kidney [157] and as were also observed in this study. The retention of free ^{64}Cu-D3R-C18 was the highest (232 ± 77%) in the first 12 minutes among the four preparations. However, the difference was not significant in comparison with free $^{64}CuCl_2$ and LIP. A significant difference was only found between the intratumoral retention of ^{64}Cu-D3R-C18 and ^{64}Cu-DOTA ($p = 0.03$). The data however, clearly indicated that the tumor retention was highest for ^{64}Cu-D3R-C18. Unlike ^{64}Cu-DOTA that had insignificant accumulation in healthy tissues, free ^{64}Cu-D3R-C18 accumulated gradually in liver, blood, spleen and kidney. The tumor retention of ^{64}Cu-D3R-C18 was significantly higher than the two control groups at 6 hours (48 ± 19%) and 24 hours (22 ± 8%) ($p < 0.05$). The initial tumor retention of LIP was moderate at 12 minutes (148 ± 38%). As free ^{64}Cu-D3R-C18 released from liposomes after the injection of the liposomal preparation, the clearance of radioactivity could be both in the form of free ^{64}Cu-D3R-C18 and LIP. A significant initial clearance of liposomes from the tumor was also observed in previous studies [26, 177]. Afterwards, the retention of LIP in the tumor was relatively stable at a level of 68 ± 26% at 6 hours and 53 ± 16% at 24 hours, which is significantly higher than the other three formulations. The cleared dose was primarily observed to accumulate in spleen and liver with a gradually increasing dose up to >5% ID/g from 6 hours onwards, which is consistent with previous study of ^{99m}Tc-labeled liposomes by intratumoral injection [177]. The cause for the long tumor retention time of LIP might be attributed to a combination of (1) slow clearance from the interstitial space because of the large liposomes particle size [26], and (2) slow release of ^{64}Cu-D3R-C18 from the liposomes when liposomes were diluted after injection (Table 3.1). The *ex vivo* data for the accumulation in organs for each group (Figure 3.8) shows the similar trend in comparison with those from PET imaging at 24 hours (Figure 3.7).

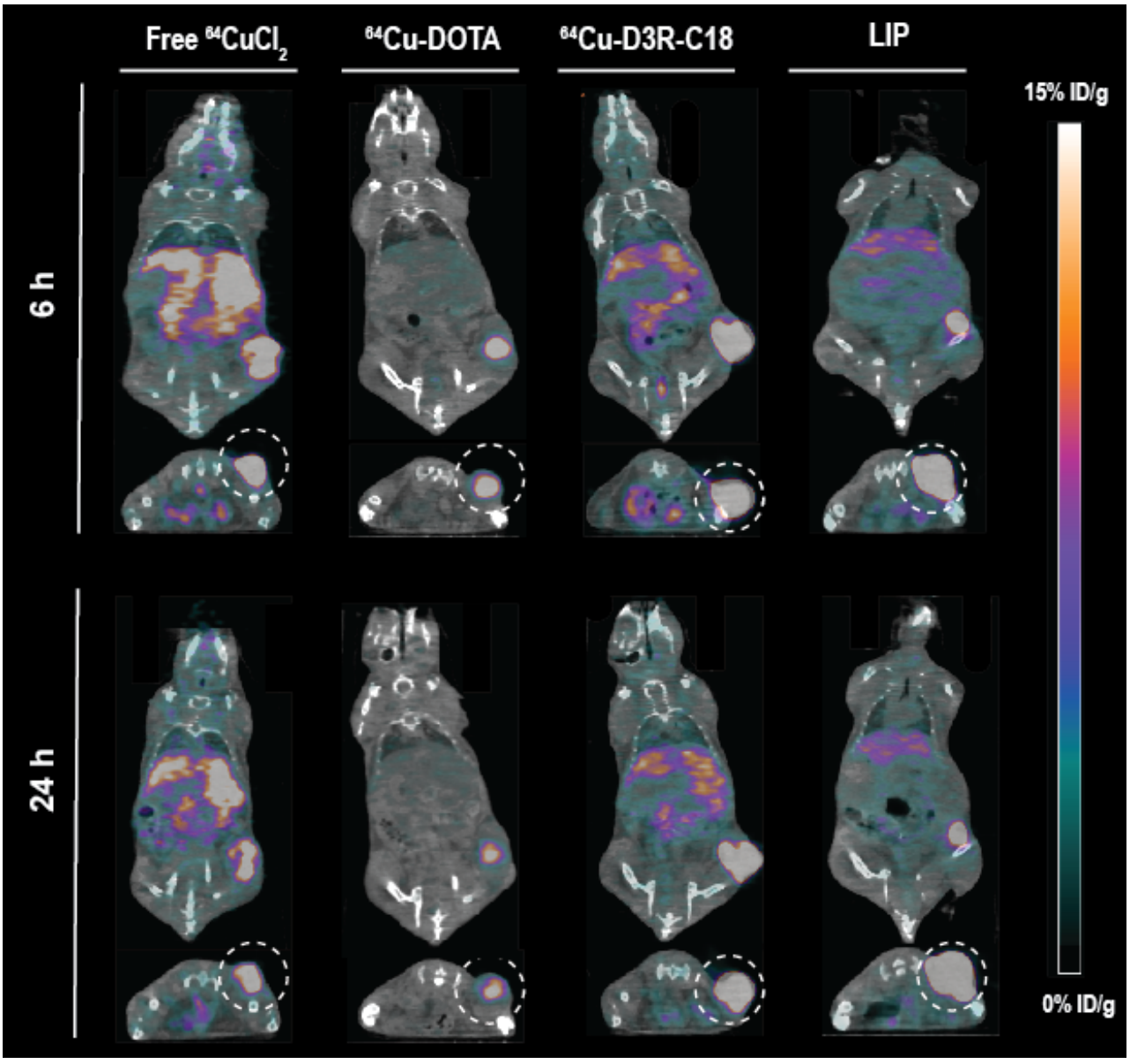

Figure 3.6. Coronal and transverse PET/CT images of tumor bearing mice injected with Free $^{64}CuCl_2$, ^{64}Cu-DOTA, ^{64}Cu-DOTA-3R-C18 or LIP at 6 hours and 24 hours. Tumors are highlighted in the transverse images by a dashed circle.

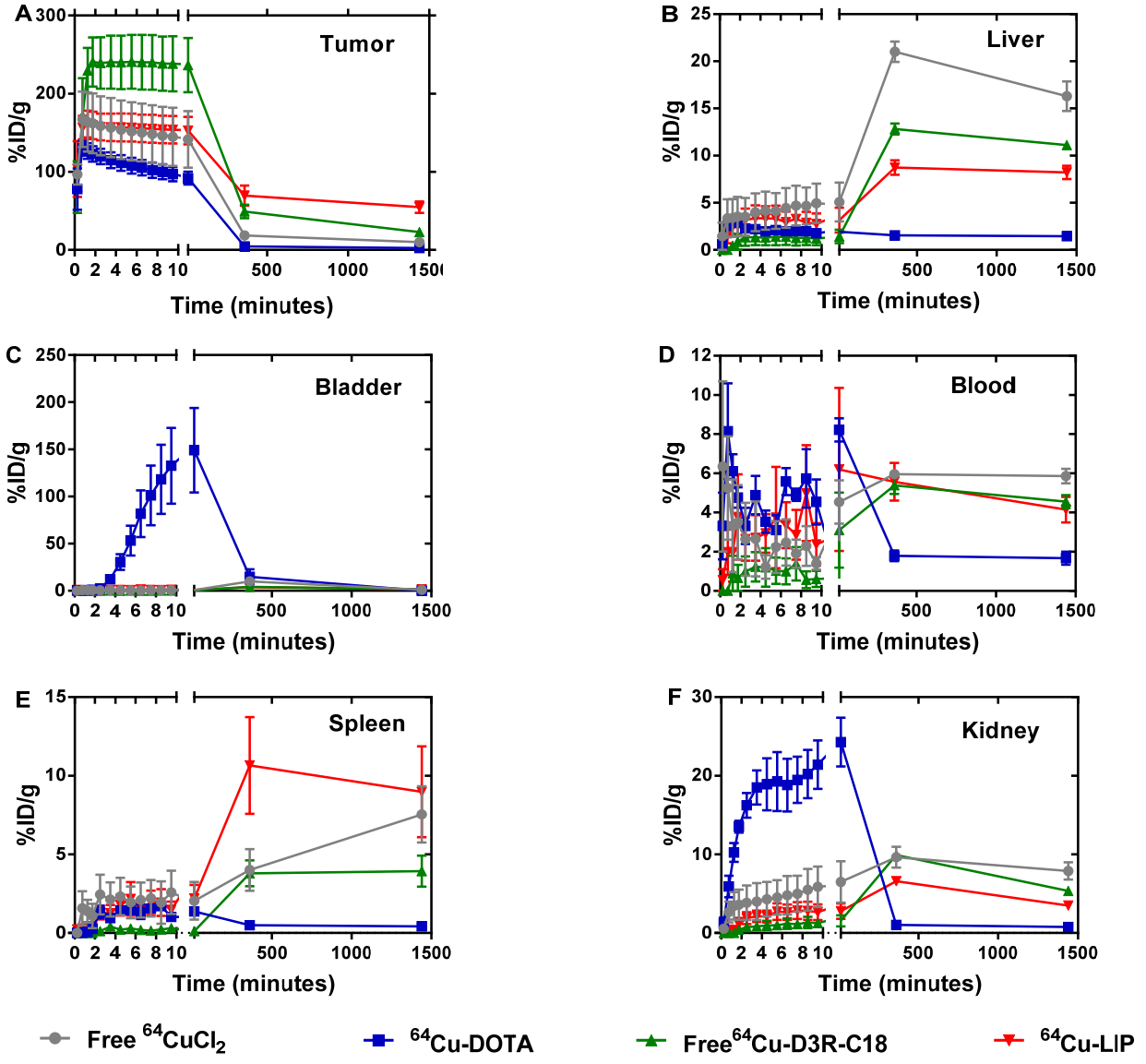

Figure 3.7. Biodistribution of free $^{64}CuCl_2$, ^{64}Cu-DOTA, free ^{64}Cu-D3R-C18 and ^{64}Cu-LIP in tumor (A), liver (B), bladder (C), blood (D), spleen (E) and kidney (F) based on PET imaging (A-F). The results are reported as mean and SEM (Free $^{64}CuCl_2$ and ^{64}Cu-DOTA n = 3, ^{64}Cu-D3R-C18 n = 5, and ^{64}Cu-LIP n = 4).

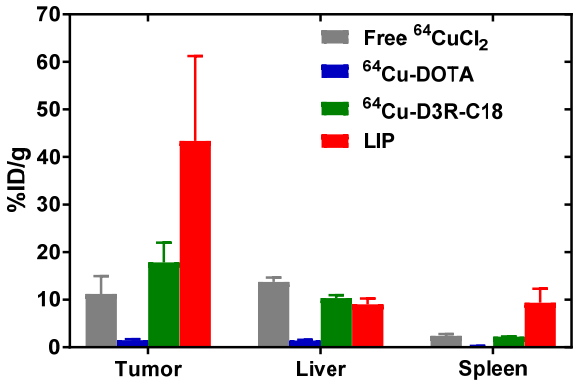

Figure 3.8. *Ex vivo* biodistribution of free $^{64}CuCl_2$, ^{64}Cu-DOTA, free ^{64}Cu-D3R-C18 and LIP. The animals were sacrificed after the 24-hour scan and excised organs were well-counted. The results are reported as mean ± SEM (free $^{64}CuCl_2$ and ^{64}Cu-DOTA n = 3, ^{64}Cu-D3R-C18 n = 5, and LIP n = 4).

3.3.5 Intratumoral distribution of radiolabeled samples

The distribution of radioactivities in the tumor region was analyzed by dividing the tumor region into small voxels and the radioactivity of each voxel was plotted as frequency distribution (Figure 3.9). Note that the first point in each plot represents the percentage of voxels with radioactivity concentrations lower than 1.6 %ID/g. These voxels are considered as empty, meaning the corresponding tumor region is non-radioactive. Free $^{64}CuCl_2$, ^{64}Cu-DOTA and ^{64}Cu-D3R-C18 distributed more rapidly through the tumor with less than 10% non-radioactive voxels at 5 minutes after the start of the PET scan, as compared with more than 15% non-radioactive voxels in the LIP. More than 40% non-radioactive voxels were observed in the ^{64}Cu-DOTA group at 6 h, showing the quick washout from the tumor. This corresponded with the relatively low tumor retention of this compound, as observed by PET (Figure 3.7). A shift towards lower activity (left shift) of the frequency distribution functions were observed for all formulations from 5 min to 6 h, indicating that the remaining radioactivity distributed gradually throughout the tumor. Free $^{64}CuCl_2$ exhibited a narrow radioactivity distribution with general voxel radioactivities from 0 to 100 %ID/g at 6 h, becoming even more narrow from 0 to 50% at 24 h. This demonstrated a fast distribution and wash-out from the tumor of free $^{64}CuCl_2$. ^{64}Cu-D3R-C18 distributed slower than free ^{64}Cu, although still with a gradually left-shifting curve. However, a very wide range of distribution from 0 to about 500% ID/g at 24 hours was observed. The slowest intratumoral distribution occurred for the LIP formulation. Virtually no change in the distribution of LIP was observed between 6 h and 24 h, both time points with a wide %ID/g distribution from 0 to about 800. LIP displayed a distribution with double peaks

at 6 h and 24 h, and the peak presented lower dose was very similar to the peak of ^{64}Cu-D3R-C18 at the same time point. This might be attribute to ^{64}Cu-D3R-C18 disassociated from liposomes due to a state of sink condition occurred when the formulation was injected in the tumor. Therefore, LIP might be a mixture of free ^{64}Cu-D3R-C18 and liposomes loaded with ^{64}Cu-D3R-C18 at 6 and 24 h.

In summary, free ^{64}CuCl, ^{64}Cu-DOTA and ^{64}Cu-D3R-C18 distributed very fast in 24 h. However, the fast distribution may be caused by rapid wash-out from tumor. Therefore, combining the results of intratumoral retention and distribution, ^{64}Cu-D3R-C18 might has the advantages to provide both better retention and distribution of radiation in first 6 h comparing to the two controls. LIP has the slowest intratumoral distribution among all the formulations. This might because of the slow release of ^{64}Cu-D3R-C18 from liposomes and the slow diffusion rate of liposomes in the tumor interstitium due to their lager size comparing to small molecules.

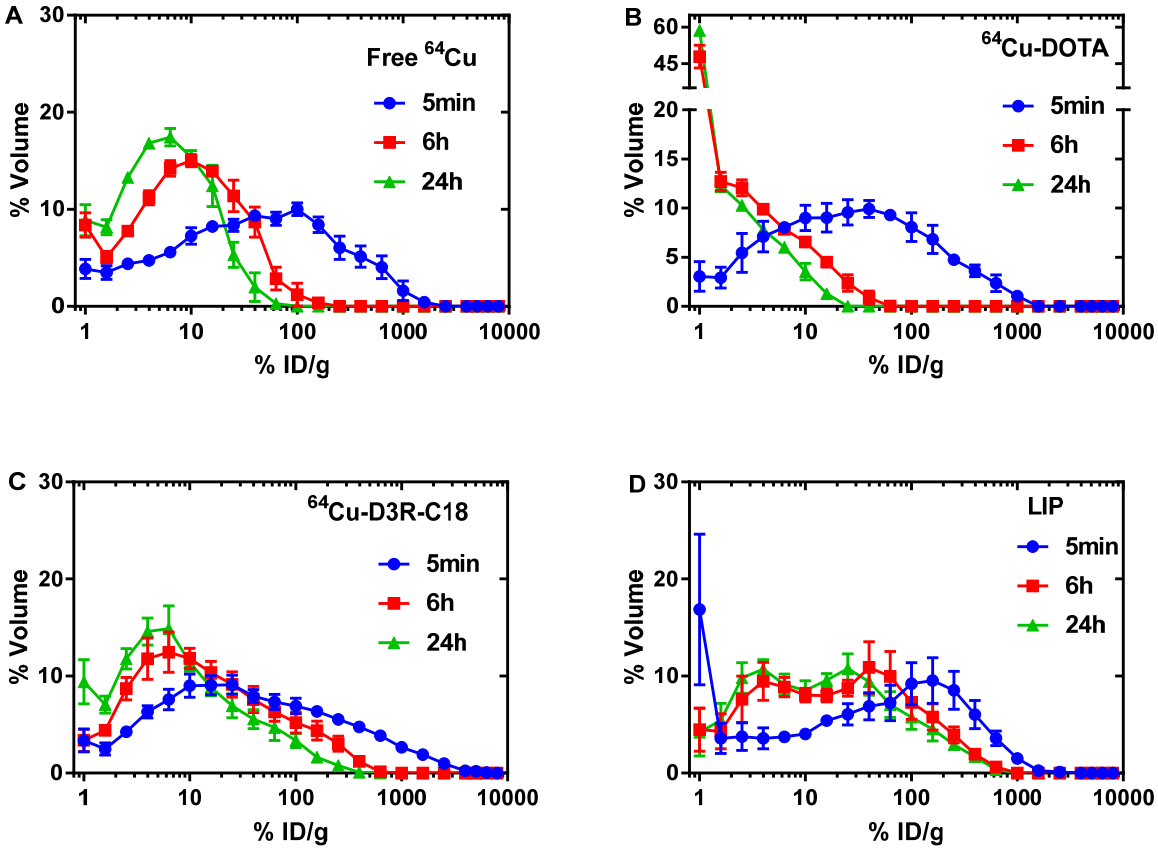

Figure 3.9. Frequency distribution functions of % voxels as a function of logarithmic % injected activity/mL for free $^{64}CuCl_2$ (A), ^{64}Cu-DOTA (B), ^{64}Cu-D3R-C18 (C) and LIP (D). Points in the curve present the mean-values of bin width. The first point of each formulation shows the percent voxels with % injected activity/mL lower than 1.6%. The results are reported as mean ± SEM (^{64}Cu free and ^{64}Cu-DOTA n = 3, ^{64}Cu-D3R-C18 n=5, and ^{64}Cu-LIP n = 4).

3.4 General discussion and future perspectives

Current brachytherapy techniques remain highly invasive requiring numerous implantations of radioactive sources. This makes it highly desirable to develop radioactive formulations that may be injected intratumorally at a single or a few sites, from where they would spread homogenously through the tumor, to irradiate the entire lesion. Such a system would also allow the use of alpha and beta emitting therapeutic radionuclides, many of which are currently becoming available in pharmaceutically relevant qualities. These are unconventional in traditional BT, due to the absorption of the emitted particles by the seed material, and the shorter half-lives of many alpha radionuclides in comparison to the time of seeds production make the system less beneficial. For this reason, short-range photon emitters are typically used in BT. Using single molecular entities or nanosized aggregates injected as solutions or dispersions would permit the use of alpha and beta radionuclides, causing the arsenal available in BT to be expanded significantly.

Optimally for brachytherapy, an injected substance would distribute from the injection point throughout the entire tumor, within a few hours. Here it would be well-retained, with minimal wash-out through blood and lymph. This would enable homogenous irradiation of the tumor tissue, and would permit the use of short-lived therapeutic radionuclides ($T_{½}$ = 5-10 hours). These would irradiate the tumor for a prolonged period, but would have decayed significantly once inevitable escape from the tumor occurred. Any radioactivity that did escape the tumor should not accumulate in non-cancerous tissues, but should be renally cleared with a short plasma half-life, to limit dose to healthy tissues and especially the bone marrow.

In this study, we prepared two novel DOTA-based chelating agents containing hydrophobic acyl chains and tri-arginine groups. These were designed to be able to transition from cell membrane to cell membrane, thus carrying radioactive material from the injection point through tissue in a gradual and controlled fashion. Cancer cell surfaces are known to be more negatively charged than normal cells [166]. Hence, highly positively charged tri-arginine groups were incorporated in order to increase the affinity to the negative lipid surface. The conducted partitioning studies of ^{64}Cu-D3R-C18 into liposomes supported this hypothesis by showing higher affinity to membranes with a higher degree of negatively charged head groups.

By radiolabeling with ^{64}Cu and conducting PET/CT *in vivo* studies, the biodistribution of the compound ^{64}Cu-D3R-C18 after intratumoral administration was investigated. The compound was administered both as the free compound (^{64}Cu-D3R-C18) and as a formulation in liposomes (LIP).

CMC measurements indicated that the free compound was present in the injection medium primarily as micelles. In both formulations, the radiolabeled compound was observed to exhibit substantial tumor retention, both as the free compound and in liposomes. In contrast, the control compounds, free $^{64}CuCl_2$ and ^{64}Cu-DOTA, exhibited rapid washout from the tumor. Free ^{64}Cu-D3R-C18 showed especially high retention during the initial 10 minutes, but significant wash-out at 6 hours and 24 hours. LIP had lower initial retention but a higher and more stable level of radioactivity at 6 and 24 hours. It is possible that this is due to slower clearance from the tumor interstitium, due to the larger particle size [26]. Both formulations showed some off-target accumulation in liver, spleen and kidneys, both in accordance with well-established biodistribution profiles for nanoparticulate substance [9, 178]. In this regard, it is important to note that free ^{64}Cu-D3R-C18 was present as micelles during the injection. After injection, these micelles would start to disintegrate into unimers because of dilution below the CMC value. Single unimers entering into the blood would be likely to exist as free molecules but may also be associated with albumin, which makes up about 60% of the total protein in the blood. The accumulation in liver, spleen and kidneys may be a result of association to this protein [179].

While tumor retention of injectable brachytherapy formulations has been addressed in other studies, the intratumoral distribution is seldom discussed. Previously, only rough estimations or comparisons of distribution between different formulations from PET images have been performed [26, 180]. In our study, voxel activity histograms were constructed to quantify and provide detailed information on the intratumoral radioactivity distribution of each formulation (Figure 3.9). One should note that the PET scan resolution and the reconstruction algorithm must be considered, since each voxel contains a large number of cancer cells and there is potential heterogeneity within one voxel [178]. The radioactivity from both formulations was observed to gradually distribute through the tumor, with the frequency distribution functions in Figure 3.9 shifting left and the magnitude of the curve increased as a function of time. According to the histograms, the distribution of ^{64}Cu-D3R-C18 is more homogenous than LIP in 24 h as the distribution curve became left-shift and unimodal as a function of time. The heterogeneous distribution of radiation is caused not only by the formulation design, but also the histopathological heterogeneity of the tumor. Tumor heterogeneity includes differences in cells densities, microenvironmental factors such as hypoxia and interstitial fluid pressure, and vasculature [181].

The formulations investigated in this study, showed relatively high retention up to 6 hours after injection. Because of this, the agent is potentially best suited for intratumoral delivery of relatively

short-lived therapeutic radionuclides, with half-lives on the order of 1-3 hours. The fast decay would prevent washout and off-target accumulation of high amounts of radioactive material. As is shown in figure 3.9, at 6 h post-injection, the radioactivity of both formulations is homogenously distributed within the tumor, with few empty tumor region and similar activity range from 0 to 1000 % ID/g. This entails that short-ranged emissions may be applicable for these systems, making especially alpha-emitters relevant. Alpha particles are particularly cytotoxic because of the high linear energy transfer radiation [182]. With half-lives of about 1 hour, the alpha-emitters ^{212}Bi (T½ = 61 min) and ^{213}Bi (T½ = 46 min) become relevant. The free D3R-C18 could be radiolabeled within < 1h and injected intratumorally as the free compound. Since D3R-C18 has a high initial dose in the tumor in the first 12 min (Figure 3.7A) and it embeds into membranes, using Auger therapy may also be potentially useful. In auger therapy, the burst of low-energy electrons can result in highly localized energy deposition in an extremely small tumor volume [183]. Recently it was shown that localization to the nucleus may not be necessary for a significant Auger therapeutic effect, but that localization to the membrane may also be effective [184, 185]. A useful, short-lived Auger radionuclide could be ^{103m}Rh, typically chelated with a sulfur-based chelator (T½ = 56 min). On the other hand, liposomes loaded with D3R-C18 might be promising with longer-lived radionuclides, due to their longer retention in tumors of up to 24 hours. However, this would still incur significant irradiation of healthy tissue, as the liposomes are seen to accumulate in organs beyond the tumor after 6 hours. In humans, however, it is possible that this window could be extended, due to slower pharmacokinetics. Even through the intratumoral distribution of liposome formulation is slower than D3R-18, the relatively long range and crossfire effect of beta minus particles can still provide relatively homogenous radiation dose [180, 184]. ^{64}Cu is not only useful as a PET imaging agent, but also a therapeutic radionuclide because of its abundant beta minus emissions (39%) and high LET auger electrons (43%) [152, 153, 186]. However, its half-life of 12.7 hours requires a long tumor retention for at least 24 hours.

3.5 Conclusion

We synthesized two novel non-toxic DOTA-triarginine-lipid conjugates, D3R-C16 and D3R-C18, to deliver radionuclides for brachytherapy. The compounds were designed to diffuse from cell membrane to cell membrane, to distribute radioactive material through the tumor tissue. The *in vitro* CMC and partitioning into liposomes with different surface properties of D3R-C16 and D3R-C18

have been investigated. The lead compound, D3R-C18, was radiolabeled with ^{64}Cu (>99% RCP in 30 min) and evaluated in vivo by intratumoral administration as both the free compound and a formulation in liposomes and imaged by PET/CT. The free compound showed a highest initial dose in first 12 min and a high degree of retention up to 6 h. The liposomal formulation showed a lower initial retention but increased long-term retention and with a slower intratumoral distribution than the free compound. Around 6 hours after injection, substantial wash-out from the tumor had occurred in both cases. Our results indicate that both D3R-C18 and LIP have potential in brachytherapy when paired with short-lived therapeutic radionuclides, notably alpha emitters such as Bi-213 and Auger emitters such as ^{103m}Rh (T½ = 56 min).

3.6 Experimental Section

3.6.1 Material

9-Fluorenylmethoxycarbonyl (Fmoc) amino acids and *O*-(7-azabenzotriazol-1-yl)-1,1,3,3-tetramethyluronium hexafluorophosphate (HATU) were purchased from GL Biochem or Iris Biotech GmbH. Novasyn TGR resin was purchased from Merck Chemicals GmbH. DOTA-tris(tBu)ester was purchased from Chematech. The freeze dried, premixed stealth liposome mixture of hydrogenated soy phosphatidylcholine (HSPC), cholesterol (CHOL) and 1,2-distearoyl-sn-glycero-3-phosphoethanolamine-N-[methoxy(polyethylene glycol)-2000] (DSPE- PEG2000) (565:382:53, molar ratio) was purchased from Lipoid. 1-palmitoyl-2-oleoyl-sn-glycero-3-phospho-(1′ -rac-glycerol) (POPG) and 1-palmitoyl-2-oleoyl-sn-glycero-3-phosphocholine (POPC) were purchased from Avanti Polar Lipids. Water was collected from a Milli-Q system (Millipore). All other chemicals were purchased from Sigma Aldrich. All the chemicals and reagents were of analytical grade and used without further purification.

Isotonic buffers, containing 10 mM 4-(2-hydroxyethyl)piperazine-1-ethanesulfonic acid (HEPES) with 150 mM sodium chloride (ISO-HEPES-NaCl) or 300 mM sucrose (ISO-HEPES-Sucrose) was prepared and adjusted to a final pH of 7.4.

CT26 (murine colon carcinoma) was purchased from ATTC (Rockville) and cultured in DMEM medium supplemented with 10% fetal calf serum and pen-strep (Invitrogen Inc) at 37 °C and 5 % CO2 in a humidified atmosphere. A commercial MTS assay was used to assess cytotoxicity. (Promega, CellTiter 96® AQueous One Solution Cell Proliferation Assay).

All radio-TLC analyses were performed on silica gel 60 F254 plates (Merck). 5% (w/v) ammonium acetate (NH_4OAc) in water-methanol (1:3) was used as eluent for ^{64}Cu-D3R-C16 and ^{64}Cu-D3R-C18, and 5% (w/v) ammonium acetate (NH_4OAc) in water-methanol (1:1) was used as eluent for ^{64}Cu-DOTA, ^{64}Cu-EDTA, ^{177}Lu-D3R-C16 and ^{177}Lu-D3R-C18. A MiniGita Star with a Beta Detector GMC probe (Perkin-Elmer) was used for analysis of radio-TLCs with radioactive peaks integrated using associated computer software. All radioactivities were measured either on a Veenstra Instruments dose calibrator VDC-505, or a liquid scintillation counting on a 300 SL spectrometer (HIDEX) with the energy range of 2 – 850 keV and linear calibration curve in the range of 20 – 800 Bq ($r^2 > 0.999$). The scintillation vials and the scintillation cocktail were purchased from PerkinElmer.

An Ez-pi+ surface tensiometer, with dyneprobe (diameter: 0.51 mm) and polypropylene sample cuvettes were purchased from Kibron to measure the surface tension.

Liposomes were prepared using a mini-extruder (Avanti Polar Lipids) or a LIPEX Thermobarrel Pressure Extruder (10 mL, Northern Lipids). The hydrodynamic size and zeta potential of liposomes were measured by dynamic light scattering (DLS) on a Zetasizer (Malvern) based on intensity with normal size distribution. The size was measured by dynamic light scattering (DLS) in ISO-HEPES-NaCl and the zeta potential was measured in ISO-HEPES-Sucrose. Lipid concentration was measured by ICP-MS (Thermo Scientifc, iCAP Q). Sephadex G-25 PD-10 columns (8.3 mL bed volume) were purchased from GE Healthcare. The phosphorous concentration of each liposome sample was measured by ICP-MS (Thermo scientific) with an internal standard of Gallium (10 ppb).

3.6.2. Preparation of ^{64}Cu

^{64}Cu was produced by proton irradiation of an electroplated ^{64}Ni target, and purified by anion exchange chromatography in aqueous HCl media. The ^{64}Cu was ultimately obtained in aq. HCl (1.0 M), and dried under argon flow for use in radiolabeling, as previously described [9, 174].

3.6.3. Synthesis of D3R-C16 and D3R-C18

The tetrapeptide H-Arg(Pbf)-Arg(Pbf)-Arg(Pbf)-Lys(Mtt) was synthesized on an Initiator Alstra peptide synthesizer (Biotage, Uppsala, Sweden) using a novasyn TGR resin (loading 0.2 mmol/g). The resin was swelled in dichloromethane (DCM) for 1 hour. Each residue was coupled for 30

minutes at room temperature using 4 eq. amino acid, 3.92 eq. HATU and 8 eq. 2,4,6-collidine in *N*,*N*-dimethylformamide (DMF). Fmoc deprotection was done using 20% piperidine in DMF for 3 plus 10 minutes. Afterwards, either stearic acid or palmitic acid was coupled using 4 eq. of fatty acid, 3.92 eq. HATU and 8 eq. 2,4,6-collidine in DCM:DMF (1:1) for 60 min. Mtt-deprotection was obtained using 2 % trifluoroacetic acid (TFA) in DCM. 25 washes of 10 mL for 5 min each were used. DOTA was coupled using 4 eq. of DOTA-tris-tBu, 3.92 eq. HATU and 8 eq. 2,4,6-collidine in DMF for 1 hour. The final products were cleaved for 3 hours using TFA/water/triisopropyl silane (95:2.5:2.5) after which the cleavage solvent was partially removed under reduced pressure and the peptide precipitated in diethyl ether. The cleaved products were dissolved in DMSO:water (5:95) and purified using semi-preparative HPLC (Waters 600 Pump & Controller and a Waters 2489 UV/Visible Detector). The C18 peptide was purified employing a Waters XTerra® C_{18} 5 µm (30 x 250 mm) column. Eluent: (A) 5 % acetonitrile, 0.1 % triethylamine (TFA) in water, (B) 0.1 % TFA in acetonitrile. Gradient profile; linear gradient from 25 % B to 45 % B over 40 min. Flow rate; 40 mL/min. The product was collected from 18-30 min. The C16 peptide was purified employing a Waters XTerra® C_{18} 5 µm (19 x 150 mm) column. Eluent: (A) 5 % acetonitrile, 0.1 % triethylamine (TFA) in water, (B) 0.1 % TFA in acetonitrile. Gradient profile; linear gradient from 20 % B to 40 % B over 20 min. Flow rate; 17 mL/min. The product was collected from 12-15 min. The products were lyophilized to obtain a white powder and the overall yield was 250 mg. The purity of the products was monitored by analytical HPLC using a Waters XBridge® C_{18} 5 µm (4.6 x 150 mm) column. Eluent: (A) 5 % acetonitrile, 0.1 % TFA in water, (B) 0.1 % TFA in acetonitrile. Gradient profile; linear gradient from 0 % B to 100 % B over 15 min. Flow rate; 1 ml/min. Purity >95 %. Rt. 11.0 min (C16) and 11.1 (C18). MALDI-TOF MS (Bruker Reflex, Bruker Daltonics, Billerica, MA, USA) (positive mode): Calc. $M+H^+$: 1238.8 Da., Obs. $M+H^+$: 1238.8 Da. (D3R-C16). Calc. $M+H^+$: 1266.9 Da., Obs. $M+H^+$: 1266.9 Da. (D3R-C18).

3.6.4. Cytotoxicity of D3R-C16 and D3R-C18

Cells were plated onto 96 well plates at a density of 4000 cells/well the day before the start of experiment. The original culture medium was replaced by medium containing increasing amounts of the indicated agents. After 24 h incubation with drugs, the medium was removed and the cells were further incubated for another 48 hours. To measure metabolically active cells, 100 µl of MTS solution

was added to the wells and incubated until sufficient amount of color was developed and within the linear range. The absorbance was measured at 490 nm using a microplate reader (Sunrise, Tecan).

3.6.5. Surface tension measurements

D3R-C16 or D3R-C18 was dispersed in ISO-HEPES-NaCl or ISO-HEPES-Sucrose for a final concentration of 250 μM as stock solutions. Sample series were prepared by diluting the stock solutions with ISO-HEPES-NaCl or ISO-HEPES-Sucrose into concentrations of 125, 62.5, 31.25, 15.63, 7.81, 3.91, 1.95, 0.98 and 0.49 μM. The surface tension of the sample was measured by the Du Noüy method with a platinum probe. For each sample, the measurements were repeated until three consecutive measurements varied with less than 1 mN/m between them. Based on the critical micelle concentration of D3R-C18, a micellar dispersion of D3R-C18 in ISO-HEPES-Sucorse (2.0 mM) was prepared. The zeta potential of D3R-C18 micelle were measured by a Zetasizer (Malvern).

3.6.6. Radiolabeling of D3R-C16 or D3R-C18

A micellar dispersion of D3R-C16 or D3R-C18 in ISO-HEPES-NaCl (2.0 mL, 200 μM) was added to dried $^{64}CuCl_2$ (about 300 MBq) or dried $^{177}LuCl_3$ (about 140 MBq). The resulting mixtures were magnetically stirred at 55 ℃ (with $^{64}CuCl_2$) or 90 ℃ (with $^{177}LuCl_3$) for 30 minutes. The formation of ^{64}Cu-D3R-C16 and ^{64}Cu-D3R-C18 was confirmed by comparing the obtained retention factor (R*f* = 0.30 – 0.40, and R_f = 0.40 – 0.50, respectively) with that of a non-radioactive chemically identical reference compound (See SI.1). The R*f* values for ^{177}Lu-D3R-C16 were 0.2 - 0.25, and the R*f* values for ^{177}Lu-D3R-C18 were 0.15 - 0.2. Free $^{64}Cu^{2+}$ and $^{177}Lu^{3+}$ both remained at the origin (R*f* = 0). The radiochemical purity (RCP) was > 95%, for all samples.

3.6.7. Preparation of liposomes for membrane partitioning studies

Three different liposomes types were prepared: 1) POPC only, 2) POPC-POPG (9:1, w/w), 3) commercially available stealth lipid mixture (*see above*). POPC or the POPC-POPC mixture was freeze-dried from tert-butanol:water (9:1). The resulting lyophilizates or the stealth lipid mixture (187.5 mg) was then hydrated with ISO-HEPES-NaCl (5.0 mL) at 65 ℃ for 60 minutes by magnetical stirring. This was followed by sizing through a mini-extruder with a cut-off size of 100 nm. Size, PDI

and zeta potential of all three preparations are listed in Table 3.2. The liposomes were diluted to lipid concentrations of 0.4, 1.0 and 4.0 mM for partitioning studies.

Table 3.2. Properties of liposomes for partitioning studies

	POPC	POPC+10% POPG	Stealth
Size (nm)	120.6 ± 0.3	129.6 ± 0.9	134.2 ± 0.8
PDI	0.040 ± 0.02	0.07 ± 0.01	0.05 ± 0.02
Zeta potential (mV)	-2.3 ± 0.6	-49.1 ± 0.6	-2.7 ± 0.3

3.6.8. Partitioning of D3R-C16 and D3R-C18 radiolabeled with ^{64}Cu or ^{177}Lu into liposomes

The kinetics of partitioning ^{64}Cu-D3R-C16 or ^{64}Cu-D3R-C16 into liposomes were studied in order to assess the equilibrium time of the process. A dispersion of ^{64}Cu-D3R-C16 (200 μM) in ISO-HEPES-NaCl (100 μL) was added to POPC liposomes (900 μL, 0.4 mM). The resulting mixture was magnetically stirred at 37 ℃. Aliquots were analyzed by size-exclusion chromatography (SEC) at 10, 30, 60, 120 and 180 minutes after addition. The mixture (100 μL) was applied to a PD-10 cartridge and eluted with ISO- HEPES-NaCl. Two consecutive fractions of 5.5 and 4.5 mL were collected. The radioactivities of the two collected fractions and the column were measured by dose calibrator. The liposome fraction eluted in the first 5.5 mL, whereas free ^{64}Cu-D3R-C16 and ^{64}Cu-D3R-C18 were retained by the column. The partitioning of the radiolabeled constructs into liposomes was calculated as the ratio of the radioactivity of the liposomes fraction to the total radioactivity of the fraction of liposomes and the column.

Next, the partitioning of ^{64}Cu-D3R-C16 and ^{64}Cu-D3R-C18 into liposomes with different lipid compositions and different concentrations was studied. A dispersion of ^{64}Cu radiolabeled D3R-C16 or D3R-C18 (200 mM, about 6 MBq) in ISO-HEPES-NaCl (30 μL) was added to POPC, POPC-POPG (9:1) or stealth liposomes (270 μL, 0.4 mM, 1.0 mM or 4.0 mM) respectively. The resulting mixtures were magnetically stirred at 37 ℃ for 60 minutes. The mixtures were analyzed by SEC by applying 200 μL to a PD-10 cartridge (see above). The liposome fraction eluted in the first 5.5 mL, whereas free ^{177}Lu-D3R-C16 and ^{177}Lu-D3R-C18 were retained by the column.

An ISO-HEPES-NaCl dispersion containing the ^{177}Lu-D3R-C16 (30 μL, 200 μM) or ^{177}Lu-D3R-C18 (30 μL, 200 μM) was added to stealth liposomes (270 μL, 0.4 mM, 1.0 mM or 4.0 mM). The resulting mixtures were magnetically stirred at 37 ℃ for 60 minutes. The mixtures were analyzed by SEC by applying 200 μL to a PD-10 cartridge (see above).

3.6.9. Interaction between ^{64}Cu-D3R-C16/^{64}Cu-D3R-C18 and stealth liposomes

^{64}Cu-D3R-C16 or ^{64}Cu-D3R-C18 were inserted into stealth liposomes by two methods: *direct mixing* and *partitioning*. *Direct mixing*: A dispersion of ^{64}Cu-D3R-C16 or ^{64}Cu-D3R-C18 (100 µM) in ISO-HEPES-NaCl (1.0 mL) was added to stealth lipid mixture powder (4.5 mg) in a glass vial, and the resulting mixtures (lipid concentration: 10 mM) were sonicated at 65 ℃ for 30 minutes. *Partitioning*: A dispersion of ^{64}Cu-D3R-C16 or ^{64}Cu-D3R-C18 (200 µM) in ISO-HEPES-NaCl (300 µL) was added to preformed liposomes in ISO-HEPES-NaCl (lipid concentration: 20 mM, 300 µL) in a 2 mL glass vial. The mixture was magnetically stirred at 55 ℃ for 60 minutes. After radiolabeling the liposomes, the mixtures made from each method were analyzed by SEC by applying 200 µL to a PD-10 cartridge (see above). In addition, a test for flip-flop of the radioactive compounds between the membrane leaflets was carried out. Samples of each type of radiolabeled liposomes were diluted 1000 or 10000 times with ISO-HEPES-NaCl. The resulting diluted samples were then incubated at 37 ℃ with gentle stirring. After 2 or 24 hours incubation, each diluted sample was analyzed by SEC by applying 1.0 mL to a PD-10 cartridge and eluting with ISO-HEPES-NaCl. Two consecutive fractions of 5.5 (liposomes) and 4.5 mL (small molecules) were collected. 1.0 mL of each of the collected fractions was measured by liquid scintillation. In order to determine the total radioactivity of the sample applied on the PD-10, 10 µL of the 1000x dilution or 100 µL of 10000x dilution were also measured by liquid scintillation.

3.6.10. Preparation of radioactive samples for *in vivo* experiments

The radioactivity concentration of all the ^{64}Cu radiolabeled samples was 40 MBq/mL at the time of injection. **Free ^{64}Cu:** ISO-HEPES-NaCl (500 µL) was added to dried $^{64}CuCl_2$ (160 MBq) and the mixture was stirred at 55 ℃, for 60 minutes. 50 µL of the sample was pipetted into a glass vial and the removed radioactivity was measured. The transfer efficiency, expressed as the ratio of the measured radioactivity to the theoretical maximum radioactivity of the withdrawn sample, was calculated to be 84%. The sample was then diluted with additional ISO-HEPES-NaCl (250 µL) to a concentration of 40 MBq/mL. **^{64}Cu-DOTA:** A solution of DOTA (100 µM) in ISO-HEPES-NaCl (1.1 mL) was added to dried $^{64}CuCl_2$ (160 MBq) and the mixture was stirred at 55 ℃ for 60 minutes. 100 µL of the sample was withdrawn and the radioactivity was measured. The transfer efficiency was 96%. Radio-TLC was conducted and the R_f of the ^{64}Cu-DOTA complex was 0.3-0.4 with a

radiochemical purity of >99%. **^{64}Cu-D3R-C18:** A dispersion of D3R-C18 (100 μM) in ISO-HEPES-NaCl (1.1 mL) was added to dried $^{64}CuCl_2$ (160 MBq) and the mixture was stirred at 55 ℃ for 30 minutes. The transfer efficiency was 91%. Radio-TLC confirmed the formation of ^{64}Cu-D3R-C18 in >95% RCP. **Liposomes loaded with ^{64}Cu-D3R-C18 (LIP):** A dispersion of D3R-C18 (200 μM) in ISO-HEPES-NaCl (500 μL) was added to dry $^{64}CuCl_2$ (160 MBq) and the mixture was stirred at 55 ℃ for 30 minutes. Radio-TLC confirmed the formation of ^{64}Cu-D3R-C18 in >95% RCP. Empty stealth liposomes had been prepared by hydrating the purchased stealth lipid mixture with ISO-HEPES-NaCl and sizing using a LIPEX Thermobarrel Pressure Extruder, as described above. The mean diameter of the resulting liposomes was 115 nm (PDI = 0.033) and the zeta potential was 12.7 ± 1.3 mV. The lipid concentration was 68 mM. ISO-HEPES-NaCl containing empty stealth liposomes (550 μL, 20 mM) was added to the ^{64}Cu-D3R-C18 suspension (200 mM, 550 μL). The mixture was stirred at 55 ℃ for 60 minutes. PD-10 analysis was conducted as described above and showed 98% partitioning of the radioactivity into the liposomes.

3.6.11. Murine cancer model

All experimental procedures were approved and conducted under the guidelines of The Danish Animal Experiments Inspectorate.

In vitro growth of CT26 wildtype cells (murine colon carcinoma, ATCC, Virginia, US) were acquired in RPMI (Roswell Park Memorial Institute) medium supplemented with 10 % heat-inactivated Fetal Calf Serum (FCS) and 1 % Penicillin-Streptomycin (Invitrogen, Carlsbad, US) retained in 5 % CO_2 incubator at 37 ° C. Immunocompetent Balb/C mice from Charles River were inoculated with tumor cells after one week of adaptation. All 20 mice included were inoculated subcutaneously with 3 x 10^5 CT26 wildtype cells in 100 μL medium on the right flank and hereafter monitored for weight and tumor size continuously for study purposes and to monitor the health of the mice. Tumor sizes were calculated from the formula of $0.52 \cdot (L^2 \cdot W)$, where L represents the length and W for the width, measured by external caliper.

Animals were included in the study when tumors were approximately 400 mm^3. Four different ^{64}Cu-compounds were investigated by PET/CT scanning to verify the diffusion after intratumoral injection: Free ^{64}Cu (n = 4), ^{64}Cu-D3R-C18 (n = 6), ^{64}Cu-DOTA (n = 4), and LIP (n = 6).

3.6.12. PET imaging and data analysis

Mice were injected intratumorally with ^{64}Cu-compounds in concentrations of 40 MBq/mL. During the scan procedures, mice were anaesthetized using 3-4 % sevoflurane (Abbott Scandinavia AB) mixed with 35% O_2 and 65% medical grade air and placed on heating pads to stabilize body temperature. Two mice were positioned side-by-side, separated by a 6 mm polystyrene block for PET/CT imaging using Inveon® small animal PET/CT system with CT based PET image attenuation (Siemens Medical Systems, Malvern, PA, USA). The protocol included a 12-minute PET scan, followed by a CT scan. Mice were fixed on a bed inside the scanner with the syringe placed and the needle fixed centrally in the tumor and ready for injection. Upon initiation of the first scan, mice were slowly injected intratumorally, to investigate the initial dynamics of the tracer diffusion. Following this, two further scans were included; a 6 hour time point (5 minutes scan time) and a 24 hour time point (12 minutes scan time). Reconstruction of PET scans were performed using maximum a posteriori (MAP) reconstruction algorithm (voxel size: 0.815x0.815x0.796 mm; resolution (FWHM) 1.2 mm). The 12 minutes scan at injection was reconstructed in 4x30 second and 10x60 second time frames to observe the dynamics of diffusion. The two last time points were reconstructed in a single time frame.

Image analysis was performed using commercially available Inveon software (Siemens Medical Systems, Malvern, PA, USA). Regions of interest (ROIs) were manually drawn based on the co-registered PET/CT images. The following ROIs were constructed; tumors (complete volume delineated), liver, spleen, kidney, bladder, and blood. Blood activity was estimated from a constructed ROI covering the left ventricular lumen of the heart. ROIs in the left ventricle and abdominal aorta were subsequently segmented to only include the voxels displaying above 80% of maximum activity with the original ROI. From the obtained uptake values all data was calculated into % ID/g for each organ. Furthermore, voxel values from tumor ROIs were used to generate histograms for substance diffusion over time in the tumor region.

3.6.13. Well counting

After the last scan time, all mice were sacrificed and tumor, spleen, and liver tissue was collected and well counted (Wizard, Perkin Elmer, US). Tissue samples were counted for 120 seconds, and

radioactivities recorded and corrected for isotope decay and well counter efficiency. Final results are presented in %ID/organ calculated from activity and the weight of the specific organ collected.

3.6.14. Statistics

The statistics on *in vitro* data were calculated in PRISM (version 7.04) using Tukey's multiple comparison test with *post hoc* two-way ANOVA. For *in vivo* data, due to the unequal sample sizes, the statistics were calculated by one-way ANOVA with Tukey's multiple comparison test. Probability values below 0.05 ($p<0.05$) are considered statistically significant.

Chapter 4. Development of Injectable *in situ* Solidifying Depots for Controlled Release of Organometallic Anticancer Compounds

4.1 Background

Chemotherapy is one of the most commonly used treatment for cancer therapy that uses one or more anti-cancer agents to kill cancer cells. Some current clinical chemotherapeutic agents and their mechanisms have been introduced in Section 1.4.1, Chapter 1. Although Platinum (Pt) coordination complexes have no alkyl groups, they are usually classified as alkylating agents due to their cross linking to DNA molecules in a similar way as standard alkylating agents. Consequently, DNA replication is inhibited by forming DNA-Pt complexes.

Cisplatin (Scheme 4.1A) was one of the first inorganic complexes found to exhibit biological activity by binding to DNA and interfering with its repair mechanism [187, 188]. Cisplatin was proven to be an effective drug for the treatment of certain cancer types, including sarcomas, cancers of soft tissue, bones and blood vessels [189]. Due to the resistance and numerous undesirable side effects such as kidney problems, allergic reactions and decrease immunity to infections of cisplatin, other platinum (Pt)-based drugs were developed. So far, FDA has approved three platinum-based drugs, namely cisplatin, carboplatin, and oxaliplatin (Scheme 4.1), for clinical treatment of various cancers. However, the Pt-based drugs display the common side effects, toxicity and drug resistance, which limit the wide clinical application of these drugs [190].

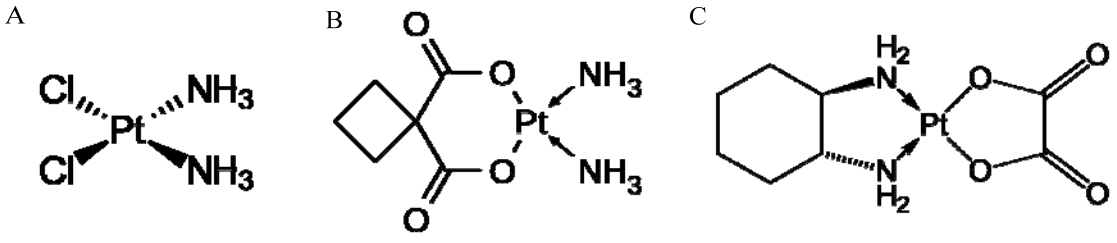

Scheme 4.1. Chemical structure of cisplatin (A), carboplatin (B) and oxaliplatin (C).

In order to achieve a higher activity with lower toxicity than current approved Pt-based drugs and overcome drug resistance problems, there has been a growing interest in the development of anti-cancer drugs based on other transition metals [191, 192, 193]. Titanium (Ti) has emerged as a promising chemotherapeutic metal among a few others [194, 195]. Ti-based compounds are more

effective than equitoxic doses of cisplatin *in vitro* [196]. Budotitane (Scheme 4.2A) was the first non-Pt complex that have evaluated in clinical trials. The encouraging preclinical results showed budotitane had a high and effective activity towards colon tumor cells [191]. Another Ti-based drug in clinical trial, titanocene dichloride (Cp_2TiCl_2, Scheme 4.2B), was effective towards cisplatin-resistant cells such as human ovarian carcinoma cell lines [191, 192, 193]. However, both drugs eventually failed in clinical trials due to their poor solubility and the high hydrolytic instability of Ti [194, 197]. The hydrolysis usually happens immediately when the drug is administrated.

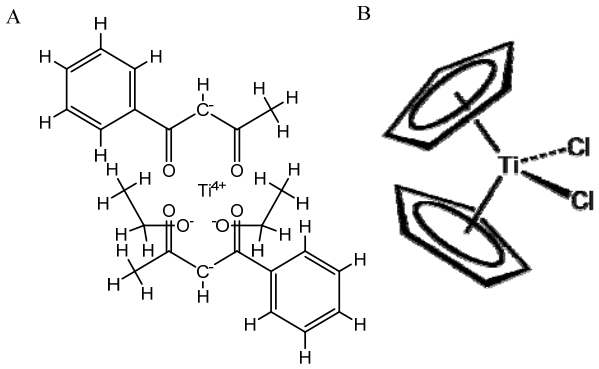

Scheme 4.2. Chemical structure of budotitane (A) and titanocene dichloride (B).

The development of titanium-stabilizing ligands has led to a new generation of Ti-based anticancer drugs [194, 196]. Tshuva et al. have introduced the ligand salan, a diamine bisphenalato compound, to improve the hydrolytic stability to Ti alkoxide complexes (Scheme 4.3A) [191, 194, 198]. The obtained Ti-based compounds displayed more effective activities and lower IC_{50} values against HT29 and OVCAR-1 cell lines in comparison with cisplatin [191]. Based on the developed structure-activity relationships [191], Huhn and co-workers further chelated Ti metal ion by substituting both terminal alkoxides groups (OR in Scheme 4.3A) with dipicolinic acid [198]. The resulting (salan)Ti(dipic) (SaTiDv1, Scheme 4.3B) was hydrolytically stable up to 2 weeks and exhibited a high cytotoxicity against HeLa S3 and Hep G2 cell lines.

The biodistribution of intravenously injected SaTiDv1 in dimethyl sulfoxide (DMSO) was evaluated in HT-29 colorectal tumor bearing mice by non-invasive positron emission tomography (PET) [194]. In this case, SaTiDv1 was radiolabeled by ^{45}Ti, which is a desirable PET radionuclide with an 85% positron branch, low β end energy of 1.04 MeV and a half-life of 3.1 h [199]. However, the results demonstrated that the circulation time of SaTiDv1 was extremely short, with a blood half-life of only 1.7 minutes. Consequently, the tumor accumulation could never achieve 1 %ID/g. Therefore, the re-

formulation of SaTiDv1 is required to improve the circulation time and the therapeutic efficacy of SaTiDv1.

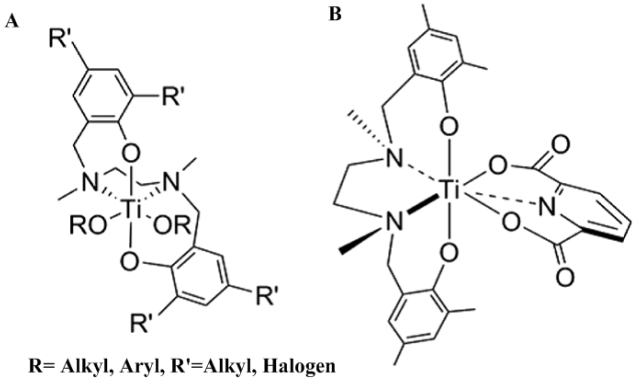

Scheme 4.3. New generation of Ti-based chemotherapeutic compounds: SaTi (A) and SaTiD (SaTiDv1 B).

4.2 Objective

Our collaborator Senior Researcher Fedor Zhuravlev from Center for Nuclear Technologies at the Technical University of Denmark has further modified SaTiD (SaTiDv2 , Scheme 4.4) in order to achieve a higher activity against cancer cells. Comparing to SaTiDv1, SaTiDv2 further increased the steric bulk by adding two benzene rings. The increase of steric bulk was found to increase the activity to against cancer cells [191]. Moreover, the strong electron donating ethers on aromatic rings could improve the binding to the Ti metal ion, which would further increase the cytotoxicity and stability of the compound [191].

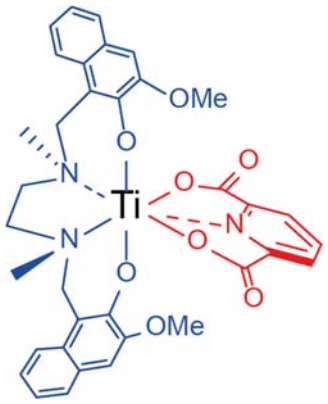

Scheme 4.4. Chemical structure of SaTiDv2.

In this project, we aimed to compare SaTiDv2 with SaTiDv1. Moreover, in order to achieve a high intratumoral dose with less systemic toxicity, SaTiDv2 was formulated into carbohydrate ester-based (sucrose acetate isobutyrate [SAIB] or lactose octaisobutyrate [LOIB], scheme 4.4A and B) *in situ*-forming depot for intratumoral administration. The depot formulation for SaTiDv2 was designed to have a slow-releasing profile based on carbohydrate ester, organic solvent and glycerol trioctanoate (GTO scheme 4.4C). In Chapter 2, we have developed a marker based on SAIB and ethanol for imaging guided surgery. Upon injection the marker in aqueous environment, a highly viscous gel-like marker formed due to the efflux of ethanol. Unlike this marker system, the depot formulation for SaTiDv2 contained a hydrophobic solvent GTO, which would diffuse from the depot and exchange with the water in the aqueous environment very slowly. Therefore, the depot formulation would keep its low viscosity for long time and the drug could slowly release from the formulation over a prolonged period without a high burst release.

Formulations containing different types of carbohydrate ester and organic solvents were compared. The therapeutic efficacy of one formulation was evaluated in tumor bearing mice.

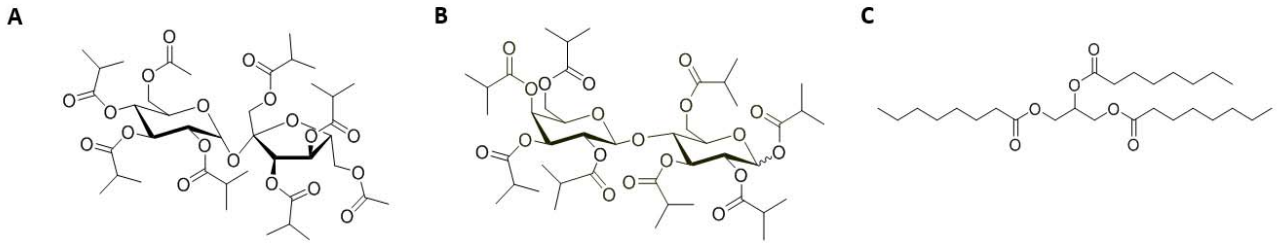

Scheme 4.4. Structure of materials for *in situ*-forming depot: sucrose acetate isobutyrate (SAIB, A), lactose octaisobutyrate (LOIB, B) and glycerol trioctanoate (GTO, C).

4.3 Results

4.3.1. *In vitro* Comparison of SaTiDv1 and SaTiDv2

The *in vitro* cytotoxicity of SaTiDv1 and SaTiDv2 was compared by treating CT26 cell line with different concentration of SaTiDv1 or SaTiDv2 in DMSO. Figure 4.1 presents the cytotoxicity of SaTiDv1 and SaTiDv2 towards CT26 cell line and both Ti complexes showed a high cytotoxic activity towards CT26 cell line. The half maximal inhibitory concentration (IC_{50}) values of two Ti complexes and DMSO were calculated using nonlinear regression fitting of dose-response curves in

GraphPaD Prism 7.04, and are presented in Table 4.1. The IC_{50} values of both Ti complexes were lower than the reference IC_{50} of cisplatin, which is the Pt-based therapeutic compound approved by FDA. Comparing to SaTiDv1, SaTiDv2. had a much lower IC_{50} of 1.21 µM indicating a higher cytotoxic activity towards CT26 cell line. The cytotoxicity results indicated that the adding of steric bulk and electron donating groups might increase the cytotoxic activity of the Ti complex, which was in line with developed structure-activity relationships of Ti complex [191]. According to the high cytotoxicity, SaTiDv2 was selected for the further *in vitro* release study and *in vivo* evaluation.

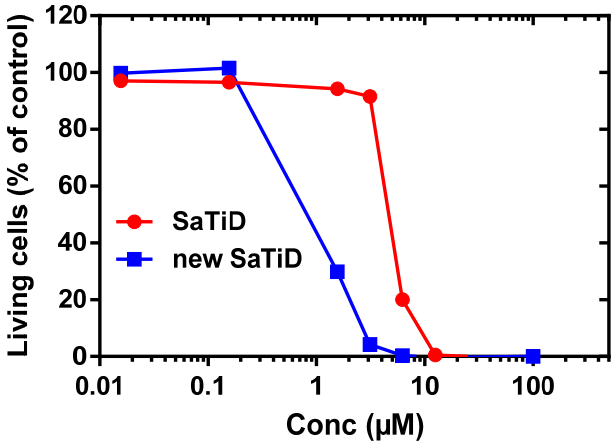

Figure 4.1. Cytotoxicity of SaTiDv1 and SaTiDv2 towards CT26 cells. CT26 cells (5000 cells/well the day before the start of experiment) were incubated for 72 h with increasing concentration of SaTiDv1 or SaTiDv2 and cell viability was evaluated using MTS assay. This experiment was performed once (n = 1).

Table 4.1. IC_{50} Values (µM) for SaTiDv1, SaTiDv2, solvent (DMSO) and FDA approved drug cisplatin towards CT26 cells. *the IC_{50} of cisplatin was measured by Ma et al. [200].

Compound	SaTiDv1	SaTiDv2	Cisplatin*
IC_{50} Values (µM)	4.84	1.21	10

4.3.2 Optimization of Depot Formulations for SaTiDv2

The carbohydrate ester *in situ*-forming drug delivery system is comprised of a water insoluble matrix material such as SAIB and LOIB, and an organic biocompatible solvent that is miscible with the matrix material and water [201]. Once the system is injected into an aqueous environment, due to the solvent induced phase inversion (SPI) process, the organic solvent will spread out and the water will diffuse in the system [201, 202]. This exchange of solvents causes the precipitation of the matrix

material resulting in the depot formation. Therefore, the selection of organic solvent in the formulation is crucial for controlling the release of drug.

In this study, the organic solvent was a mixture of glycerol trioctanoate (GTO) and an organic solvent, dimethyl sulfoxide (DMSO), propylene carbonate (PC) or benzyl alcohol (BA). The release of SaTiDv2 was optimized by varying the GTO ratio and type of organic solvent in the depot formulations. GTO is a highly hydrophobic solvent, which will stay in the formulation or diffuse into aqueous environment very slowly upon injection of the formulation. The purpose of adding GTO in the formulation is to lower the viscosity of the depot and avoid the formation of a highly viscous depot after the efflux of water miscible organic solvent causing drug precipitation in the depot or trapping of the drug due to the high viscosity of the depot. With GTO in the formulation, the drug molecules diffuse freely in the depot and have the chance to be released from a depot with low viscosity to the aqueous environment over long time. Besides GTO, the formulation consisted of 10% w/w DMSO, PC or BA. The water solubility and logP values of these three organic solvents are listed in Table 2. All the formulations prepared were injectable by using a 25G needle. The effect of SAIB or LOIB, the ratio of GTO, and the type of organic solvents on the *in vitro* release of SaTiDv2 were investigated and compared.

Table 4.2. Properties of organic solvents used in the formulations. [a]Information obtained from [201]. [b]Information obtained from [203]. [c]Information obtained from [204].

Solvent	Water solubility	LogP
Dimethyl sulfoxide (DMSO)	Completely miscible	-1.35b
Propylene carbonate (PC)	175 g/L at 20 ^{o}C	-0.41b
Benzyl alcohol (BA)	33g/L at 20 ^{o}C	1.1b

The *in vitro* release of SaTiDv2 from SAIB-based formulations containing different GTO ratio and organic solvent was firstly compared (Figure 4.2). Comparing the release of drug from the formulation with the same organic solvent (in each figure), the total cumulative release in 30 days of the drug was higher from the formulation with higher ratio of GTO. These results were in line with our hypothesis that more GTO causes formulation to be less viscous, therefore, the drug can be continuously released from the depot. Moreover, after the efflux of water miscible organic solvent, the hydrophobic component GTO might exchange with water very slowly and form a depot with smooth surface and small pores [205]. An increased amount of GTO might result in a structure with more pores or larger pores causing higher release of the drug. A higher burst release in 2 hours was

also observed from the formulation with the same organic solvent but more GTO. This might due to a faster diffusion of the organic solvent from a less viscous formulation.

Comparing the release of drug from the formulation with the same amount of GTO but different organic solvent (the line with same color), BA gave a lowest total cumulative release of the drug in 30 days among three organic solvents. Only 18 ± 2% of drug released in 30 days from the formulation with highest GTO amount (36%) and BA. BA is the most hydrophobic solvent (logP = 1.1) among all three solvents and it has a low water solubility of 33 g/L (corresponding to 3.3% w/w, Table 4.2). The solvents have low water solubility of below 7% w/w have been shown to cause a low drug release due to the limit of solvent diffusion to aqueous environment and water uptake [201]. DMSO gave a highest burst release of the drug (19 ± 3%) in 24 hours in comparison with PC (2.4 ± 0.1) and BA (4 ± 1) from the formulation with 27% GTO as an example. DMSO is hydrophilic and completely miscible with water, hence, it diffused into aqueous environment rapidly, once the formulation was injected into release buffer [201, 206, 207]. However, the viscosity of the formulation increased immediately after the efflux of DMSO. Therefore a lower total cumulative drug release observed from formulation with DMSO and 27% GTO (21 ± 1%) comparing to the release from the formulation with PC and same amount of GTO (30 ± 1%) in 30 days. In summary, PC is an optimal organic solvent in the formulation in order to achieve a high cumulative drug release in 30 days with a relatively low burst release.

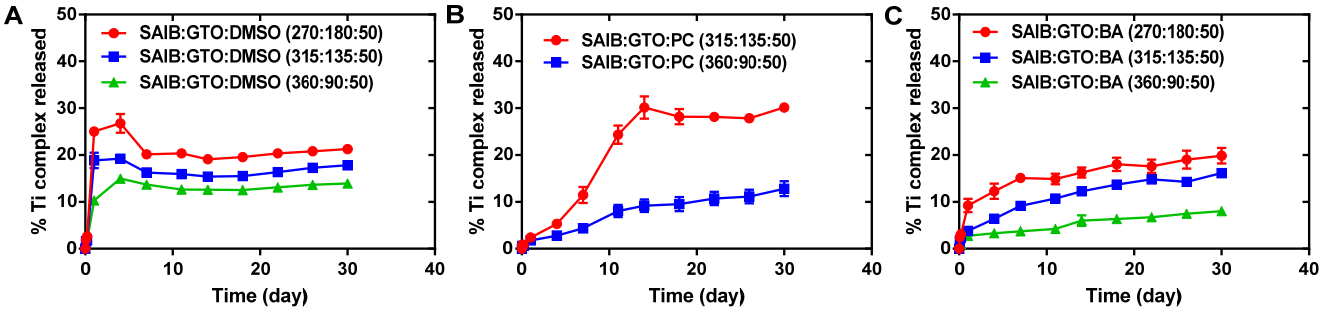

Figure 4.2. *In vitro* release of SaTiDv2 from the SAIB-based formulations with DMSO (A), PC (B) and BA (C). The formulations contained different amount of GTO (18-36% w/w) and 0.08% w/w SaTiDv2. All the ratios represent weight ratios. Data present as mean ± SEM, n = 3. The Ti element in each aliquot was measured by ICP-MS.

The *in vitro* release of SaTiDv2 from LOIB-based formulation containing different GTO ratio and organic solvents was also investigated (Figure 4.3). More GTO in the formulation with the same

organic solvent resulted in a higher total cumulative release and burst release of the drug. These results are in line with the previous release profiles from SAIB-based formulation, indicating GTO might have the same effect on LOIB formulations. Comparing different organic solvent in the formulation with same GTO amount (27 or 36%), a higher burst release at 24 hours was observed from the formulation with DMSO (6.5 ± 0.7 or 15 ± 3%) in comparison with that from the formulation with PC (1.9 ± 0.2 or 1.87 ± 0.3%) or BA (1.0 ± 0.2 or 1.3 ± 0.2%). The highest cumulative release of the drug in 30 days (22 ± 3%) was observed from the formulation with DMSO and 36% GTO. In general, the total cumulative release of the drug in 30 days from LOIB-based formulations was lower than that from SAIB-based formulations with the same GTO amount and organic solvent. It might because of the higher binding affinity of the hydrophobic drug with LOIB due to the more hydrophobic property of LOIB than SAIB. Moreover, the viscosity of LOIB-based formulation is higher than SAIB-based formulation before and after the efflux of organic solvent from the formulation to the aqueous solution.

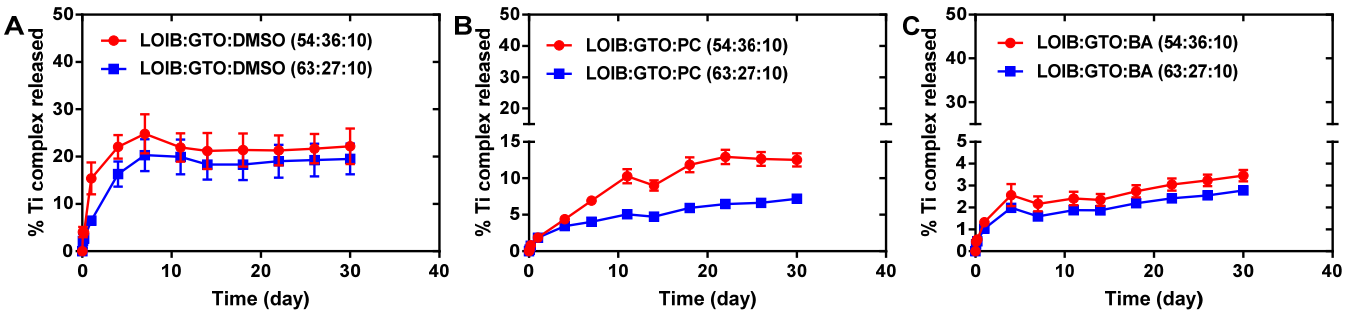

Figure 4.3. *In vitro* release of SaTiDv2 from the LOIB-based formulations with DMSO (A), PC (B) and BA (C). The formulations contained different amount of GTO (27 or 36% w/w) and 0.08% SaTiDv2. All the ratios represent weight ratios. Data present as mean ± SEM, n = 3.

According to all the *in vitro* release results, the release profile of SaTiDv2 could be tuned by changing carbohydrate ester such as SAIB and LOIB, GTO amount in the formulation and the selection of organic solvent. The ideal release profile for chemotherapeutic drug should be continuously release over 30 days with a low burst release. Therefore, formulation of SAIB:GTO:PC 63:27:10 w/w was selected for further *in vivo* efficacy evaluation.

4.3.3 *In vivo* Efficacy Evaluation of the Formulation Containing SaTiDv2

A preliminary *in vivo* efficacy evaluation of the formulation containing SaTiDv2 was performed in CT26 syngeneic tumor-bearing Balb/c mice by intratumoral injection. Formulation consisting of SAIB:GTO:PC 63:27:10 w/w loaded with 0.16% w/w SaTiDv2 was selected for *in vivo* evaluation. Note that the concentration of SaTiDv2 in the formulation for *in vivo* evaluation was 2-fold higher than the concentration used for *in vitro* release study. This is because we assumed that the higher concentration of chemotherapeutic drug in the formulation could gave a higher *in vivo* efficacy. 0.16% w/w was the highest concentration of SaTiDv2 we could achieve in the selected formulation. The injected volume was 50 μL for each mice and the dose was about 4 mg/kg. The efficacy of the treatment group with the formulation injected in tumor-bearing mice was compared to the control group of non-treatment mice.

The tumor sizes of treatment and control groups were monitored until their size reached a volume of ≥1000 mm^3 or if extensive abrasions were observed on the skin surrounding the tumor. The results (Figure 4.4A) show the growth of the tumor injected with the formulation containing SaTiDv2 was suppressed up to 18 days comparing to the control group. Moreover, Kaplan-Meier survival curves (Figure 4.4B) show that the group with the formulation prolonged survival. In the treatment group, 100% survival has been observed for 24 days. However, the mice were euthanized due to big tumor size or extensive abrasions observed surrounding the tumor in the control group from 24 days. There was no significant weight change observed after the injection of the formulation containing SaTiDv2 to the tumor, indicating there might not be severe side effect during the treatment. The *in vivo* evaluation results have shown the depot formulation containing SAIB:GTO: PC 63:27:10 w/w with 0.16% w/w SaTiDv2 had the potential to delay the tumor growth and improve the survival rate with low side effect. However, the single injection of the formulation was not effective for the complete tumor elimination. The average concentration of 30% released SaTiDv2 in the tumor could be estimated to be about 360 μM, assuming homogenous intratumoral distribution of the compound in a 100 mm^3 tumor. According to the *in vitro* cytotoxicity results (Figure 4.1), this estimated concentration is 300-fold higher than IC_{50} and might be enough to eliminate all the cancer cells. The reason of this ineffective treatment might be the insufficient release of the drug from the formulation, as only 30% total cumulative drug released and there was no further release after 14 days from this formulation observed from *in vitro* release study. Moreover, the distribution of the drug in the tumor might be heterogeneous, and the drug might have a low retention in the tumor.

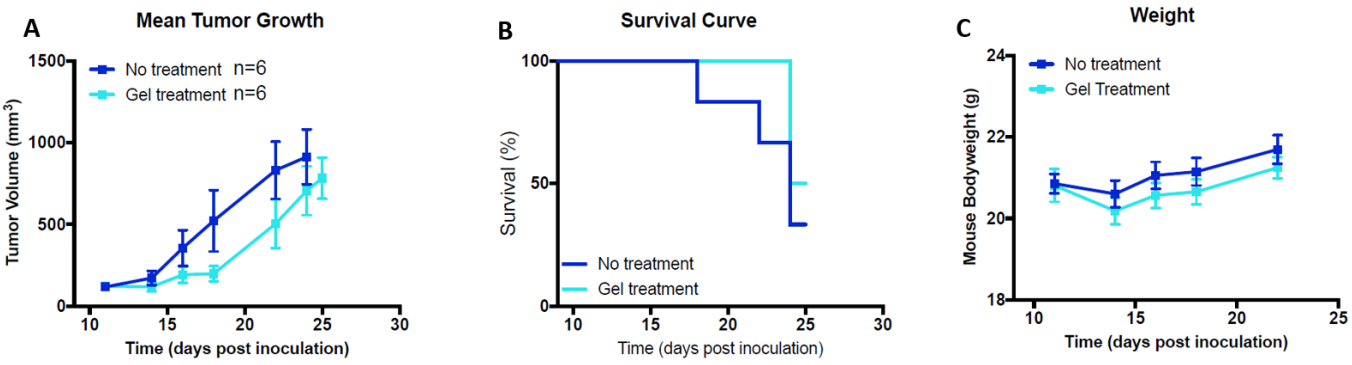

Figure 4.4. Therapeutic efficacy of intratumoral injection of SAIB:GTO:PC 63:27:10 w/w formulation containing 0.16% w/w SaTiDv2 in tumor bearing mice. Monitoring of tumor growth during treatment (A). Survival of mice under treatment and control group (B). Weight monitoring of mice during treatment (C). The data are presented as mean ± SEM, n = 6 for each group.

4.4 General Discussion and Future Perspective

Intratumoral injection is an effective administration method for chemotherapeutic agents locally to the tumor with minimal exposure to healthy tissues. The *in situ*-forming depot system based on carbohydrate ester, GTO and organic solvent has shown the potential to deliver SaTiDv2 to the tumor. However, an insufficient efficacy of the formulation was observed as the tumor could not be eliminated due to the low cumulative and non-continuous drug release from the depot during the treatment. New formulations with higher cumulative release and low burst release of the drug are desired. Both SAIB and LOIB might be too hydrophobic, hence, the hydrophobic SaTiDv2 has a high affinity to the depot material instead of efflux to surrounding aqueous environment. Other more hydrophilic carbohydrate ester such as a mixture of lactose octaacetate and lactose octapropionate (1:1 w/w, scheme 4.6) might be a potential formulation to improve the release profile of SaTiDv2.

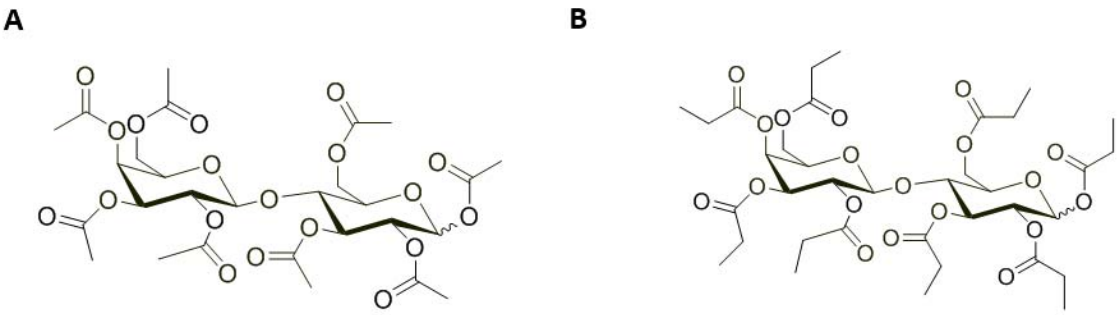

Scheme 4.6. Structure of lactose octaacetate (A) and lactose octapropionate (B).

One preliminary *in vitro* release study has shown a continuous and higher cumulative release of SaTiDv2 (48%, Figure 4.5) in 7 days than the release from SAIB or LOIB based depot formulation. However, the burst release was high as 27% in 1 hour and this might because of the high ratio of DMSO (15% w/w) used in the formulation. Therefore, the change of DMSO to PC or decreasing DMSO and increasing GTO amount in the formulation might be a solution to reduce the burst release. Moreover, the adding of polymer such as poly lactic-co-glycolic acid (PLGA) in the formulation could form a thick shell at the interface to reduce the burst release after injecting the formulation into aqueous environment [39].

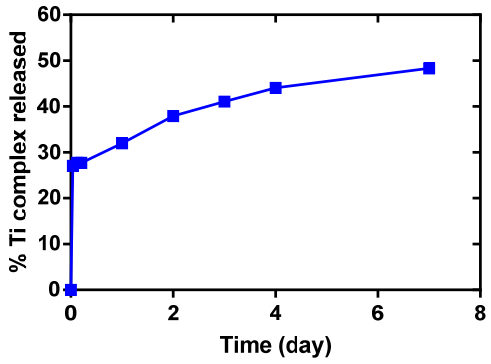

Figure 4.5. *In vitro* release of SaTiDv2 from the formulation containing 80% LAP (lactose acetate:lactose propionate 1:1 w/w), 15% DMSO, 5% GTO and 0.06% SaTiDv2 (w/w). n = 1.

Imaging modalities are noninvasive and effective ways to investigate the biological fate of a potential pharmaceutical. Recently, single photon computed tomography (SPECT) has been employed to clinically investigate the distribution of ^{195m}Pt radiolabeled cisplatin in order to relate the pharmacokinetics to the efficacy of treatment [208]. Similar to the technique to trace cisplatin, Ti-complex based drug could be radiolabeled by a highly desirable positron emitting radionuclide ^{45}Ti with 85% β branch, low β end point energy of 1.04 MeV and a half-life of 3.1 h [199]. Therefore, the biodistribution of ^{45}Ti radiolabeled Ti-complex drug could be obtained by the non-invasive positron emission tomography (PET). Zhuravlev et al. [194] have successfully employed PET to evaluate the biodistribution of ^{45}Ti radiolabeled SaTiD DMSO solution in tumor-bearing mice. The results showed that [^{45}Ti]SaTiD was metabolized in the liver with a fast hepatobiliary excretion pattern. PET could be a useful tool to study the *in vivo* behaver of SaTiDv2 and accelerate the clinical translation in future.

4.5 Conclusion

In this study, we have compared SaTiDv2 with SaTiDv1. SaTiDv2 is more toxic than SaTiDv1 with a 4-fold lower LC_{50} towards CT26 cells. We have also developed intratumorally injectable *in situ*-forming depot formulation based on carbohydrate ester (SAIB or LOIB) for controlling the release of SaTiDv2. The *in vitro* release of the drug could be modified by adding different amount GTO and using varying type of organic solvent (DMSO, PC or BA). The optimal formulation should give the highest cumulative release of SaTiDv2 in 30 days with low burst release. Among all the formulation tested, the formulation consisting of SAIB:GTO:PC 63:27:10 w/w was the best for the criteria, which gave about 30% total cumulative release in 30 days with only about 2% burst release after 1 day. Then this formulation consisting of SAIB:GTO:PC 63:27:10 w/w with 0.16% w/w SaTiDv2 was evaluated in tumor-bearing mice. Comparing to the control group without treatment, the growth of the tumor was suppressed by the depot formulation with the drug over 18 days. Moreover, 100% survival has been observed for 24 days in the group treated with the formulation in comparison with 67% survival in the non-treatment group. All these results have proved that the *in-situ* forming depot based on carbohydrate ester is a potential formulation for delivering SaTiDv2 to the tumor to delay the tumor growth and improve the survival rate.

4.8 Experimental Section

4.8.1 Material

Lactose octaisobutyrate (LOIB) and iodinated sucrose acetate isobytyrate (SAIB)-derivative (xSAIB) was kindly provided by the Danish company, Nanovi. The freeze dried, premixed stealth liposome mixture of hydrogenated soy phosphatidylcholine (HSPC), cholesterol (CHOL) and 1,2-distearoyl-sn-glycero-3-phosphoe- thanolamine-N-[methoxy(polyethylene glycol)-2000] (DSPE- PEG2000) (565:382:53, molar ratio) was purchased from Lipoid. Reagents for ICP-MS measurements were purchased from TraceSelect® and nitric acid was purchased from Fluka Analytical. Sucrose acetate isobutyrate (SAIB), glycerol trioctanoate (GTO), Trizma®base (Tris(hydroxymethyl)aminonethane), sodium chloride, and all other chemicals were purchased from Sigma Aldrich. All the chemicals and reagents were of analytical grade and used without further purification. All water was collected from a Milli-Q system (Millipore).

Isotonic buffer, ISO-TRIS, containing 2-Amino-2-(hydroxymethyl)-1,3-propanediol (TRIS, 10 mM) and sodium chloride (150 mM), was prepared and adjusted to a final pH of 7.8, using hydrochloride acid (0.1 M). A liposomal dispersion (50 mM) was prepared in ISO-TRIS by sonication for 1 h at 65 ^{o}C. The liposomes suspension was extruded through 200 nm pore sized polycarbonate membranes using an mini extruder (Avanti) at 65 ^{o}C. The hydrodynamic size of liposomes were measured in ISO-TRIS by dynamic light scattering (DLS) on a Zetasizer (Malvern). The mean hydrodynamic diameter of the liposomes was 106 $\pm$ 9 (PDI: 0.25 $\pm$ 0.04). The lipid concentration of liposomes were measured using ICP-MS (Thermo Scintific, iCAP Q) by diluting liposomes 5000- fold with 2% nitric acid solution and 10 ppb of Gallium was added as internal standard. The liposomes were diluted with ISO-TRIS to a final concentration of 5 mM as release medium.

The released concentration of Titanium (Ti) in the new SaTiD were measured by ICP-MS (Thermo Scintific, iCAP Q). Release samples were diluted 10-fold with 2% nitric acid solution and 3 ppb of gadolinium was added as internal standard. The remaining formulation with new SaTiD in the formulation after 30 days was measured by UV-vis (Nanodrop 2000, ThermoFisher).

4.8.2 Synthesis of SaTiDv1 and SaTiDv2

Both Ti complex were synthesized by Senior Researcher Fedor Zhuravlev from Center for Nuclear Technologies at the Technical University of Denmark. SaTiDv1 was synthesized as the same method described in the literature [198]. The NMR properties (^{1}H, ^{13}C) were in full agreement with the reported data. Due to the patent issue, the synthesis of SaTiDv2 could not be described here.

4.8.3 Cell toxicity of SaTiDv1 and SaTiDv2

The cell toxicity of two Ti complex was investigated in the murine CT26 colon carcinoma line. CT26 cells were cultured in DMEM medium supplemented with 10% fetal calf serum and pen-strep at 37 ^{o}C and 5 % CO_2 in a humidified atmosphere. The cellular toxicity of two Ti complex was evaluated by an MTS assay (Promega, CellTiter 96® AQ_{ueous}One Solution Cell Proliferation Assay). CT26 cells were seeded onto 96 well plates at a density of 5000 cells/well one day before adding the solution containing Ti complex. A stock solution of SaTiDv1 or SaTiDv2 in DMSO was prepared (5 mM). A start concentration of 100 µM containing each Ti complex was prepared by diluting the stock solution

50-fold with DMEM medium. Then varying amount of culture medium for CT26 cells was replaced by the Ti complex solution (100 μM, DMEM medium with 2% v/v DMSO) in order to achieve different concentration of Ti complex in each well (0 – 100 μM for each Ti complex). The cells with different amount of Ti complex were incubated for 72 h, then the medium was removed and the cells were incubated in MTS solution. The absorbance was read at 490 nm using a microplate reader (Sunrise, Tacan, USA). Dose-response curves were constructed and the IC_{50} values were calculated from the dose-response curves using GraphPad Prism 7.04.

4.8.4 Preparation of the *in situ*-depot formulation containing SaTiDv2 for *in vitro* release study

SAIB was heated at 70ºC then the liquid-like SAIB could be taken by syringe without needles. LOIB is a powder-like material and could be taken by plastic spatulas. SAIB or LOIB (60 – 80% w/w) was mixed with GTO (40 – 20% w/w) and the resulting mixtures were sonicated for 30 minutes to obtain transparent and homogenous viscous solutions.

A stock solution of SaTiDv2 in DMSO (dimethyl sulfoxide), PC (propylene carbonate) or BA (benzyl alcohol) (8 mg/mL). Then 50 μL of stock solution was added to 450 μL of the viscous solution of SAIB or LOIB with GTO. The resulting mixtures were mixing by sonicating for 30 minutes and vortexing for 1 minute to obtain a homogenous formulation. The concentration of SaTiDv2 in the final depot formulation was about 0.08% w/w.

4.8.4 *In vitro* release of the *in situ*-forming depot formulation containing SaTiDv2

A 100 μL depot formulation containing SaTiDv2 was injected through a 25G needle into 4 mL of ISO-TRIS with stealth liposomes (lipid concentration: 5 mM). The liposomes were added as a sink condition mimic. All the samples were incubated at 37ºC. Aliquots (250 μL) were removed at 2 h and 5 h, and replaced with an equal amount of release medium. Aliquots (250 μL) were removed at 1, 4, 7, 11, 14, 18, 22, 26 and 30 days, and 1 mL of the medium changed with fresh release medium every time. The concentration of Ti element in each aliquot was measured by ICP-MS with a Ti standard curve in the range of 1.25 – 20 ppb. After 30 days, 3.5 mL of release medium was removed and 2 mL of ethanol was added to dissolve the remaining depot formulation. The concentration of

SaTiDv2 in ethanol was analyzed by measuring absorbance using UV-vis at wavelength of 326 nm with a standard curve of new SaTiD in ethanol in the range of 0.0025 – 0.04 mg/mL ($r^2 > 0.999$).

4.8.9 Preparation of the *in situ*-depot formulation containing SaTiDv2 for *in vivo* efficacy study

SAIB was heated at 70°C and poured into a glass vial. 0.7 g SAIB and 0.3 g GTO was mixed by sonicating for 30 minutes to obtain a homogeneous viscous solution. 16 mg SaTiDv2 was dissolved in 1 mL PC. 50 µL of this solution was added to 450 µL of the viscous solution of SAIB with GTO. The resulting mixtures were mixing by sonicating for 30 minutes and vortexing for 1 minute to obtain a homogenous formulation. The concentration of SaTiDv2 in the final depot formulation was about 0.16% w/w.

4.8.9 *In vivo* efficacy study of the *in situ*-forming depot formulation with SaTiDv2

The Danish Animal Welfare Council under the Danish Ministry of Justice approved all experimental procedures conducted during these studies. 7-9 weeks-old female Balb/c mice were obtained from Charles River and were given one week of adaption upon arrival. The CT26 mouse colon carcinoma cell line was obtained from ATCC and maintained in RPMI-1640 supplemented with 10% fetal calf serum (Life Technologies, Thermo Fisher) and 1% penicillin-streptomycin (Almeco).

CT26 syngeneic tumors were established by subcutaneous injection on the flank by 3x105 cells in 100 µl RPMI. Tumors were allowed to grow until they reached an average size of 116 mm^3 (11 days after inoculation), before the mice were randomized into two groups based on a size-dependent randomization (n = 8 per group). Subsequently, one group was left untreated while the other group was intratumoral injected with 50 µL depot formulation (SaTiDv2 concentration 1.6 µg/µL). During treatment, the mice were anesthetized by inhalation anesthesia (~4.5% sevoflurane). Tumor growth progression was monitored by external caliper measurements two to three times a week and the volume was calculated as (length x width2)/2. Mice were terminated from the study, once their tumors reached a volume of ≥1000 mm^3 or if extensive abrasions were observed on the skin surrounding the tumor. The weight of the mice was monitored to ensure that no weight loss beyond 15% was observed.

4.8.10 Supplementary information – Preliminary *in vitro* release of SaTiDv2 from formulation containing LAP (lactose acetate: propionate 1:1 w/w), GTO and DMSO

LAP was first prepared by mixing 200 mg lactose octaacetate with 200 mg lactose octapropionate in a glass vial. Then 25 mg of GTO was added into the glass vial of LAP. 4 mg new SaTiD was dissolved by 1 mL DMSO and 75 mg of this solution was added into the glass vial of LAP with GTO. The final mixture of LAP, GTO and drug DMSO solution was sonicated for 30 min and followed by 1 min vortexing to obtain a homogenous formulation (LAP:GTO:DMSO 80:5:15) with 0.06% w/w SaTiDv2.

A 100 μL depot formulation containing SaTiDv2 was injected through a 25G needle into 4 mL of ISO-TRIS with stealth liposomes (lipid concentration: 5 mM). All the samples were incubated at 37 ^{o}C. Aliquots (250 μL) were removed at 1, 3 and 5 h, and replaced with an equal amount of release medium. Aliquots (250 μL) were removed at 1, 4 and 7 days, and 1 mL of the medium changed with fresh release medium every time. The concentration of Ti element in each aliquot was measured by ICP-MS with a Ti standard curve in the range of 1.25 – 20 ppb. After 7 days, 3.5 mL of release medium was removed and 1.5 mL of ethanol was added to dissolve the remaining depot formulation. The concentration of SaTiDv2 in ethanol was analyzed by measuring absorbance using UV-vis at wavelength of 326 nm with a standard curve of SaTiDv2 in the range of 0.0025 – 0.04 mg/mL (r^2 > 0.999).

Chapter 5. Concluding remarks and perspectives

At present, the commonly applied clinical treatment modalities for cancer are chemotherapy, surgery and radiation therapy. However, each modality has its own limitations. Novel biodegradable materials for intratumoral administration such as liposomes, micelles and *in-situ* forming systems are considered as powerful weapons in the fight against cancer. Therefore, the aim of this thesis was to develop these novel materials to deliver anti-cancer compounds or imaging contrast agents in order to improve the current cancer treatments.

Currently, the development of novel markers for surgical guidance is the crucial challenge in the improvement of surgery. The ideal marker should allow for image guidance during implantation (i.e. CT, NMR, ultrasound images), be visible on planning images (i.e. CT, NMR, PET images), and can be accurately localized by palpation, gamma detection, NIR imaging, etc. Moreover, the ideal marker should be biocompatible and reduce the discomfort of patients during the procedure. However, none of the currently available markers fulfil all of these criteria. Here, we have reported an injectable multimodal fiducial marker that is visible in CT, ultrasound, PET, gamma detection and NIR images for surgical guidance. The marker contains a fluorophore, PC, which have similar fluorescence emission properties as ICG. PC was found to be stably retained in the marker, and it could chelate radionuclide such as $^{64}Cu^{2+}$ for PET imaging and gamma detection. Our *in vivo* evaluation of the marker in mice model showed the marker was clearly by PET and CT images for at least 48 hours with radioactivity of 1.75 MBq at the time of injection, and NIR images for at least 4 weeks. Moreover, the radionuclide and fluorophore were well retained in the marker, which lower the risk of healthy tissue damage caused by radiation or toxicity of the fluorophore. The long-term visibility of the marker will provide surgeons enough time for planning and performing the surgical procedure. In comparison to some systemic tumor-targeted novel delivery systems such as liposomes or antibody modified contrast agents, the intratumoral injection of a surgical marker can provide higher tumor-to-blood ratio. However, the marker might not be fully compatible to the clinical NIR camera systems to detect ICG or MB. Therefore, a solution for this issue could be 1) develop new NIR camera system that can detect the marker, 2) change to other phthalocyanine fluorophores that have the similar emission spectra of ICG or MB, or 3) change to other fluorophores that have the similar emission spectra of ICG or MB and chelate radionuclide by some hydrophobic compounds such as ionophores. In summary, the injectable multimodal fiducial marker is promising for future clinical surgical procedures to remove pulmonary nodules or lymph node in head, neck or breast.

In the clinical brachytherapy, the main limitations are the invasive procedures due to the implantation of the metal seeds and the heterogeneous dose distribution in the tumor region. To overcome these issues, we have designed and synthesized two novel non-toxic DOTA-triarginine-lipid conjugates, D3R-C16 and D3R-C18 for controlled delivery of radionuclides to tumors. The compounds were designed to diffuse in the tumor region and partition to the cell membrane. The *in vivo* results showed the D3R-C18 had a fast intratumoral distribution and a high degree of retention up to 6 h. The liposomal formulation with D3R-C18 showed a slower distribution within the tumor than the free compound but longer retention up to 24 h. Our results indicated that both formulations have promising potential in brachytherapy to deliver short-lived and short-ranged therapeutic radionuclides, such as alpha emitters (Bi-213) and Auger emitters (Rh-103m). Moreover, the liposome formulation might also be promising to deliver long ranged beta minus emitters such as Cu-64. Alpha and auger emitters are seldom discuss in previous research studies in brachytherapy because the design of the systems to deliver these emitters is challenging. The distribution of these emitters in the tumor should be fast due to their short range and the retention time in the tumor should be long enough to avoid the radiation to other health tissues. As a small molecule, D3R-C18 can diffuse through the tumor interstitium, resulting in a faster distribution than nanoparticles such as liposomes and gold particles. Moreover, a long tumor retention was achieved by the partitioning into cell membranes. In future studies, *in vivo* efficacy of the formulation containing therapeutic radionuclides should be evaluated. Radionuclides with different energy and half-lives should also be compared. The ideal clinical result should be complete elimination of the tumor by single or several injections of the formulation.

In current chemotherapy, most of the drug are delivered by systemic administration. However, systemic administration of the drug causes insufficient dose in the tumor and several side effect in the healthy tissues. In order to improve the current chemotherapy, we have developed *in situ*-forming depot formulations for intratumoral injection that can deliver a new generation Ti-complex chemotherapeutic drug, SaTiDv2, to the tumor. A highly cytotoxic compound SaTiDv2 with a 4-fold lower IC_{50} than the previous reported SaTiDv1 was synthesized by chemical modification. Then SaTiDv2 was loaded into depot formulations based on carbohydrate esters (SAIB or LOIB) with GTO and organic solvent (DMSO, propylene carbonate or benzyl alcohol). The *in vitro* release profile of SaTiDv2 could be modified by types of carbohydrate ester, amount of GTO and the types of organic solvent used in the formulation. The optimal formulation that gave the highest cumulative release in 30 days and a low burst release was SAIB:GTO:PC 63:27:10 w/w. The formulation loaded with SaTiDv2 was investigated *in vivo* in tumor-bearing mice. The *in vivo* results indicated the

locoregional formulation had the potential to suppress the tumor growth. However, the tumor could not be completely eliminated by the single injection of the formulation. The incomplete elimination of the tumor might due to the low cumulative release of the drug from the formulation and the plateau of release reached early on Day 11. Therefore, multiple injections of the formulation such as one injection every two weeks could be considered for future investigation or clinical suggestion. Moreover, hydrophilic carbohydrate esters such as the mixture of lactose acetate and lactose propionate that have low interaction with the hydrophobic drug could be better materials than SAIB and LOIB. Ti-45 is a desirable PET radionuclide, therefore, PET imaging could be utilized to monitor the retention of the Ti-45 radiolabeled drug in tumor and other health tissues for future study. These results could be valuable for the *in vivo* toxicity evaluation for both preclinical and clinical evaluation.

Generally, novel biodegradable materials such as micelles, liposomes and *in situ*-forming depot formulations are promising to improve the clinical cancer treatment methods including chemotherapy, surgery and brachytherapy.

Reference

[1] World Health Oranization, "Latest world cancer statistics," *Int. Agency Res. Cancer, World Heal. Organ.*, no. December, pp. 2012–2014, 2013.

[2] S. Tsim, C. A. O'Dowd, R. Milroy, and S. Davidson, "Staging of non-small cell lung cancer (NSCLC): A review," *Respir. Med.*, vol. 104, no. 12, pp. 1767–1774, 2010.

[3] M. W. G. Jesse B.Wolinsky, Yolonda L.Colson, "Local drug delivery strategies for cancer treatment: gels, nanoparticles, polymeric films, rods, and wafers," *J Control Release*, vol. 159, no. 1, pp. 1–34, 2012.

[4] M. Arruebo *et al.*, "Assessment of the evolution of cancer treatment therapies," *Cancers (Basel).*, vol. 3, no. 3, pp. 3279–3330, 2011.

[5] Y. Brudno and D. J. Mooney, "On-demand drug delivery from local depots," *J. Control. Release*, vol. 219, pp. 8–17, 2015.

[6] J. Amir Fakhari and A. Subramony, "Engineered in-situ depot-forming hydrogels for intratumoral drug delivery," *J. Control. Release J.*, vol. 220, pp. 465–475, 2015.

[7] H. Maeda, "Macromolecular therapeutics in cancer treatment: The EPR effect and beyond," *J. Control. Release*, vol. 164, no. 2, pp. 138–144, 2012.

[8] A. F. Frellsen *et al.*, "Mouse positron emission tomography study of the biodistribution of gold nanoparticles," 2016.

[9] A. I. Jensen *et al.*, "Remote-loading of liposomes with manganese-52 and in vivo evaluation of the stabilities of52Mn-DOTA and64Cu-DOTA using radiolabelled liposomes and PET imaging," *J. Control. Release*, vol. 269, no. July 2017, pp. 100–109, 2018.

[10] J. E. Gains *et al.*, "177Lu-DOTATATE molecular radiotherapy for childhood neuroblastoma," *J. Nucl. Med.*, vol. 52, no. 7, pp. 1041–1047, 2011.

[11] G. P. Nicolas *et al.*, "Biodistribution, pharmacokinetics, and dosimetry of ^{177}Lu-, ^{90}Y-, and ^{111}In-labeled somatostatin receptor antagonist OPS201 in comparison to the agonist ^{177}Lu-DOTATATE: The mass effect," *J. Nucl. Med.*, vol. 58, no. 9, pp. 1435–1441, 2017.

[12] B. L. R. Kam *et al.*, "Lutetium-labelled peptides for therapy of neuroendocrine tumours,"

Eur. J. Nucl. Med. Mol. Imaging, vol. 39, no. SUPPL.1, 2012.

[13] J. Skowronek, "Low-dose-rate or high-dose-rate brachytherapy in treatment of prostate cancer - Between options," *J. Contemp. Brachytherapy*, vol. 5, no. 1, pp. 33–41, 2013.

[14] S. K. Sahoo and V. Labhasetwar, "Nanotech approaches to drug delivery and imaging," *Drug Discov. Today*, vol. 8, no. 24, pp. 1112–1120, 2003.

[15] A. Akbarzadeh, R. Rezaei-sadabady, S. Davaran, S. W. Joo, and N. Zarghami, "Liposome : classification , preparation , and applications," *Nanoscale Res. Lett.*, vol. 8, no. 1, p. 1, 2013.

[16] A. T. I. Jensen, P. Rasmussen, and T. L. Andresen, "Radiolabeling of liposomes and polymeric micelles with PET-isotopes," *Tech. Univ. Denmark*, 2012.

[17] N. M. Rao, "Cationic lipid-mediated nucleic acid delivery: beyond being cationic," *Chem. Phys. Lipids*, vol. 163, no. 3, pp. 245–252, 2010.

[18] R. A. Demel and B.DE. Kruyff, "The function of sterols in membranes," *Biochim. Biophys. Acta (BBA)-Reviews Biomembr.*, vol. 457, no. 2, pp. 109–132, 1976.

[19] M. L. Briuglia, C. Rotella, A. McFarlane, and D. A. Lamprou, "Influence of cholesterol on liposome stability and on in vitro drug release," *Drug Deliv. Transl. Res.*, vol. 5, no. 3, pp. 231–242, 2015.

[20] T. M. Allen, C. Hansen, F. Martin, C. Redemann, and A. Yau-Young, "Liposomes containing synthetic lipid derivatives of poly(ethylene glycol) show prolonged circulation half-lives in vivo," *BBA - Biomembr.*, vol. 1066, no. 1, pp. 29–36, 1991.

[21] K. J. Harrington, G. Rowlinson-busza, K. N. Syrigos, P. S. Uster, R. G. Vile, and J. S. W. Stewart, "Pegylated liposomes have potential as vehicles for intratumoral and subcutaneous drug delivery," vol. 6, no. June, pp. 2528–2537, 2000.

[22] Kacoli Banerjee, Shubhadeep Banerjee, and Mahitosh Mandal, "Liposomes as a drug delivery system," in *Biological and Pharmaceutical Applications of Nanomaterials*, vol. Chapter 3, 2015, pp. 53–100.

[23] Y. Barenholzt, S. Amselem, and L. D., "A new method for preparation of phospholipid vesicles (liposomes) - french press," *FEBS Lett.*, vol. 99, no. 1, pp. 210–214, 1979.

[24] Y. Barenholz, "Doxil® - The first FDA-approved nano-drug: Lessons learned," *J. Control.*

Release, vol. 160, no. 2, pp. 117–134, 2012.

[25] B. Goins, W. T. Phillips, A. Bao, M. Code, S. Antonio, and C. W. Reserve, "Strategies for improving the intratumoral distribution of liposomal drugs in cancer therapy," *Expert Opin Drug Deliv*, vol. 13, no. 6, pp. 873–889, 2016.

[26] A. Bao *et al.*, "Potential use of drug carried-liposomes for cancer therapy via direct intratumoral injection," *Int. J. Pharm.*, vol. 316, pp. 162–169, 2006.

[27] A. A. Gorfe, R. Baron, and J. A. McCammon, "Water-membrane partition thermodynamics of an amphiphilic lipopeptide: An enthalpy-driven hydrophobic effect," *Biophys. J.*, vol. 95, no. 7, pp. 3269–3277, 2008.

[28] C. Oerlemans, W. Bult, M. Bos, G. Storm, J. F. W. Nijsen, and W. E. Hennink, "Polymeric micelles in anticancer therapy: Targeting, imaging and triggered release," *Pharm. Res.*, vol. 27, no. 12, pp. 2569–2589, 2010.

[29] V. P. Torchilin, "Micellar nanocarriers: Pharmaceutical perspectives," *Pharm. Res.*, vol. 24, no. 1, pp. 1–16, 2007.

[30] A. V Kabanov, E. V Batrakova, and V. Yu, "Pluronic ® block copolymers as novel polymer therapeutics for drug and gene delivery," *J. Control. Release*, vol. 82, pp. 189–212, 2002.

[31] G. Adams, ML; Lavasanifar, A; Kwon, "Amphiphilic block copolymers for drug delivery," *J. Pharm. Sci.*, vol. 92, no. 7, pp. 1343–1355, 2003.

[32] J. L. Schaal *et al.*, "Injectable polypeptide micelles that form radiation crosslinked hydrogels in situ for intratumoral radiotherapy," *J. Control. Release*, vol. 228, pp. 58–66, 2016.

[33] M. Xu *et al.*, "Evaluation of micelles incorporated into thermosensitive hydrogels for intratumoral delivery and controlled release of docetaxel: A dual approach for in situ treatment of tumors," *Asian J. Pharm. Sci.*, vol. 13, no. 4, pp. 373–382, 2018.

[34] X. Liu, W. S. Heng, Paul, Q. Li, and L. W. Chan, "Novel polymeric microspheres containing norcantharidin for chemoembolization," *J. Control. Release*, vol. 116, no. 1, pp. 35–41, 2006.

[35] D. E. Gerber, G. L. Gallia, B. M. Tyler, C. G. Eberhart, G. Royer, and S. A. Grossman, "A novel polymer gel for the delivery of local therapies to intracranial tumors: In vivo safety

evaluation," *J. Biomed. Mater. Res. - Part A*, vol. 99 A, no. 3, pp. 479–484, 2011.

[36] Li Xingyi, Kong Xiangye, Zhang Juan, Wang Yingjing, Wang Yujun, Shi Shuai, Guo Gang, Luo Feng, Zhao Xia, Wei Yuquan, Qian Zhiyong, "A Novel Composite Hydrogel Based on Chitosan and Inorganic Phosphate for Local Drug Delivery of Camptothecin Nanocolloids," *J. Pharm. Sci.*, vol. 100, no. 1, pp. 232–241, 2011.

[37] B. S. Davidson, F. Izzo, D. M. Cromeens, L. C. Stephens, Z. H. Siddik, and S. A. Curley, "Collagen matrix cisplatin prevents local tumor growth after margin-positive resection," *Journal of Surgical Research*, vol. 58, no. 6. pp. 618–624, 1995.

[38] M. Sowjanya, S. Debnath, P. Lavanya, R. Thejovathi, and M. N. Babu, "Polymers used in the Designing of Controlled Drug Delivery System," *Res. J. Pharm. Technol.*, vol. 10, no. 3, p. 903, 2017.

[39] X. Lin, S. Yang, J. Guo, M. Zhao, Y. Zhang, N. Qi, H. He, C. Cai, X. Tang, P. Guo, "A novel risperidone-loaded SAIB-PLGA mixture matrix depot with a reduced burst release: Effects of solvents and PLGA on drug release behaviors in vitro/in vivo," *J. Mater. Sci. Mater. Med.*, vol. 23, no. 2, pp. 443–455, 2012.

[40] R. I. Jølck, T Binderup, A. E. Hansen, J. B Scherman, P. M. Rosenschold, A. Kjær, T. L. Andresen, "Injectable colloidal gold in a sucrose acetate isobutyrate gelating matrix with potential use in radiation therapy," *Adv. Healthc. Mater.*, vol. 3, pp. 1680–1687, 2014.

[41] Y. Lu, Y. Yu, X. Tang, "Sucrose acetate isobutyrate as an in situ forming system for sustained risperidone release," *J. Phar*, vol. 96, pp. 3252–3262, 2007.

[42] C. B. Packhaeuser, J. Schnieders, C. G. Oster, and T. Kissel, "In situ forming parenteral drug delivery systems: An overview," *Eur. J. Pharm. Biopharm.*, vol. 58, no. 2, pp. 445–455, 2004.

[43] F. W. Okumu *et al.*, "Sustained delivery of human growth hormone from a novel gel system: SABER™," *Biomaterials*, vol. 23, no. 22, pp. 4353–4358, 2002.

[44] S. Pechenov, B. Shenoy, M. X. Yang, S. K. Basu, and A. L. Margolin, "Injectable controlled release formulations incorporating protein crystals," *J. Control. Release*, vol. 96, no. 1, pp. 149–158, 2004.

[45] J. S. Rydhög *et al.*, "Liquid fiducial marker performance during radiotherapy of locally advanced non small cell lung cancer," *Radiother. Oncol.*, vol. 121, no. 1, pp. 64–69, 2016.

[46] H. Schaarup-Jensen *et al.*, "Injectable iodine-125 labeled tissue marker for radioactive localization of non-palpable breast lesions," *Acta Biomater.*, vol. 65, pp. 197–202, 2018.

[47] M. L. James and S. S. Gambhir, "A molecular imaging primer: modalities, imaging agents, and applications," *Physiol. Rev.*, vol. 92, no. 2, pp. 897–965, 2012.

[48] B. J. Hillman, "Introduction to the special issue on medical imaging in oncology," *J. Clin. Oncol.*, vol. 24, no. 20, pp. 3223–3224, 2006.

[49] S. N. Histed, M. L. Lindenberg, E. Mena, B. Turkbey, P. L. Choyke, and K. A. Kurdziel, "Review of functional/ anatomic imaging in oncology," *Nucl Med Commun*, vol. 33, no. 4, pp. 349–361, 2012.

[50] N. Lee, S. H. Choi, and T. Hyeon, "Nano-sized CT contrast agents," *Adv. Mater.*, vol. 25, no. 19, pp. 2641–2660, 2013.

[51] H. Lusic and M. W. Grinstaff, "X-Ray Computed tomography contrast agents," *Chem. Rev.*, vol. 113, no. 3, pp. 1641–1666, 2014.

[52] Y. Xing, J. Zhao, P. S. Conti, and K. Chen, "Radiolabeled nanoparticles for multimodality tumor imaging," *Theranostics*, vol. 4, no. 3, pp. 290–306, 2014.

[53] S. B. Yu and A. D. Watson, "Metal-based X-ray contrast media," *Chem. Rev.*, vol. 99, no. 9, pp. 2353–2377, 1999.

[54] A. A. Enquobahrie, A. P. Reeves, D. F. Yankelevitz, and C. I. Henschke, "Automated detection of small pulmonary nodules in whole lung CT scans," *Acad. Radiol.*, vol. 14, no. 5, pp. 579–593, 2007.

[55] F.-M. Lu and Z. Yuan, "PET/SPECT molecular imaging in clinical neuroscience: recent advances in the investigation of CNS diseases," *Quant. Imaging Med. Surg.*, vol. 5, no. 3, pp. 433–447, 2015.

[56] S. S. Gambhir, "Molecular imaging of cancer with positron emission tomography," *Nat. Rev. Cancer*, vol. 2, no. 9, pp. 683–693, 2002.

[57] D. L. Bailey and K. P. Willowson, "An evidence-based review of quantitative SPECT

imaging and potential clinical applications," *J. Nucl. Med.*, vol. 54, no. 1, pp. 83–89, 2013.

[58] V. D. Awasthi, B. Goins, R. Klipper, and W. T. Phillips, "Dual radiolabeled liposomes: Biodistribution studies and localization of focal sites of infection in rats," *Nucl. Med. Biol.*, vol. 25, no. 2, pp. 155–160, 1998.

[59] S. P. Butler, D. L.Bailey, A. F.McLaughlin, F. A.Khafag, and F. 0. Stephens, "SPECTEvaluationof ArterialPerfusion in Regional Chemotherapy," *jounal Nucl. Med. Nucl. Med.*, vol. 29, no. 5, pp. 593–598, 1988.

[60] M. M.V., M. S.A., K. E.E., and M. H.A., "Evaluation and localization of lymphatic drainage and sentinel lymph nodes in patients with head and neck melanomas by hybrid SPECT/CT lymphoscintigraphic imaging," *J. Nucl. Med. Technol.*, vol. 35, no. 1, pp. 10–16, 2007.

[61] E. Even-Sapir *et al.*, "Lymphoscintigraphy for sentinel node mapping using a hybrid SPECT/CT system.," *J. Nucl. Med.*, vol. 44, no. 9, pp. 1413–1420, 2003.

[62] M. E. Phelps, "Positron emission tomography provides molecular imaging of biological processes," *Proc. Natl. Acad. Sci.*, vol. 97, no. 16, pp. 9226–9233, 2000.

[63] L. Fass, "Imaging and cancer: A review," *Mol. Oncol.*, vol. 2, no. 2, pp. 115–152, 2008.

[64] M. E. Juweid and B. D. Cheson, "Positron-emission tomography and assessment of cancer therapy," *N. Engl. J. Med.*, vol. 354, no. 5, pp. 496–507, 2006.

[65] M. C. A. Van Kouwen, W. J. G. Oyen, F. M. Nagengast, J. B. M. J. Jansen, and J. P. H. Drenth, "FDG-PET scanning in the diagnosis of gastrointestinal cancers," *Scand. J. Gastroenterol.*, vol. 39, no. 241, pp. 85–92, 2004.

[66] A. Zhu, D. Lee, and H. Shim, "Metabolic PET imaging in cancer detection and therapy response," *Semin Oncol.*, vol. 38, no. 1, pp. 55–69, 2011.

[67] G. Engudar *et al.*, "Remote loading of liposomes with a 124I-radioiodinated compound and their in vivo evaluation by PET / CT in a murine tumor model," *Theranostics*, vol. 8, no. 21, pp. 5828–5841, 2018.

[68] Y. Zhang, H. Hong, and W. Cai, "PET tracers based on zirconium-89," *Curr. Radiopharm.*, vol. 4, no. 2, pp. 131–139, 2011.

[69] N. Kosaka, M. Ogawa, P. L. Choyke, and H. Kobayashi, "Clinical implications of near-

infrared fluorescence imaging in cancer," *Futur. Oncol.*, vol. 5, no. 9, pp. 1501–1511, 2009.

[70] R. Weissleder and M. J. Pittet, "Imaging in the era of molecular oncology," *Nature*, vol. 452, no. 7187, pp. 580–589, 2008.

[71] G. Hong, A. L. Antaris, and H. Dai, "Near-infrared fluorophores for biomedical imaging," *Nat. Biomed. Eng.*, vol. 1, no. 1, pp. 1–22, 2017.

[72] G. E. Moore, W. T. Peyton, L. A. French, and W. W. Walker, "The clinical use of fluorescein in neurosurgery, The localization of brain tumors," *J. Neurosurg.*, vol. 5, no. 4, pp. 392–398, 1948.

[73] D. Jaque *et al.*, "Nanoparticles for photothermal therapies," *Nanoscale*, vol. 6, no. 16, pp. 9494–9530, 2014.

[74] S. Zhu, B. C. Yung, S. Chandra, G. Niu, A. L. Antaris, and X. Chen, "Near-Infrared-II (NIR-II) bioimaging via Off-Peak NIR-I fluorescence emission," *Theranostics*, vol. 8, no. 15, pp. 4141–4151, 2018.

[75] S. L. Troyan *et al.*, "The FLARE intraoperative Near-Infrared fluorescence imaging system: A first-in-human clinical trial in breast cancer snetienl lymp node mapping," *Ann. Surg. Oncol.*, vol. 16, no. 10, pp. 2943–2952, 2009.

[76] G. Themelis, J. S. Yoo, K. Soh, R. B. Schulz, and V. Ntziachristos, "Real-time intraoperative fluorescence imaging system using light-absorption correction.," *J. Biomed. Opt.*, vol. 14, no. 6, p. 64012, 2009.

[77] C.-Y. Huang, D.-T. Ju, C.-F. Chang, P. Muralidhar Reddy, and B. K. Velmurugan, "A review on the effects of current chemotherapy drugs and natural agents in treating non–small cell lung cancer," *BioMedicine*, vol. 7, no. 4, pp. 12–23, 2017.

[78] B. A. Chabner and T. G. Roberts, "Chemotherapy and the war on cancer," *Nat. Rev. Cancer*, vol. 5, no. 1, pp. 65–72, 2005.

[79] R. K. Singh, S. Kumar, D. N. Prasad, and T. R. Bhardwaj, "Therapeutic journery of nitrogen mustard as alkylating anticancer agents: Historic to future perspectives," *Eur. J. Med. Chem.*, vol. 151, pp. 401–433, 2018.

[80] D. Hanahan and R. A. Weinberg, "The hallmarks of cancer," *Cell*, vol. 100, pp. 57–70, 2000.

[81] S. Lv *et al.*, "Co-delivery of doxorubicin and paclitaxel by PEG-polypeptide nanovehicle for the treatment of non-small cell lung cancer," *Biomaterials*, vol. 35, no. 23, pp. 6118–6129, 2014.

[82] H. Wang *et al.*, "Enhanced anti-tumor efficacy by co-delivery of doxorubicin and paclitaxel with amphiphilic methoxy PEG-PLGA copolymer nanoparticles," *Biomaterials*, vol. 32, no. 32, pp. 8281–8290, 2011.

[83] M. Li *et al.*, "Cisplatin crosslinked pH-sensitive nanoparticles for efficient delivery of doxorubicin," *Biomaterials*, vol. 35, no. 12, pp. 3851–3864, 2014.

[84] S. Barui, S. Saha, G. Mondal, S. Haseena, and A. Chaudhuri, "Simultaneous delivery of doxorubicin and curcumin encapsulated in liposomes of pegylated RGDK-lipopeptide to tumor vasculature," *Biomaterials*, vol. 35, no. 5, pp. 1643–1656, 2014.

[85] N. Iqbal and N. Iqbal, "Imatinib: A breakthrough of targeted therapy in cancer," *Chemother. Res. Pract.*, vol. 2014, pp. 1–9, 2014.

[86] H. Nückel, U. H. Frey, A. Röth, U. Dührsen, and W. Siffert, "Alemtuzumab induces enhanced apoptosis in vitro in B-cells from patients with chronic lymphocytic leukemia by antibody-dependent cellular cytotoxicity," *Eur. J. Pharmacol.*, vol. 514, no. 2–3, pp. 217–224, 2005.

[87] American Cancer Society, "https://www.cancer.org/treatment/treatments-and-side-effects/treatment-types/radiation/basics.html." Link assessed 30.1 2019.

[88] R. Baskar, K. A. Lee, R. Yeo, and K. W. Yeoh, "Cancer and radiation therapy: Current advances and future directions," *Int. J. Med. Sci.*, vol. 9, no. 3, pp. 193–199, 2012.

[89] S. P. Jackson and J. Bartek, "The DNA-damage response in human biology and disease," *Nature*, vol. 461, no. 7267, pp. 1071–1078, 2009.

[90] J. Bosch-Barrera, B. Queralt, and J. A. Menendez, "Targeting STAT3 with silibinin to improve cancer therapeutics," *Cancer Treat. Rev.*, vol. 58, pp. 61–69, 2017.

[91] S. Gianfaldoni, R. Gianfaldoni, U. Wollina, J. Lotti, G. Tchernev, and T. Lotti, "An overview on radiotherapy: From its history to its current applications in dermatology," *Open Access Maced. J. Med. Sci.*, vol. 5, no. 4, p. 521, 2017.

[92] J. Thariat, J. M. Hannoun-Levi, A. Sun Myint, T. Vuong, and J. P. Gérard, “Past, present, and future of radiotherapy for the benefit of patients,” *Nat. Rev. Clin. Oncol.*, vol. 10, no. 1, pp. 52–60, 2013.

[93] D. W. Fry, R. B. R.-S.-Harvie, L. B. Mullett, and W. Walkinshaw, “A travelling-wave linear accelerator for 4-MEV electrons,” *Nature*, vol. 162, no. 4126, pp. 859–861, 1948.

[94] R. Mohan, “Field shaping for three-dimensional conformal radiation therapy and multileaf collimation,” *Semin. Radiat. Oncol.*, vol. 5, no. 2, pp. 86–99, 1995.

[95] C. S. Chui, M. F. Chan, E. Yorke, S. Spirou, and C. C. Ling, “Delivery of intensity-modulated radiation therapy with a conventional multileaf collimator: Comparison of dynamic and segmental methods,” *Med. Phys.*, vol. 28, no. 12, pp. 2441–2449, 2001.

[96] E. Bakiu, E. Telhaj, E. Kozma, F. Rųi, and P. Malkaj, “Comparison of 3D CRT and IMRT tratment plans,” *Acta Inform. Medica*, vol. 21, no. 3, pp. 211–212, 2013.

[97] P. Giraud, E. Yorke, S. Jiang, L. Simon, K. Rosenzweig, and G. Mageras, “Reduction of organ motion effects in IMRT and conformal 3D radiation delivery by using gating and tracking techniques,” *Cancer/Radiotherapie*, vol. 10, no. 5, pp. 269–282, 2006.

[98] L. A. Dawson and M. B. Sharpe, “Image-guided radiotherapy ationale, benefits, and.pdf,” *Lancet Oncol.*, vol. 7, pp. 848–858, 2006.

[99] M. N. Duma, S. Kampfer, J. J. Wilkens, T. Schuster, M. Molls, and H. Geinitz, “Comparative analysis of an image-guided versus a non-image-guided setup approach in terms of delivered dose to the parotid glands in head-and-neck cancer IMRT,” *Int. J. Radiat. Oncol. Biol. Phys.*, vol. 77, no. 4, pp. 1266–1273, 2010.

[100] B. M. Barney, R. J. Lee, D. Handrahan, K. T.Welsh, T. Cook, and W. T. Sause, “Image-guided radiotherapy (IGRT) for prostate cancer comparing kV imaging of fiducial markers with cone beam computed tomography (CBCT),” *Int. J. Radiat. Oncol. Biol. Phys.*, vol. 80, no. 1, pp. 301–305, 2011.

[101] M. R. Moman *et al.*, “Long-term experience with transrectal and transperineal implantations of fiducial gold markers in the prostate for position verification in external beam radiotherapy; feasibility, toxicity and quality of life,” *Radiother. Oncol.*, vol. 96, no. 1, pp. 38–42, 2010.

[102] Reflexion, “https://www.reflexion.com/.” Link assessed 30.1 2019.

[103] Q. Fan, A. Nanduri, S. Mazin, and L. Zhu, “Emission guided radiation therapy for lung and prostate cancers: A feasibility study on a digital patient,” *Med. Phys.*, vol. 39, no. 11, pp. 7140–7152, 2012.

[104] Q. Fan *et al.*, “Toward a planning scheme for emission guided radiation therapy (EGRT): FDG based tumor tracking in a metastatic breast cancer patient,” *Med. Phys.*, vol. 40, no. 8, p. 81708, 2013.

[105] J. Yang, T. Yamamoto, S. R. Mazin, E. E. Graves, and P. J. Keall, “The potential of positron emission tomography for intratreatment dynamic lung tumor tracking: A phantom study,” *Med. Phys.*, vol. 41, no. 2, pp. 1–14, 2014.

[106] M. Dahiya, “Brachytherapy: a Review,” *J. Crit. Rev.*, vol. 3, no. 2, pp. 6–10, 2016.

[107] I. C. on R. U. and Measurements, “Dose and volume specification for reporting intracavitary therapy in gynecology,” in *Tech. Rep. 38, International Commission on Radiation Units and Measurements, Bethesda, Md, USA*, 1985.

[108] E. B. Podgorsak, “Radiation oncology physics: A handbook for teachers and students,” *International atomic energy agency, Vienna*. 2005.

[109] A. Chichel, M. Kanikowski, J. Skowronek, M. Dymnicka, and T. Piotrowski, “Correlation between treatment plan parameters and particular prognostic factors in prostate cancer treated with high-dose-rate brachytherapy (HDR-BT) as a boost,” *J Contem Brachyther*, vol. 1, no. 1, pp. 11–17, 2009.

[110] D. J. Demanes, R. R. Rodriguez, and G. A. Altieri, “High dose rate prostate brachytherapy: The California Endocurietherapy (CET) method,” *Radiother. Oncol.*, vol. 57, no. 3, pp. 289–296, 2000.

[111] A. Challapalli, E. Jones, C. Harvey, G. O. Hellawell, and S. A. Mangar, “High dose rate prostate brachytherapy: An overview of the rationale, experience and emerging applications in the treatment of prostate cancer,” *Br. J. Radiol.*, vol. 85, no. SPEC. ISSUE 1, 2012.

[112] J.Schramm, “Advances and Technical Standards in Neurosurgery-Low-Grade Gliomas,” *SpringerWien, New York,* 2010.

[113] H. H. Holm, N. Juul, J. F. Pedersen, H. Hansen, and I. Stroyer, “Transperineal 125iodine seed implantation in prostatic cancer guided by transrectal ultrasonography.,” *J. Urol.*, vol. 167, pp. 985–989, 1983.

[114] Jeffrey F williamson, “Brachytherapy technology and physics practice since 1950: a half-century of progress,” *Phys. Med. Biol.*, vol. 51, pp. R303–R325, 2006.

[115] M. D. Michaelson, S. E. Cotter, P. C. Gargollo, A. L. Zietman, D. M. Dahl, and M. R. Smith, “Management of complications of prostate cancer treatment M.,” *CA. Cancer J. Clin.*, vol. 58, no. 4, pp. 196–213, 2008.

[116] R. A. Older, B. Synder, T. L. Krupski, D. J. Glembocki, and J. Y. Gillenwater, “Radioactive implant migration in patients treated for localized prostate cancer with interstitial brachytherapy.,” *J. Urol.*, vol. 165, no. 5, pp. 1590–1592, 2001.

[117] J. Brumm, “Brachytherapy as a treatment option for prostate cancer :,” *BUMC Proc.*, vol. 13, pp. 227–229, 2000.

[118] W. T. Phillips *et al.*, “Rhenium-186 liposomes as convection- enhanced nanoparticle brachytherapy for treatment of glioblastoma,” *Neuro. Oncol.*, vol. 14, no. 4, pp. 416–425, 2012.

[119] J. T. French *et al.*, “Interventional therapy of head and neck cancer with lipid nanoparticle-carried rhenium-186 radionuclide,” *J. Vasc. Interv. Radiol.*, vol. 21, no. 8, pp. 1271–1279, 2010.

[120] S. X. Wang *et al.*, “Intraoperative186 re-liposome radionuclidetherapy in a head and neck squamous cell carcinoma xenograft positive surgical margin model,” *Clin. Cancer Res.*, vol. 14, no. 12, pp. 3975–3983, 2008.

[121] M. Laprise-Pelletier, Y. Ma, J. Lagueux, M. F. Côté, L. Beaulieu, and M. A. Fortin, “Intratumoral injection of low-energy photon-emitting gold nanoparticles: A microdosimetric monte Carlo-based Model,” *ACS Nano*, vol. 12, no. 3, pp. 2482–2497, 2018.

[122] Y. Kim *et al.*, “Locally targeted delivery of a micron-size radiation therapy source using temperature-sensitive hydrogel Y,” *Int. J. Radiat. Oncol. • Biol. • Phys.*, vol. 88, no. 5, pp. 1142–1147, 2014.

[123] S. B. Mondal, S. Gao, N. Zhu, R. Liang, V. Gruev, and S. Achilefu, "Real-time fluorescence image-guided oncologic surgery," 1st ed., vol. 124. *Elsevier Inc*., 2014.

[124] E. Jolesz, Ferenc A., *"Intraoperative imaging and image-guided therapy," Springer Science & Business Media.,* 2014.

[125] A. L. Vahrmeijer, M. Hutteman, J. R. Van Der Vorst, C. J. H. Van De Velde, and J. V. Frangioni, "Image-guided cancer surgery using near-infrared fluorescence," *Nature Reviews Clinical Oncology*, vol. 10, no. 9. pp. 507–518, 2013.

[126] M. Ahmed, A. D. Purushotham, and M. Douek, "Novel techniques for sentinel lymph node biopsy in breast cancer: A systematic review," *The Lancet Oncology*, vol. 15, no. 8. Elsevier Ltd, pp. e351–e362, 2014.

[127] B. A. in't Hout, K. E. Schenk, A. N. van der Linden, and R. M. H. Roumen, "Efficacy of localization of non-palpable, invasive breast cancer: Wire localization vs. Iodine-125 seed: A historical comparison," *Breast*, vol. 29, pp. 8–13, 2016.

[128] R. J. Gray *et al.*, "Randomized prospective evaluation of a novel technique for biopsy or lumpectomy of nonpalpable breast lesions: Radioactive seed versus wire localization," *Ann. Surg. Oncol.*, vol. 8, no. 9, pp. 711–715, 2001.

[129] R. Gennari *et al.*, "Use of technetium-99m-labeled colloid albumin for preoperative and intraoperative localization of nonpalpable breast lesions," *J. Am. Coll. Surg.*, vol. 190, no. 6, pp. 692–699, 2000.

[130] M. E. M. Van Der Noordaa, K. E. Pengel, and E. Groen, "The use of radioactive iodine-125 seed localization in patients with non-palpable breast cancer : A comparison with the radioguided occult lesion localization with 99m technetium," *Eur. J. Surg. Oncol.*, vol. 41, no. 4, pp. 553–558, 2015.

[131] S. H. Goudreau, J. P. Joseph, and S. J. Seiler, "Preoperative radioactive seed localization for nonpalpable breast lesions: Technique, pitfalls, and solutions," *RadioGraphics*, vol. 35, no. 5, pp. 1319–1334, 2015.

[132] C. Lee, "MRI-guided preoperative ^{125} I seed localizations: Case report," *Breast J.*, vol. 24, no. 3, pp. 397–399, 2018.

[133] K. Moghissi and K. Dixon, “Image-guided surgery and therapy for lung cancer: a critical review.,” *Futur. Oncol.*, vol. 13, no. 26, pp. 2383–2394, 2017.

[134] R. Tabanfar *et al.*, “Real-time continuous image-guided surgery: Preclinical investigation in glossectomy,” *Laryngoscope*, vol. 127, no. 10, pp. E347–E353, 2017.

[135] P. L. Kubben, K. J. ter Meulen, O. E. M. G. Schijns, M. P. ter Laak-Poort, J. J. van Overbeeke, and H. van Santbrink, “Intraoperative MRI-guided resection of glioblastoma multiforme: A systematic review,” *Lancet Oncol.*, vol. 12, no. 11, pp. 1062–1070, 2011.

[136] S. L. Bugby, J. E. Lees, and A. C. Perkins, “Hybrid intraoperative imaging techniques in radioguided surgery: present clinical applications and future outlook,” *Clin. Transl. Imaging*, vol. 5, no. 4, pp. 323–341, 2017.

[137] M. V. Marshall, J. C. Rasmussen, I. Tan, M. V Marshall, C. E. Fife, and E. M. Sevick-, “Near-Infrared Fluorescence Imaging in Humans with Indocyanine Green: A Review and Update,” *Open Surg. Oncol. J.*, vol. 2, no. 2, pp. 12–25, 2012.

[138] T. Ishizawa *et al.*, “Real-time identification of liver cancers by using indocyanine green fluorescent imaging,” *Cancer*, vol. 115, no. 11, pp. 2491–2504, 2009.

[139] B. Alacam, B. Yazici, X. Intes, S. Nioka, and B. Chance, “Pharmacokinetic-rate images of indocyanine green for breast tumors using near-infrared optical methods,” *Phys. Med. Biol.*, vol. 53, no. 4, pp. 837–859, 2008.

[140] J. Zheng *et al.*, “A multimodal nano agent for image-guided cancer surgery,” *Biomaterials*, vol. 67, pp. 160–168, 2015.

[141] S. Lutje *et al.*, “Dual-modality image-guided surgery of prostate cancer with a radiolabeled fluorescent anti-PSMA monoclonal antibody,” *J. Nucl. Med.*, vol. 55, no. 6, pp. 995–1001, 2014.

[142] J. Brierley, M. Gospodarowicz, and B. O’Sullivan, “Principles of cancer staging,” *Ecancermedicalscience*, vol. 10, no. ed61, pp. 1–4, 2016.

[143] B. Zhu, J. Yang, P. Zhang, L. Shen, X. Li, and J. Li, “Safety and effectiveness of localized lung resection combined with neoadjuvant chemotherapy in the treatment of stage I-II non-small cell lung cancer,” *Oncol. Lett.*, vol. 13, no. 4, pp. 2344–2348, 2017.

[144] R. D. Shah and T. A. D'Amico, "Modern impact of video assisted thoracic surgery," *J. Thorac. Dis.*, vol. 6, pp. S631–S636, 2014.

[145] N. N. Y. Janssen *et al.*, "Radioactive seed localization in breast cancer treatment," *Br. J. Surg.*, vol. 103, no. 1, pp. 70–80, 2016.

[146] C. Li *et al.*, "Dual optical and nuclear imaging in human melanoma xenografts using a single targeted imaging probe," *Nucl. Med. Biol.*, vol. 33, no. 3, pp. 349–358, 2006.

[147] S. Leong *et al.*, "Electromagnetic navigation bronchoscopy: A descriptive analysis," *J. Thorac. Dis.*, vol. 4, no. 2, pp. 173–185, 2012.

[148] J. Brunner and R. Kraemer, "Copper(II)-quenched oligonucleotide probes for fluorescent DNA sensing," *J. Am. Chem. Soc.*, vol. 126, no. 42, pp. 13626–13627, 2004.

[149] D. Maji, M. Zhou, P. Sarder, and S. Achilefu, "Near infrared fluorescence quenching properties of copper (II) ions for potential applications in biological imaging," *Prog. Biomed. Opt. Imaging - Proc. SPIE*, vol. 8956, no. Ii, pp. 1–6, 2014.

[150] G. M. Mamardashvili and B. D. Berezin, "Reactions of chelate complexes with macrocyclic ligands. Tetra-tert-butylphthalocyanine," *Russ. J. Coord. Chem. Khimiya*, vol. 30, no. 5, pp. 335–338, 2004.

[151] K. H. Lieser, "Nuclear and Radiochemistry Fundamentals and Applicat ions," vol. 151. *VCH*, 1997.

[152] Y. Yoshii *et al.*, "64Cu-ATSM therapy targets regions with activated DNA repair and enrichment of CD133+cells in an HT-29 tumor model: Sensitization with a nucleic acid antimetabolite," *Cancer Lett.*, vol. 376, no. 1, pp. 74–82, 2016.

[153] A. R. Jalilian and J. Osso, "The current status and future of theranostic Copper-64 radiopharmaceuticals," *Iran. J. Nucl. Med.*, vol. 25, no. 1, pp. 1–10, 2017.

[154] A. C. S. Lobo *et al.*, "Phthalocyanine labels for near-infrared fluorescence imaging of solid tumors," *J. Med. Chem.*, vol. 59, no. 10, pp. 4688–4696, 2016.

[155] E. P. Porcu, A. Salis, E. Gavini, G. Rassu, M. Maestri, and P. Giunchedi, "Indocyanine green delivery systems for tumour detection and treatments," *Biotechnol. Adv.*, vol. 34, no. 5, pp. 768–789, 2016.

[156] J. Tchou *et al.*, “Safety and efficacy of intratumoral injections of chimeric antigen receptor (CAR) T cells in metastatic breast cancer,” *Cancer Immunol. Res.*, vol. 5, no. December, p. canimm.0189.2017, 2017.

[157] J. T. Jørgensen, M. Persson, J. Madsen, and A. Kjær, “High tumor uptake of 64 Cu : Implications for molecular imaging of tumor characteristics with copper-based PET tracers,” *Nucl. Med. Biol.*, vol. 40, no. 3, pp. 345–350, 2013.

[158] S. A. Gulec, E. Hoenie, R. Hostetter, and D. Schwartzentruber, “PET probe-guided surgery: Applications and clinical protocol,” *World J. Surg. Oncol.*, vol. 5, no. 65, pp. 1–7, 2007.

[159] J. Rousseau, D. Autenrieth, and J. E. Van Lier, “Synthesis, tissue distribution and tumor uptake of99mTc- and67Ga-tetrasulfophthalocyanine,” *Int. J. Appl. Radiat. Isot.*, vol. 36, no. 9, pp. 709–716, 1985.

[160] V. Ščasnár and J. E. Van Lier, “Biological activities of phthalocyanines-XV. Radiolabeling of the differently sulfonated67Ga-phthalocyanines for photodynamic therapy and tumor imaging,” *Nucl. Med. Biol.*, vol. 20, no. 3, pp. 257–262, 1993.

[161] H. Shirato *et al.*, “Feasibility of insertion/implantation of 2.0-mm-diameter gold internal fiducial markers for precise setup and real-time tumor tracking in radiotherapy,” *Int. J. Radiat. Oncol. Biol. Phys.*, vol. 56, no. 1, pp. 240–247, 2003.

[162] K. Tanderup, C. Ménard, C. Polgar, J. C. Lindegaard, C. Kirisits, and R. Pötter, “Advancements in brachytherapy,” *Adv. Drug Deliv. Rev.*, vol. 109, pp. 15–25, 2017.

[163] A. L. Petersen *et al.*, “In vivo evaluation of PEGylated 64 Cu-liposomes with theranostic and radiotherapeutic potential using micro PET / CT,” *Eur J Nucl Med Mol Imaging.*, vol. 45, no. 5, pp. 941-952, 2016.

[164] S. Hermanto, R. D. Haryuni, M. Ramli, A. Mutalib, and S. Hudiyono, “Synthesis and stability test of radioimmunoconjugate 177Lu-DOTA-F(ab′)2-trastuzumab for theranostic agent of HER2 positive breast cancer,” *J. Radiat. Res. Appl. Sci.*, vol. 9, no. 4, pp. 441–448, 2016.

[165] R. M. de Kruijff, H. T. Wolterbeek, and A. G. Denkova, “A critical review of alpha radionuclide therapy-how to deal with recoiling daughters?,” *Pharmaceuticals*, vol. 8, no. 2, pp. 321–336, 2015.

[166] B. Chen *et al.*, "Targeting negative surface charges of cancer cells by multifunctional nanoprobes," *Theranostics*, vol. 6, no. 11, pp. 1887–1898, 2016.

[167] A. Helenius and K. Simons, "Solubilization of membranes by detergents," *Biochim. Biophys. Acta, Biomembr.*, vol. 415, no. 1, pp. 29–79, 1975.

[168] J. R. Henriksen, T. L. Andresen, L. N. Feldborg, L. Duelund, and J. H. Ipsen, "Understanding Detergent Effects on Lipid Membranes : A Model Study of Lysolipids," *Biophysj*, vol. 98, no. 10, pp. 2199–2205, 2010.

[169] K. Shinoda, B.-I. Tamanushi, T. Nakagawa, and T. Isemura, "Colloidal Surfactants," vol. 12. *Acedamic Press,INC, New York*, 1963.

[170] J. Knobloch, D. K. Suhendro, J. L. Zieleniecki, J. G. Shapter, and I. Köper, "Membrane-drug interactions studied using model membrane systems," *Saudi J. Biol. Sci.*, vol. 22, no. 6, pp. 714–718, 2015.

[171] S. Tsermentseli, K. Kontogiannopoulos, V. Papageorgiou, and A. Assimopoulou, "Comparative study of PEGylated and conventional liposomes as carriers for shikonin," *Fluids*, vol. 3, no. 2, p. 36, 2018.

[172] A. M. Vali, T. Toliyat, B. Shafaghi, and S. Dadashzadeh, "Preparation, optimization, and characterization of topotecan loaded PEGylated liposomes using factorial design," *Drug Dev. Ind. Pharm.*, vol. 34, no. 1, pp. 10–23, 2008.

[173] F. X. Contreras, L. Sánchez-Magraner, A. Alonso, and F. M. Goñi, "Transbilayer (flip-flop) lipid motion and lipid scrambling in membranes," *FEBS Lett.*, vol. 584, no. 9, pp. 1779–1786, 2010.

[174] A. L. Petersen *et al.*, "64Cu loaded liposomes as positron emission tomography imaging agents," *Biomaterials*, vol. 32, pp. 2334–2341, 2011.

[175] T. M. Jones-Wilson *et al.*, "The in vivo behavior of copper-64-labeled azamacrocyclic complexes," *Nucl. Med. Biol.*, vol. 25, no. 6, pp. 523–530, 1998.

[176] A. I. Jensen, T. Binderup, P. Kumar Ek, A. Kjær, P. H. Rasmussen, and T. L. Andresen, "Positron emission tomography based analysis of long-circulating cross-linked triblock polymeric micelles in a U87MG mouse xenograft model and comparison of DOTA and CB-

TE2A as chelators of copper-64," *Biomacromolecules*, vol. 15, no. 5, pp. 1625–1633, 2014.

[177] A. Bao, B. Goins, R. Klipper, G. Negrete, M. Mahindaratne, and W. T. Phillips, "A novel liposome radiolabeling method using 99mTc-' SNS/S' complexes: In vitro and in vivo evaluation," *J. Pharm. Sci.*, vol. 92, no. 9, pp. 1893–1904, 2003.

[178] A. E. Hansen *et al.*, "Positron emission tomography based elucidation of the enhanced permeability and retention effect in dogs with cancer using copper-64 liposomes," no. 7, pp. 6985–6995, 2015.

[179] J. M. Hierrezuelo and C. Carnero Ruiz, "Exploring the affinity binding of alkylmaltoside surfactants to bovine serum albumin and their effect on the protein stability: A spectroscopic approach," *Mater. Sci. Eng. C*, vol. 53, pp. 156–165, 2015.

[180] S. Yook, Z. Cai, Y. Lu, M. A. Winnik, J.-P. Pignol, and R. M. Reilly, "Intratumorally injected 177Lu-labeled gold nanoparticles: gold nanoseed brachytherapy with application for neoadjuvant treatment of locally advanced breast cancer," *J. Nucl. Med.*, vol. 57, no. 6, pp. 936–942, 2016.

[181] N. Just, "Improving tumour heterogeneity MRI assessment with histograms," *Br. J. Cancer*, vol. 111, no. 12, pp. 2205–2213, 2014.

[182] K. Yong and M. Brechbiel, "Application of ^{212}Pb for targeted α-particle therapy (TAT): pre-clinical and mechanistic understanding through to clinical translation," *AIMS Med. Sci.*, vol. 2, no. 3, pp. 228–245, 2015.

[183] A. I. Kassis, "Cancer therapy with Auger electrons: are we almost there?," *J. Nucl. Med.*, vol. 44, no. 9, pp. 1479–1481, 2003.

[184] Y. Dekempeneer *et al.*, "Targeted alpha therapy using short-lived alpha-particles and the promise of nanobodies as targeting vehicle," *Expert Opin. Biol. Ther.*, vol. 16, no. 8, pp. 1035–1047, 2016.

[185] J. Elgqvist, S. Frost, J.-P. Pouget, and P. Albertsson, "The potential and hurdles of targeted Alpha therapy – Clinical trials and beyond," *Front. Oncol.*, vol. 3, pp. 1–9, 2014.

[186] P. J. Blower, J. S. Lewis, and J. Zweit, "Copper radionuclides and radiopharmaceuticals in nuclear medicine," *Nucl. Med. Biol.*, vol. 23, no. 8, pp. 957–980, 1996.

[187] E. Wong and C. M. Giandornenico, “Current status of platinum-based antitumor drugs,” *Chem. Rev.*, vol. 99, no. 9, pp. 2451–2466, 1999.

[188] I. Ali, W. A. Wani, K. Saleem, and A. Haque, “Platinum compounds: a hope for future cancer chemotherapy.,” *Anticancer Agents Med. Chem.*, vol. 13, no. 2, pp. 296–306, 2013.

[189] S. Dasari and P. B. Tchounwou, “Cisplatin in cancer therapy: Molecular mechanisms of action,” *Eur. J. Pharmacol.*, vol. 740, no. 1, pp. 364–378, 2014.

[190] N. Muhammad and Z. Guo, “Metal-based anticancer chemotherapeutic agents,” *Curr. Opin. Chem. Biol.*, vol. 19, no. 1, pp. 144–153, 2014.

[191] E. Y. Tshuva and D. Peri, “Modern cytotoxic titanium(IV) complexes; Insights on the enigmatic involvement of hydrolysis,” *Coord. Chem. Rev.*, vol. 253, no. 15–16, pp. 2098–2115, 2009.

[192] A. Korfel *et al.*, “Phase I clinical and pharmacokinetic study of titanocene dichloride in adults with advanced solid tumors,” *Clin. Cancer Res.*, vol. 4, no. November, pp. 2701–2708, 1998.

[193] P. Köpf-Maier, “Antitumor activity of titanocene dichloride in xenografted human renal-cell carcinoma,” *Anticancer Res.*, vol. 19, no. 1 A, pp. 493–504, 1999.

[194] G. W. Severin, C. H. Nielsen, A. I. Jensen, J. Fonslet, A. Kjær, and F. Zhuravlev, “Bringing radiotracing to titanium-based antineoplastics: solid phase radiosynthesis, PET and ex Vivo evaluation of antitumor agent [45 Ti](salan)Ti(dipic),” *J. Med. Chem.*, vol. 58, pp. 7591–7595, 2015.

[195] F. Caruso and M. Rossi, “Antitumor titanium compounds,” *Med. Chem. (Los. Angeles).*, vol. 4, pp. 49–60, 2004.

[196] K. M. Buettner and A. M. Valentine, “Bioinorganic chemistry of titanium,” *Chem. Rev.*, vol. 112, no. 3, pp. 1863–1881, 2012.

[197] E. Melendez, “Titanium complexes in cancer treatment,” *Crit. Rev. Oncol. Hematol.*, vol. 42, pp. 309–315, 2002.

[198] T. A. Immel, U. Groth, and T. Huhn, “Cytotoxic titanium salan complexes: Surprising interaction of salan and alkoxy ligands,” *Chem. - A Eur. J.*, vol. 16, no. 9, pp. 2775–2789,

2010.

[199] T.W.Burrows, “Nuclear data sheets for A = 45*,” *Nucl. Data Sheets*, vol. 109, pp. 171–296, 2008.

[200] N. Cheng, T. Xia, Y. Han, Q. J. He, R. Zhao, and J. R. Ma, “Synergistic antitumor effects of liposomal honokiol combined with cisplatin in colon cancer models,” *Oncol. Lett.*, vol. 2, no. 5, pp. 957–962, 2011.

[201] R. R. S. Thakur, H. L. McMillan, and D. S. Jones, “Solvent induced phase inversion-based in situ forming controlled release drug delivery implants,” *J. Control. Release*, vol. 176, no. 1, pp. 8–23, 2014.

[202] P. D. Graham, K. J. Brodbeck, and A. J. McHugh, “Phase inversion dynamics of PLGA solutions related to drug delivery,” *J. Control. Release*, vol. 58, no. 2, pp. 233–245, 1999.

[203] C. Hansch, A. Leo, and D. Hoekman, “Hydrophobic, Electronic, and Steric Constants, ACS Professional Reference Book,” *ACS, Washington,* 1995.

[204] J. A. Riddick, W. B. Bunger, and T. K. Sakano, “Techniques of Chemistry 4th ed., Volume II. Organic Solvents,” *John Wiley and Sons, New York*, 1985.

[205] L. Wang, S. Venkatraman, and L. Kleiner, “Drug release from injectable depots : two different in vitro mechanisms,” *J. Control. Release 99*, vol. 99, pp. 207–216, 2004.

[206] L. Wang *et al.*, “Design of a long-term antipsychotic in situ forming implant and its release control method and mechanism,” *Int. J. Pharm.*, vol. 427, no. 2, pp. 284–292, 2012.

[207] H. Kranz and R. Bodmeier, “Structure formation and characterization of injectable drug loaded biodegradable devices : In situ implants versus in situ microparticles,” *Eur. J. Pharm. Sci.*, vol. 4, pp. 164–172, 2008.

[208] J. R. Zeevaart *et al.*, “Production of high specific activity 195m Pt-cisplatinum at South African nuclear energy corporation for Phase 0 clinical trials in healthy individual subjects †,” *J. Label. Compd. Radiopharm.*, vol. 56, no. July, pp. 495–503, 2013.